

# Measurement of the Ratio of the Sachs Form Factors of the Proton at the Psi-prime Resonance

In the experiment E835 conducted at Fermi National Accelerator Laboratory, proton-antiproton annihilation was studied using a stochastically cooled antiproton beam incident on an internal hydrogen gas jet target. The E835 detector was optimized for the detection of electromagnetic final states ( $e^+$ ,  $e^-$  and  $\gamma$ ) in the presence of a large hadronic background. We collected  $22.57 \text{ pb}^{-1}$  of data at the center-of-mass energy of the  $\psi'$  resonance (3686 MeV) during two separate periods of data taking. In these data there was a subset of 6844 exclusive  $e^+e^-$  events, the analysis of which is the subject of this thesis. The reaction  $\bar{p}p \rightarrow e^+e^-$  probes the electromagnetic structure of the proton, which can be represented by the Sachs form factors  $G_E$  and  $G_M$ . These form factors have been well measured as a function of momentum transfer squared ( $q^2$ ) in the space-like region ( $q^2 < 0$ ). In the time-like region ( $q^2 \geq 4M_p^2$ ), the experiments are more difficult due to the rapid fall-off in the  $\bar{p}p$  cross section. In this thesis the first measurement of the angular distribution of the process  $\bar{p}p \rightarrow e^+e^-$  at the  $\psi'$  resonance is described and from this result the value of  $\left| \frac{G_E}{G_M} \right|$  was determined to be  $0.87^{+0.25}_{-0.24}$ .

UNIVERSITY OF MINNESOTA

This is to certify that I have examined this bound copy of a doctoral thesis by

Seon-Hee Seo

and have found that it is complete and satisfactory in all respects and that any and all  
revisions required by the final examining committee have been made.

Professor Roger W. Rusack  
(Faculty Adviser)

---

---

GRADUATE SCHOOL

# Measurement of the Ratio of the Sachs Form Factors of the Proton at the Psi-prime Resonance

A THESIS  
SUBMITTED TO THE FACULTY OF THE GRADUATE SCHOOL  
OF THE UNIVERSITY OF MINNESOTA  
BY

Seon-Hee Seo

IN PARTIAL FULFILLMENT OF THE REQUIREMENTS  
FOR THE DEGREE OF  
DOCTOR OF PHILOSOPHY

January, 2004

© Seon-Hee Seo 2004  
ALL RIGHTS RESERVED



# Measurement of the Ratio of the Sachs Form Factors of the Proton at the Psi-prime Resonance

by Seon-Hee Seo

Under the supervision of Professor Roger W. Rusack

## ABSTRACT

In the experiment E835 conducted at Fermi National Accelerator Laboratory, proton-antiproton annihilation was studied using a stochastically cooled antiproton beam incident on an internal hydrogen gas jet target. The E835 detector was optimized for the detection of electromagnetic final states ( $e^+$ ,  $e^-$  and  $\gamma$ ) in the presence of a large hadronic background. We collected  $22.57 \text{ pb}^{-1}$  of data at the center-of-mass energy of the  $\psi'$  resonance (3686 MeV) during two separate periods of data taking. In these data there was a subset of 6844 exclusive  $e^+e^-$  events, the analysis of which is the subject of this thesis. The reaction  $\bar{p}p \rightarrow e^+e^-$  probes the electromagnetic structure of the proton, which can be represented by the Sachs form factors  $G_E$  and  $G_M$ . These form factors have been well measured as a function of momentum transfer squared ( $q^2$ ) in the space-like region ( $q^2 < 0$ ). In the time-like region ( $q^2 \geq 4M_p^2$ ), the experiments are more difficult due to the rapid fall-off in the  $\bar{p}p$  cross section. In this thesis the first measurement of the angular distribution of the process  $\bar{p}p \rightarrow e^+e^-$  at the  $\psi'$  resonance is described and from this result the value of  $\left| \frac{G_E}{G_M} \right|$  was determined to be  $0.87^{+0.25}_{-0.24}$ .

# Acknowledgements

My first thanks go to my thesis advisor Prof. Roger Rusack who has believed in me and supported me with his advice and guidance throughout my research career at Minnesota. I would also like to thank our spokespeople Stephen Pordes and Rosanna Cester: Their insights, experience and wisdom made our experiment possible and successful.

My special thanks go to Claudia Patrignani for many helpful consultations during my research in E835. I would like to thank Paolo Rumerio, Jason Kasper, Matteo Negrini, Mirco Andreotti, Wander Baldini, Mathew Graham, Ted Vidnovic III, David Joffe, Keith Gollwitzer, Wilhelm Roethel and Amiran Tomaradze: They freely gave of their precious time in providing me with useful information and materials. I would like to give thanks to all my other collaborators as well.

It is not enough for me to say thank you to Prof. Serge Rudaz for his help especially in theory part of my thesis: His brightness, insight and erudition in physics always inspired me. Prof. Jon Urheim also deserves my thanks for the many good discussions we had while he was in Minnesota.

I would like to thank Alex Smith, Long Duong and Steve Giron who provided me with technical help on a number of occasions.

My friend Un-Ki Yang deserves my thanks: He furnished me with constructive criticism and general help whenever I was in need of it.

Most of all, my heartfelt thanks go to my parents. They always have believed in me and have been the source of my strength so that I was able to complete my degree in the United States.

Without all of them, my thesis would not have come to light.

To my parents



# Table of Contents

Abstract	i
Acknowledgements	ii
List of Tables	viii
List of Figures	x
<b>1 Theoretical Background</b>	<b>1</b>
1.1 Form Factors in the Space-like Region . . . . .	3
1.2 Form Factors in the Time-like Region . . . . .	13
1.3 Asymptotic Property of Form Factors . . . . .	16
<b>2 Experimental Setup</b>	<b>21</b>
2.1 Antiproton ( $\bar{p}$ ) Beam . . . . .	23
2.1.1 $\bar{p}$ Production . . . . .	23
2.1.2 $\bar{p}$ Cooling and Storage . . . . .	23
2.1.3 $\bar{p}$ Deceleration . . . . .	25
2.1.4 Collision and Data taking . . . . .	25
2.1.5 $\bar{p}$ Dump . . . . .	26
2.2 The Hydrogen Gas Jet Target . . . . .	26
2.3 Luminosity Monitor . . . . .	27
2.4 Measurement of the Center of Mass Energy . . . . .	31
2.4.1 Measurement of the Orbit Length . . . . .	32
2.4.2 Measurement of the Revolution Frequency . . . . .	33

2.4.3	Measurement of the Beam Energy Spectrum . . . . .	34
2.5	Experimental Technique . . . . .	35
<b>3</b>	<b>The Detector</b>	<b>38</b>
3.1	Inner Detectors . . . . .	38
3.1.1	Hodoscopes . . . . .	39
3.1.2	Straw Chambers . . . . .	40
3.1.3	Scintillating Fiber Trackers . . . . .	42
3.2	Threshold Čerenkov Counter . . . . .	45
3.3	Electromagnetic Calorimeters . . . . .	46
3.3.1	Central Calorimeter . . . . .	47
3.3.2	Forward Calorimeter . . . . .	51
<b>4</b>	<b>Trigger System and Data Acquisition</b>	<b>55</b>
4.1	Hardware Trigger . . . . .	56
4.1.1	Charged Trigger (Level I trigger) . . . . .	57
4.1.2	Neutral Trigger (Level I trigger) . . . . .	62
4.1.3	Master MLU (Level II trigger) . . . . .	64
4.1.4	Gatemaster . . . . .	65
4.2	Software Trigger (Level III trigger) . . . . .	67
4.3	Data Acquisition (DAQ) . . . . .	67
4.3.1	Data Flow and DAQ Hardware . . . . .	69
<b>5</b>	<b>Data Analysis</b>	<b>73</b>
5.1	Data Set . . . . .	73
5.2	Clustering . . . . .	74
5.2.1	CCAL Clusterizer Algorithm . . . . .	74
5.2.2	“Shower splash” . . . . .	78
5.2.3	CCAL Timing . . . . .	81
5.3	Event Selection . . . . .	81
5.4	Background Study . . . . .	97
5.5	Contribution from Continuum . . . . .	97
5.6	Efficiency . . . . .	98

5.6.1	Pileup Efficiency . . . . .	98
5.6.2	Event Selection Efficiency and Geometrical Acceptance . . . .	101
<b>6</b>	<b>Results and Conclusion</b>	<b>109</b>
6.1	Fit Method . . . . .	109
6.2	Stack-by-stack Results . . . . .	110
6.3	Results from Full Data Set . . . . .	116
6.4	Results from Combined Data Sets . . . . .	116
6.5	Systematic Error . . . . .	121
6.6	Conclusions . . . . .	122
<b>Appendix A. Form factors and the angular distribution</b>		
	for the process $\bar{p}p \rightarrow e^+e^-$	<b>128</b>
<b>Appendix B. Helicity Amplitudes for the Process <math>\bar{p}p \rightarrow e^+e^-</math></b>		<b>135</b>
B.1	Wigner D-function and 2-body decay amplitude . . . . .	135
B.2	Angular distribution and the helicity amplitudes for the process $\bar{p}p (\lambda_{\bar{p}}\lambda_p) \rightarrow \psi'(\lambda) \rightarrow e^+e^- (\lambda_{\bar{e}}\lambda_e)$ . . . . .	137
<b>Appendix C. GEANT Monte Carlo Study of</b> “shower splash” and bremsstrahlung		<b>140</b>
<b>Appendix D. Kolmogorov-Smirnov Test</b>		<b>153</b>
<b>References</b>		<b>155</b>

# List of Tables

1.1	Some charge distributions and the corresponding form factors. . . . .	2
1.2	All measurements of magnetic form factor of the proton in the time-like region under the assumption that $ G_E  =  G_M $ . . . . .	17
1.3	Measured values of $\lambda$ , $\left \frac{G_E}{G_M}\right $ and $\left \frac{C_0}{C_1}\right $ at the $J/\psi$ . . . . .	18
1.4	Predicted values of $\lambda$ , $\left \frac{G_E}{G_M}\right $ and $\left \frac{C_0}{C_1}\right $ at the $J/\psi$ and $\psi'$ . . . . .	18
3.1	Characteristics of scintillating hodoscopes. . . . .	41
3.2	Characteristics of straw chambers. . . . .	42
3.3	Characteristics of the scintillating fibers. . . . .	43
3.4	Characteristics of the two cells of the threshold gas Čerenkov counter. . . . .	47
3.5	Geometrical characteristics of the CCAL blocks and their PMTs. . . . .	49
3.6	Characteristics of the FCAL blocks and their PMTs. . . . .	53
4.1	The inputs and outputs of the Charged MLU (1996-1997 run/2000 run). . . . .	63
4.2	The inputs and outputs of the Master MLU (1996-1997 run/2000 run). See the text for the explanation of the logical input combinations. . . . .	65
4.3	The inputs of the Gatemaster (1996-1997 run/2000 run). . . . .	66
4.4	PRUDE filters, physical meaning, priority, and final data tapes. . . . .	68
5.1	Stack-by-stack luminosity and the corresponding energy from the 1996-1997 run (left) and the 2000 run (right). . . . .	75
5.2	The different selections criteria applied for event selection (criteria with * were used for the pre-selection of the events). . . . .	94
5.3	The number of pre-selected events and the number of finally selected events from the 1996-1997 data (top 2 rows) and from the 2000 data (bottom 2 rows). . . . .	95



5.4	The number of pre-selected events and the number of finally selected events from the 1996-1997 (top 2 rows) and the 2000 GEANT MC (bottom 2 rows). A total of 330,000 MC $e^+e^-$ events was generated with $\lambda = 0$ at the $\psi'$ . . . . .	96
5.5	Possible $e^+e^-$ background channels and the corresponding number of mis-identified background events. . . . .	98
6.1	Stack-by-stack results and their average (last row) from the 1996-1997 data. . . . .	111
6.2	Stack-by-stack results and their average (last row) from the 2000 data.	112
6.3	The K-S test results between each stack from the 1996-1997 run. The last row is the test result between a given stack and the rest of the stacks. . . . .	114
6.4	The K-S test results between each stack from the 2000 run. The last row is the test result between a given stack and the rest of the stacks.	114
6.5	The comparison of the results from the two data sets. The values of $\lambda$ from the two data set are consistent. . . . .	119
6.6	The systematic errors from each cut and the final systematic error (last row). . . . .	123
6.7	The experimental measurements and the theoretical predictions on $\lambda$ at the $J/\psi$ and $\psi'$ . . . . .	126
6.8	Extracted values of $\left \frac{G_F}{G_M}\right $ and $\left \frac{C_0}{C_1}\right $ using the measured/predicted $\lambda$ at the $J/\psi$ and $\psi'$ from Table 6.7. . . . .	126
A.1	Each component of currents and helicities of $\bar{p}p$ and $e^+e^-$ . In $e^+e^-$ part, the values are from the direct calculation of $\chi_{-\lambda_e}^\dagger(\hat{k})\vec{\sigma}\chi_{-\bar{\lambda}_e}\delta_{\lambda_e,-\bar{\lambda}_e}$ .	133
C.1	The number of events assorted with the number of clusters according to the seed/cluster thresholds. See text. . . . .	143
C.2	The number of $e^+e^-$ events assorted with the number of clusters according to the seed/cluster thresholds. See text. . . . .	144
C.3	The number of events with additional clusters with only CCAL and FCAL “on”, divided by that with the complete detector “on” according to the seed/cluster threshold. A total of 100,000 $e^+e^-$ MC events was generated at the $\psi'$ . . . . .	146

# List of Figures

1.1	The lowest order Feynman diagram of the $e^-p \rightarrow e^-p$ scattering. (All quantities are described in the text following Eq. (1.3).)	4
1.2	Vertex correction term responsible for the anomalous magnetic moment of the electron.	5
1.3	The first measurement of the proton structure in $e^-p$ scattering (adapted from [7]).	8
1.4	Schematic of the Rosenbluth separation method.	9
1.5	Dipole scaling ( $G_D$ ) behavior of $G_M$ both in Rosenbluth technique (hollow square) and polarization technique (filled circle) up to 6 GeV <sup>2</sup> (adapted from [15]).	12
1.6	Discrepancy between the Rosenbluth technique (hollow) and polarization technique (filled circle). (adapted from [15]). See text.	12
1.7	The lowest order Feynman diagram of the $\bar{p}p \rightarrow e^+e^-$ process.	13
1.8	All measurements of $ G_M $ vs. $Q^2$ in the time-like region under the assumption that $ G_E  =  G_M $ [38].	20
2.1	$\bar{p}$ source at Fermilab.	22
2.2	Schematic of stochastic (betatron) cooling (from [43]).	24
2.3	The formation of clusters of hydrogen gas jet target inside the trumpet shaped nozzle (left) and cross sectional view of the gas jet target perpendicular to the $\bar{p}$ beam direction (right).	27
2.4	The hydrogen jet density vs. pressure curve for a given temperature (top line), operating temperature vs. pressure curve for a given density (open circles), and the hydrogen saturation curve (bottom line).	28

2.5	The hydrogen jet target density (filled circles) needed to be increased during the data taking to keep a constant luminosity ( $\sim 2.5 \times 10^{31} \text{cm}^{-2} \text{sec}^{-1}$ ) (white circles) to compensate the decrease of the $\bar{p}$ current (decreasing line) as a result of the $\bar{p}p$ interactions. . . . .	29
2.6	Luminosity monitor: side view (left and top right), top view (bottom right). . . . .	30
2.7	Schottky noise power spectrum at the 127th harmonic. . . . .	35
2.8	Excitation curve of $\chi_0 \rightarrow J/\psi\gamma$ . . . . .	37
3.1	Cross section of E835 detector for the 2000 run. . . . .	39
3.2	Beam's view of the inner detectors. . . . .	40
3.3	Mechanical structure of the straw chamber. . . . .	41
3.4	Side cross section of the scintillating fibers. . . . .	43
3.5	Schematic of the light path from the scintillating fibers to the VLPC cryostat. . . . .	44
3.6	Cross section of the Čerenkov counter. . . . .	46
3.7	Cross section of the CCAL. . . . .	48
3.8	Schematic of the laser monitoring system for CCAL. . . . .	51
3.9	Beam's view of FCAL consisted of a total of 144 lead glass blocks (black rectangles represent dead blocks). . . . .	52
3.10	Invariant mass distribution of $\pi^0$ candidates used for preliminary FCAL calibration. . . . .	54
3.11	FCAL calibration constant (block #3) vs. integrated luminosity obtained from laser data (white triangles) after rescaling to the 6 photon data (black dots). . . . .	54
4.1	Schematic of the E835 trigger system [64]. . . . .	58
4.2	Schematic of the E835 charged trigger system. . . . .	59
4.3	Schematic of E835 DAQ hardware system. . . . .	70
5.1	Three types of clusters: "split" (left), "shared" (middle), and "isolated" (right). . . . .	77
5.2	Cluster mass distribution for "isolated" clusters (peak near 60 MeV) and "split" clusters (peak near 135 MeV). . . . .	77

5.3	An $e^+e^-$ event display (top) and the corresponding hits in the CCAL (bottom) obtained by the 2000 GEANT MC. . . . .	79
5.4	A 2-cluster event is interpreted as a 3-cluster event in the CCAL by a clusterizer Boxes represent hit map and arrows represent clusters (two down-pointing triangles represent main clusters and one up-pointing triangle represents a secondary cluster). . . . .	80
5.5	Seed/cluster threshold dependency of 2-cluster events normalized to the total # of events using the 1996-1997 MC (top) and the 2000 MC (bottom). . . . .	84
5.6	Invariant mass distribution between $e^-$ ( $e^+$ ) and its secondary cluster. Top: the 1996-1997 MC (left) and data (right), Bottom: the 2000 MC (left) and data (right). No other selections were applied except for pre-selection criteria (see Table 5.2). . . . .	86
5.7	The probability distribution of the 4C fit. Top: the 1996-1997 MC (left) and data (right), Bottom: the 2000 MC (left) and data (right). No other selections were applied except for pre-selection criteria (see Table 5.2). . . . .	87
5.8	A $\log_{10}$ plot of the electron weight (EW) distribution. Top: the 1996-1997 MC (left) and data (right), Bottom: the 2000 MC (left) and data (right). The hatched area in the 2000 data was obtained by background events. No other selections were applied except for pre-selection criteria (see Table 5.2). . . . .	89
5.9	The cluster mass ( $m_{cl}$ ) distribution of the $e^+e^-$ candidates. Top: the 1996-1997 MC (left) and data (right), Bottom: the 2000 MC (left) and data (right). No other selections were applied except for pre-selection cuts (see Table 5.2). . . . .	91
5.10	Invariant mass distributions of the $e^+e^-$ candidates. Top: the 1996-1997 MC (left) and data (right), Bottom: the 2000 MC (left) and data (right). Shaded area ( $> 3.4$ GeV) represents finally selected events. . . . .	92

5.11	Angular distribution of the reconstructed events (lower lines) with “split” OFF. A total of 100,000 $e^+e^-$ events was generated using the 2000 GEANT MC with $\lambda = 0$ (upper lines). (top: 2-cluster events, bottom: including events with up to 2 secondary clusters.) . . . . .	93
5.12	Pileup efficiency ( $\epsilon_{pileup}$ ) vs. instantaneous luminosity ( $L_{inst}$ ) from the 1996-1997 MC (top) and from the 2000 MC (bottom). The line is a fit to the MC data. . . . .	100
5.13	Pileup efficiency ( $\frac{RG_{ON}}{RG_{OFF}}$ ) vs. $\cos\theta^*$ from the 1996-1997 MC (top) and from the 2000 MC (bottom). . . . .	102
5.14	Event selection efficiency as a function of $\cos\theta^*$ . A total of 330,000 $e^+e^-$ events with $\lambda = 0$ was generated using the GEANT MC (top: from the 1996-1997 MC, bottom: from the 2000 MC). . . . .	103
5.15	CCAL ring number vs. $\cos\theta^*$ coverage. . . . .	104
5.16	$\phi$ vs. $\cos\theta^*$ coverage (There are two entries per event). . . . .	105
5.17	Event selection efficiency as a function of $\cos\theta^*$ . (No dead blocks and # of bins = 12) Note the dip in $\cos\theta^* = 0.2$ region has disappeared. A total of 100,000 $e^+e^-$ events with $\lambda = 0$ was generated using the GEANT MC (top: from the 1996-1997 MC, bottom: from the 2000 MC). . . . .	106
5.18	Efficiency vs. ring number (two entries per event). . . . .	107
5.19	Before and after efficiency correction to the finally selected events. (top: the 1996-1997 data, bottom: the 2000 data) . . . . .	108
6.1	The K-S probability distribution between each stack from the 1996-1997 run and the 2000 run. . . . .	115
6.2	$\lambda$ from each stack vs. the K-S probability between a stack and the rest of the stacks for both the 1996-1997 and the 2000 data sets. No particular relation exists between $\lambda$ and the K-S probability. . . . .	115
6.3	The angular distribution of $\bar{p}p \rightarrow e^+e^-$ at the $\psi'$ from the 1996-1997 data and its likelihood fit (line). . . . .	117
6.4	The angular distribution of $\bar{p}p \rightarrow e^+e^-$ at the $\psi'$ from the 2000 data and its likelihood fit (line). . . . .	118

6.5	Fitted $\lambda$ (2000 data) vs. $\#$ of bins. Note that the $\#$ of bins does not affect for measuring $\lambda$ . . . . .	119
6.6	The angular distribution of $\bar{p}p \rightarrow e^+e^-$ at the $\psi'$ from the combined data (filled circles). The fit result (line) is $\lambda = 0.67^{+0.15}_{-0.14}$ (stat.) Open circles represents MC events generated with $\lambda = 0.67$ . . . . .	120
6.7	All the measurements and the theoretical predictions of $\lambda$ at the $J/\psi$ (top) and $\psi'$ (bottom). . . . .	127
A.1	$\bar{p}p \rightarrow e^+e^-$ in the CM system. . . . .	129
C.1	3-cluster events normalized to the total $\#$ of events vs. seed/cluster threshold using the 1996-1997 MC (Top) and the 2000 MC (Bottom). . . . .	145
C.2	Graphical representaion of Table C.3. . . . .	147
C.3	$\theta_{lab}$ vs. $\cos\theta^*$ obtained from $e^+e^-$ events using the 2000 GEANT MC. . . . .	148
C.4	Angular distribution of the 3-cluster events with the complete detector “on” (white area) and with CCAL and FCAL “on” (hatched area) according to seed/cluster thresholds (25/50 to 70/70) obtained by using the 1996-1997 GEANT MC. . . . .	149
C.5	Angular distribution of the 3-cluster events with the complete detector “on” (white area) and with CCAL and FCAL “on” (hatched area) according to seed/cluster thresholds (80/80 to 110/110) obtained by using the 1996-1997 GEANT MC. . . . .	150
C.6	Angular distribution of the 3-cluster events with the complete detector “on” (white area) and with CCAL and FCAL “on” (hatched area) according to seed/cluster thresholds (25/50 to 70/70) obtained by using the 2000 GEANT MC. . . . .	151
C.7	Angular distribution of the 3-cluster events with the complete detector “on” (white area) and with CCAL and FCAL “on” (hatched area) according to seed/cluster thresholds (80/80 to 110/110) obtained by using the 2000 GEANT MC. . . . .	152
D.1	The cumulative distributions of the two data sets being used for the K-S test. The D represents the maximum deviation of the two data sets. . . . .	154

# Chapter 1

## Theoretical Background

In the standard model, there are six quarks ( $u, d, c, s, t$  and  $b$ ) and six leptons ( $e, \nu_e, \mu, \nu_\mu, \tau$  and  $\nu_\tau$ ) as the fundamental particles in the universe. There are three types of force carriers (neglecting gravity) in the model, which mediate the interactions between them. They are the photon for the electromagnetic force,  $W^\pm$  and  $Z^0$  for the weak force, and eight gluons for the strong force. In Quantum Chromo Dynamics (QCD), the strong force makes bound states composed of three quarks for a baryon, or a quark and anti-quark pair for a meson. Baryons and mesons are known collectively as hadrons as opposed to leptons which are not affected by the strong interaction.

The electromagnetic (EM) structure of composite particles has been studied traditionally in scattering experiments in the same way that Rutherford used the scattering of alpha particles to probe the structure of the atom. More recently, the experiments that measure the electromagnetic properties of hadrons have been limited to the scattering of electrons since they have no strong interactions and are, as far as we know, point-like. Charge and magnetic moment distributions in space are not directly measureable, but their Fourier transforms, known as EM form factors <sup>1</sup> are directly measureable in scattering experiments.

The cross section for the scattering of a spinless charged particle by a potential due to a charge distribution can be written as:

---

<sup>1</sup>The concept of a form factor was first used in X-ray scattering to measure the distribution of charge through Fourier transform.

$$\left(\frac{d\sigma}{d\Omega}\right)_{charge\ dist.} = |F(\vec{q})|^2 \cdot \left(\frac{d\sigma}{d\Omega}\right)_{point} \quad (1.1)$$

where  $\vec{q}$  is the momentum transfer between the incident particle and the scattered particle and  $F(\vec{q})$  is the form factor which is in the non-relativistic limit the Fourier transform of the charge distribution  $\rho(\vec{r})$ :

$$F(\vec{q}) = \int e^{i\vec{q}\cdot\vec{r}} \rho(\vec{r}) d^3r \quad (1.2)$$

Thus  $F(\vec{q})$  is an indication of the degree of the compositeness. Table 1.1 lists some charge distributions and the corresponding representation of the form factors obtained by Fourier transform.

In relativistic theory, these form factors become analytic functions of the four-momentum transfer squared ( $q^2$ ). In the space-like region, where  $q^2$  is negative ( $q^2 \equiv -Q^2 < 0$ ), the physical process is the elastic scattering of an electron on a composite particle. In the time-like region, where  $q^2$  is positive ( $q^2 \equiv +Q^2 > 0$ ), the physical process is the annihilation of a lepton and an anti-lepton followed by the production of a hadron and anti-hadron ( $\bar{l}l \rightarrow h\bar{h}$ ), or the inverse process. In the space-like region the form factors are real functions, while they are complex functions in the time-like region [1].

charge distribution $\rho(\vec{r})$		Form factor $F(q^2)$	
Point	$\delta(\vec{r} - \vec{r}')$	Constant	1
Yukawa	$\frac{m^2}{4\pi r} e^{-mr}$	Mono pole	$(1 + \frac{q^2}{m^2})^{-1}$
Exponential	$\frac{m^3}{8\pi} e^{-mr}$	Dipole	$(1 + \frac{q^2}{m^2})^{-2}$
Gaussian	$\frac{m^3}{(2\pi)^{3/2}} e^{-m^2 r^2/2}$	Gaussian	$e^{-q^2/2m^2}$

Table 1.1: Some charge distributions and the corresponding form factors.



The space-like and time-like form factors should be described by a single analytic function over the whole range of  $q^2$  ( $-\infty < q^2 < +\infty$ ). Dispersion relations connect the real and imaginary parts of analytic functions [2] and thus allow one to predict, in principle, the form factors for any  $q^2$  once all the poles and branch-cuts in the time-like region and their behavior at large  $Q^2$  are known, or vice versa. The dispersion relation approach to nucleon form factors was first used in 1957 and later stimulated the discovery of the  $\rho$  and  $\omega$  mesons ([2] and Chap. 7 of [3]).

In perturbative QCD (pQCD), the form factors should be reliably calculable for large space-like  $q^2$ . In addition there is a proof based on the Phragmén-Lindelöf theorem [5], that the space-like form factors and the time-like form factors are the same as  $Q^2 \rightarrow \infty$ . Thus for large  $Q^2$ , the time-like form factors should be real functions and calculable within the framework of pQCD.

As experiments are simpler to perform in the space-like region, the form factors in this region have been investigated earlier and more data exist with higher  $Q^2$ . The main experimental difficulty in the time-like region is the small cross section for the process  $e^+e^- \rightarrow h\bar{h}$  (or  $h\bar{h} \rightarrow e^+e^-$ ) which decreases rapidly as  $Q^2$  increases. The ratio of the EM form factors, however, can be obtained using the angular distribution at resonances in the time-like region where higher statistics are available.

The proton is the lightest baryon, but its structure is still incompletely understood at the energy scale of QCD ( $\sim 1$  GeV): It is described by two form factors. (Generally for any particle with parity conservation and time reversal invariance, the number of EM form factors is  $(2S + 1)$  for a composite spin  $S$  particle.) In the non-relativistic limit and in the space-like region, they are electric charge and magnetic moment distributions through Fourier transform. The discussions in the following sections are restricted to the EM form factors of the proton both in the space-like and the time-like regions.

## 1.1 Form Factors in the Space-like Region

In Figure 1.1 the lowest order Feynman diagram for electron-proton elastic scattering is shown.

This process is described by  $d\sigma/dq^2 \propto \mathcal{M}^2$  where  $\mathcal{M}$  is the Lorentz invariant

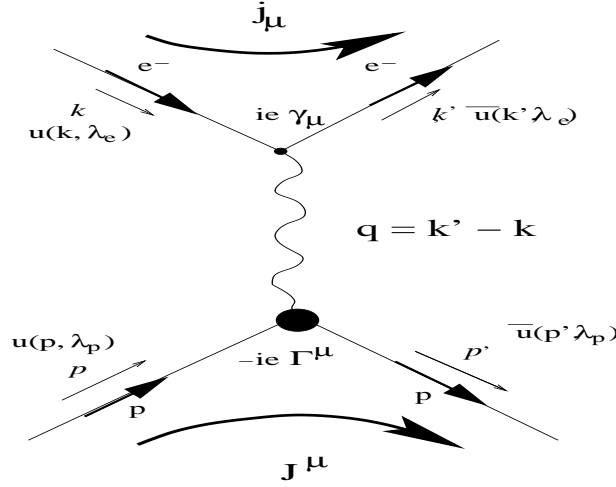


Figure 1.1: The lowest order Feynman diagram of the  $e^-p \rightarrow e^-p$  scattering. (All quantities are described in the text following Eq. (1.3).)

amplitude for this process due to one photon exchange given by:

$$\begin{aligned} \mathcal{M} &\sim \langle p | J^\mu | p \rangle \cdot \frac{1}{q^2} \cdot \langle e | j_\mu | e \rangle \\ &= \frac{4\pi\alpha}{q^2} \bar{u}(\vec{p}', \lambda_p) \Gamma^\mu u(\vec{p}, \lambda_p) \cdot \bar{u}(\vec{k}', \lambda_e) \gamma_\mu u(\vec{k}, \lambda_e) \end{aligned} \quad (1.3)$$

where  $\bar{u}$  ( $u$ ) is a spinor for creating (annihilating) spin-half particle,  $\vec{p}$  ( $\vec{p}'$ ) and  $\vec{k}$  ( $\vec{k}'$ ) represent the momenta of the in-coming (out-going) proton and electron, respectively, and  $\lambda$  is the helicity of corresponding particle.  $\Gamma^\mu$  accounts for the EM interaction of the proton and includes the form factors: The corresponding quantity for the point-like electron is simply the Dirac matrix  $\gamma_\mu$ .

In quantum mechanics the magnetic moment  $\vec{\mu}$  of an electron is given by:

$$|\mu_z| = g \frac{e}{2m_e c} |S_z| = \frac{e\hbar}{2m_e c} (1 + k_e) \quad (1.4)$$

where  $g$  is the Landé g-factor (or gyromagnetic ratio) and  $k_e$  ( $= \frac{g-2}{2}$ ) is the anomalous magnetic moment of an electron. The value of  $k_e$  was first calculated by

Schwinger in 1947 to be about 0.00116 from a correction to the vertex that included the emission and absorption of a virtual photon as shown in the Feynman diagram below, Figure 1.2.



Figure 1.2: Vertex correction term responsible for the anomalous magnetic moment of the electron.

This mechanism by itself, however, did not explain the huge anomalous magnetic moment of the proton ( $k_p = 1.79$ ). Instead it turned out to be due to the fact that the proton has structure rather than being point-like, like an electron. One may then write the expression for  $\Gamma^\mu$  in the following way that satisfies Lorentz invariance, current conservation, and parity conservation:

$$\Gamma^\mu = \gamma^\mu F_1(Q^2) + \frac{i\sigma^{\mu\nu}q_\nu}{2M_p} F_2(Q^2) \quad (1.5)$$

where  $F_1(Q^2)$  and  $F_2(Q^2)$  are the Dirac and Pauli form factors. In the non-relativistic limit they are the Fourier transforms of the charge and anomalous magnetic moment distributions, respectively. At  $Q^2 = 0$ ,  $F_1$  reduces to just the total electric charge  $e$  and  $F_2$  becomes the anomalous magnetic moment in units of the nuclear magnetic moment ( $\mu_N = \frac{e\hbar}{2M_p}$ ) for the proton.

In 1950 Rosenbluth calculated the cross-section of elastic  $e^-p$  scattering based on single photon exchange [6]. The result can be written in the lab frame as:

$$\left(\frac{d\sigma}{d\Omega}\right)_{e^-p \rightarrow e^-p} = \left(\frac{d\sigma}{d\Omega}\right)_{Mott} \left[ \frac{G_E^2 + \tau G_M^2}{1 + \tau} + 2\tau G_M^2 \tan^2 \left( \frac{\theta_e}{2} \right) \right] \quad (1.6)$$

where  $\tau \equiv \frac{Q^2}{4M_p^2}$  and  $\left(\frac{d\sigma}{d\Omega}\right)_{Mott}$  is the ‘‘Mott cross section’’ corresponding to the scattering of an electron by a hypothetical point-like spinless charged particle of mass  $M_p$ :

$$\left(\frac{d\sigma}{d\Omega}\right)_{Mott} = \frac{\alpha^2 E_e' \cos^2(\theta_e/2)}{4E_e^3 \sin^4(\theta_e/2)} \quad (1.7)$$

and  $E_e$  ( $E_e'$ ) is the energy of the incident (scattered) electron with the scattering angle of  $\theta_e$ . From kinematics we have:

$$\frac{E_e'}{E_e} = \left[ 1 + 2\frac{E_e}{M_p} \sin^2 \left( \frac{\theta_e}{2} \right) \right]^{-1}. \quad (1.8)$$

The two terms  $G_E$  and  $G_M$  are the electric and magnetic Sachs form factors, which are defined as:

$$G_E(Q^2) \equiv F_1(Q^2) + \frac{t}{4M_p^2} F_2(Q^2) \quad (1.9)$$

$$G_M(Q^2) \equiv F_1(Q^2) + F_2(Q^2) \quad (1.10)$$

where  $t$  is one of the Mandelstam variables <sup>2</sup> defined as  $t \equiv q^2$  ( $\equiv -Q^2$ ).

$G_E$  and  $G_M$  at  $Q^2 = 0$  correspond to electric charge and magnetic current distributions in the non-relativistic limit. The benefit of using  $G_E(Q^2)$  and  $G_M(Q^2)$  instead of  $F_1(Q^2)$  and  $F_2(Q^2)$  is that there is no cross-term of the form  $G_E G_M$  in the expression (Eq. (1.6)) for the differential cross section. Thus separate measurements of  $G_E(Q^2)$  and  $G_M(Q^2)$  are possible and from them  $F_1(Q^2)$  and  $F_2(Q^2)$  can

---

<sup>2</sup>The variable  $t$  should be replaced by  $s$  ( $\equiv q^2 \equiv +Q^2$ ) in the time-like region.

be calculated. The first measurement of the EM form factors of the proton was performed in an elastic  $e^-p$  scattering experiment by Hofstadter's group at Stanford during the period of 1953-1956. They used an electron beam with energies of 100, 188, and 236 MeV incident on a gaseous hydrogen target and their results are shown in Figure 1.3 [7]: Their data did not match either the Mott curve, or the fit assuming that the proton had a point-charge and point-magnetic moment. Their result clearly indicated that the proton had to have a structure.

Since then, measurements of the EM form factors of the proton have been performed by many other groups both in the space-like and in the time-like regions. In the space-like region experimental data currently exist up to  $Q^2 = 31.3 \text{ GeV}^2$ , while in the time-like region the data exist up to  $Q^2 \sim 15 \text{ GeV}^2$ .

Traditionally all the determinations of  $G_E$  and  $G_M$  have been made with cross section measurements that use the Rosenbluth separation technique for an unpolarized electron beam. This technique is based on the reasoning that Eq. (1.6) can be rewritten as a reduced cross section,  $\sigma_R$ , where

$$\sigma_R \equiv \left( \frac{d\sigma}{d\Omega} \right)_{e^-p \rightarrow e^-p} \cdot \frac{\epsilon(1+\tau)}{(d\sigma/d\Omega)_{Mott}} = \tau G_M^2(Q^2) + \epsilon G_E^2(Q^2) \quad (1.11)$$

with  $\epsilon \equiv \left[ 1 + 2(1+\tau) \tan^2 \left( \frac{\theta_e}{2} \right) \right]^{-1}$ , the longitudinal polarization of the virtual photon. The above equation is a linear function of  $\epsilon$  for a fixed  $Q^2$ : The reduced cross section ( $\sigma_R$ ) is measured as a function of the  $\epsilon$  by changing the beam energy and measuring different values of  $\theta_e$  to maintain  $\tau$  constant. Since Eq. (1.11) is a linear equation, its slope gives a measurement of  $G_E$  and the intersection gives a measurement of  $G_M$ : Figure 1.4 shows schematically the Rosenbluth separation method.

However, with this method relatively precise measurements of  $G_E$  have only been carried out for  $Q^2 \leq 6 \text{ GeV}^2$ . This is especially because the  $G_M$  term contributes much more significantly than  $G_E$  at high  $Q^2$  due to the  $\tau$  ( $\equiv \frac{Q^2}{4M_p^2}$ ) term that multiplies  $G_M$  (see Eq. (1.6)). Thus measurements of  $G_E$  by the Rosenbluth method lead to large errors when  $Q^2$  is greater than 6  $\text{GeV}^2$ . In spite of this limitation in

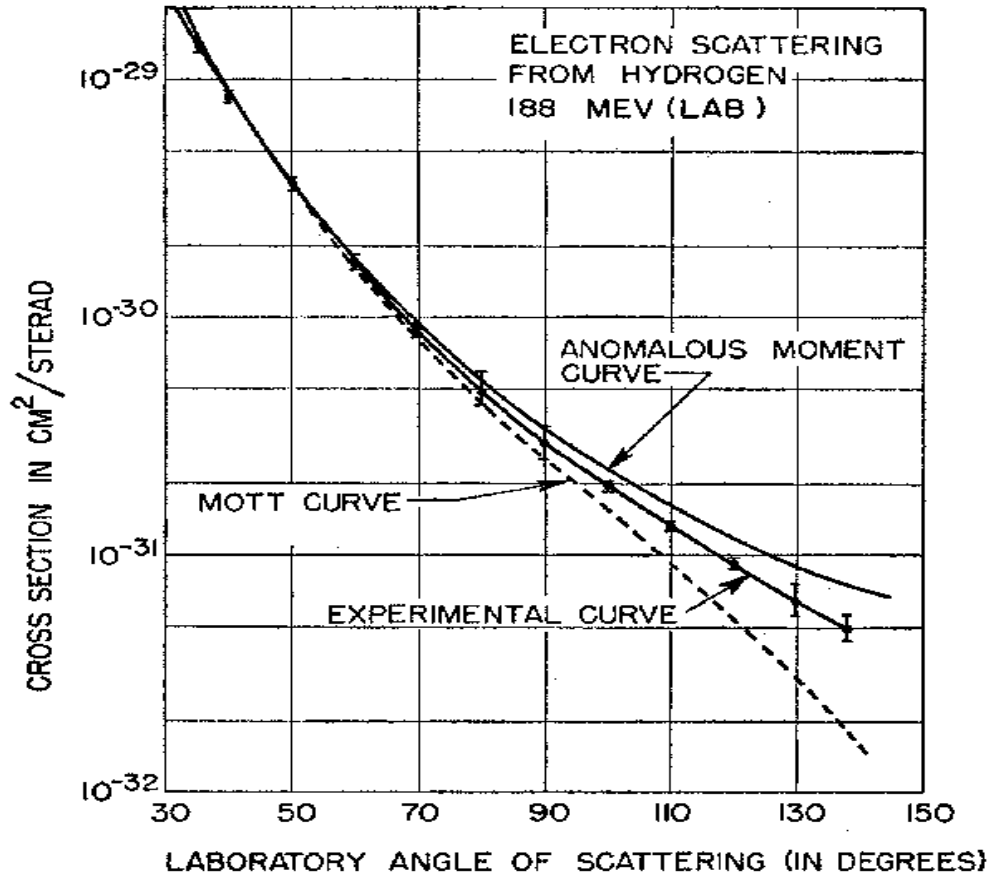


Figure 1.3: The first measurement of the proton structure in  $e^-p$  scattering (adapted from [7]).

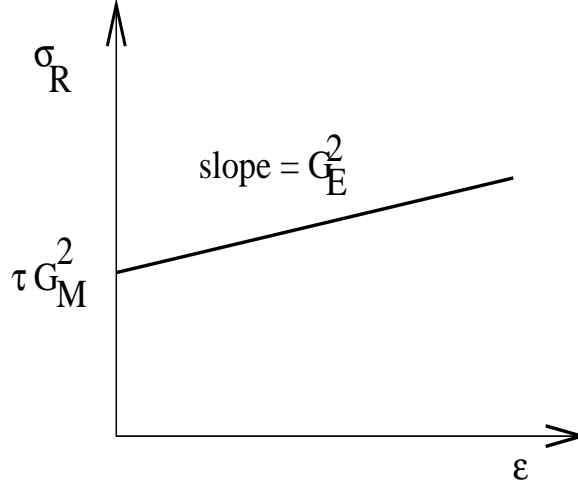


Figure 1.4: Schematic of the Rosenbluth separation method.

the measurement of  $G_E$  an empirical relationship between the two EM form factors of the proton in the space-like region has been established. It is simply:

$$\mu_p \frac{G_E}{G_M} = 1 \quad (1.12)$$

where  $\mu_p = 2.79$  is the magnetic moment of the proton in units of the nuclear magneton, while  $\frac{G_M}{\mu_p}$  was found to be described by the following (also empirical) relationship:

$$\frac{G_M}{\mu_p} = \left(1 + \frac{Q^2}{0.71 \text{ GeV}^2}\right)^{-2} \equiv G_D \quad (1.13)$$

where the dipole form factor,  $G_D$ , is the Fourier transform of an exponential charge distribution ( $\rho(r) \approx e^{-\sqrt{0.71}r}$ ) in the non-relativistic limit (see Table 1.1).

There exists now an alternative way to measure the ratio of the space-like form factors of the proton using the scattering of longitudinally polarized electrons [8, 9, 10], which was first proposed in 1968 [8]. In this method the transverse ( $P_t$ ) and longitudinal ( $P_l$ ) polarizations of the initially unpolarized recoil proton, the energies

of incident and scattered electrons ( $E_e$  and  $E'_e$ ) and the scattering angle ( $\theta_e$ ) of the electron, are measured to extract the ratio of the form factors that is given by [10]:

$$\frac{G_E}{G_M} = -\frac{P_t}{P_l} \frac{(E_e + E'_e)}{2M_p} \tan\left(\frac{\theta_e}{2}\right) \quad (1.14)$$

Separate measurements of  $G_E$  and  $G_M$  are also possible by additional measurement of  $I_0$  which has a direct relationship with the Rosenbluth cross section:

$$\frac{d\sigma}{d\Omega} = \left(\frac{d\sigma}{d\Omega}\right)_{Mott} \cdot \frac{I_0}{1 + \tau} \quad (1.15)$$

where

$$I_0 \equiv G_E^2(Q^2) + \frac{\tau}{\epsilon} G_M^2(Q^2) \quad (1.16)$$

$G_E$  and  $G_M$  can be determined via the following relationships:

$$I_0 P_l = \frac{E_e + E'_e}{M} \sqrt{(1 + \tau)} G_M^2 \tan^2\left(\frac{\theta_e}{2}\right) \quad (1.17)$$

$$I_0 P_t = -2\sqrt{(1 + \tau)} G_E G_M \tan\left(\frac{\theta_e}{2}\right). \quad (1.18)$$

This technique does allow for precision measurements of  $G_E$  at high  $Q^2$  since the transverse polarization term ( $I_0 P_t$ ) which contains an interference of  $G_E$  and  $G_M$ . Hence this technique works better in high  $Q^2$  than the Rosenbluth separation method, while the reverse is true at low  $Q^2$ . Experimentally this method had not been feasible until recently due to the difficulties of producing intense polarized electron beams and of making polarization measurements at energies of order 1 GeV.

The first measurement of the ratio  $\frac{G_E}{G_M}$  using this method was performed at the MIT-Bates Linear Accelerator Center at low  $Q^2$  ( $< 1 \text{ GeV}^2$ ) and the result showed the same scaling behavior that obtained with the Rosenbluth method [11]. Recently



an experiment (E01-001) at Jefferson Lab (JLab) has measured the value of  $\frac{G_E}{G_M}$  up to  $Q^2 = 5.6 \text{ GeV}^2$  [12, 13] and it was observed that the simple scaling of Eq. (1.12) fails for  $Q^2 > 1 \text{ GeV}^2$ . In this region the value of  $G_E$  falls faster than the dipole ( $G_D$ ) approximation and, since both techniques can give relatively precise measurements of the two form factors, there is a discrepancy between these two methods. The  $G_M$  measurements by two methods kept the same scaling behavior of dipole ( $G_D$ ) up to  $Q^2 \sim 6 \text{ GeV}^2$  within an error of 5%. However a result by Sill et al. [16] using polarization method showed  $G_M$  measurements fell faster than  $G_D$  in the range of  $\sim 6 \text{ GeV}^2$  up to  $\sim 12 \text{ GeV}^2$  [15], but there has been no experiment confirming their result yet. See Figure 1.5.

Figure 1.6 shows the ratio  $\mu_p \frac{G_E}{G_M}$  as a function of  $Q^2$  as obtained by the two methods described above [15]. The JLab measurements of polarization data up to  $Q^2 \sim 6 \text{ GeV}^2$  are fit by:

$$\mu_p \frac{G_E}{G_M} = 1 - 0.13 \left( \frac{Q^2}{\text{GeV}^2} - 0.04 \right) \quad (1.19)$$

These results indicate that the electric charge distribution of the proton is more spatially extended than the magnetic one: If they are correct then the discrepancy can perhaps be due to the failure of the physical assumption of one photon exchange made in the Rosenbluth cross section formula, or maybe that there is a significant error in the measurements. An experiment designed to investigate this discrepancy is continuing at JLab (experiment E01-001) which is to make precise measurements of  $\mu_p \frac{G_E}{G_M}$  using the Rosenbluth technique [17] [18]. Future measurements of  $\mu_p \frac{G_E}{G_M}$  up to  $Q^2 = 9 \text{ GeV}^2$  are also planned in JLab experiment E01-109 [19].

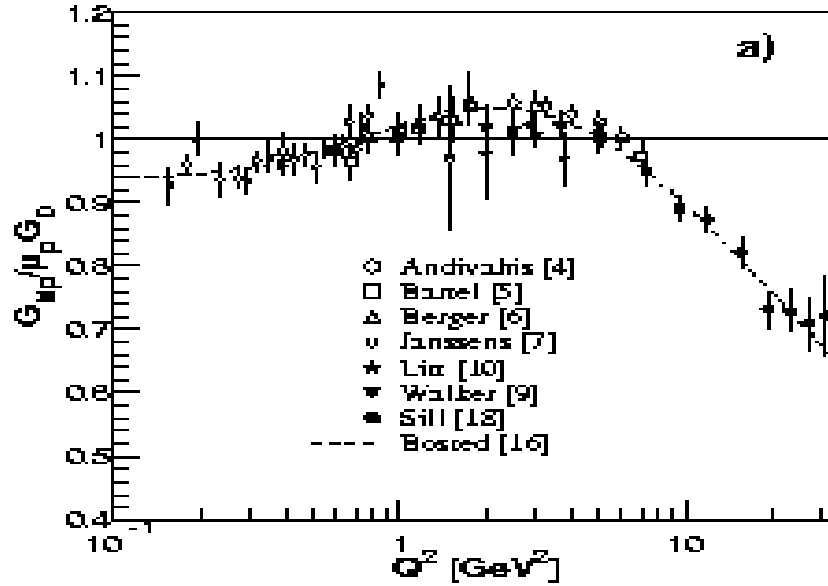


Figure 1.5: Dipole scaling ( $G_D$ ) behavior of  $G_M$  both in Rosenbluth technique (hollow square) and polarization technique (filled circle) up to  $6 \text{ GeV}^2$  (adapted from [15]).

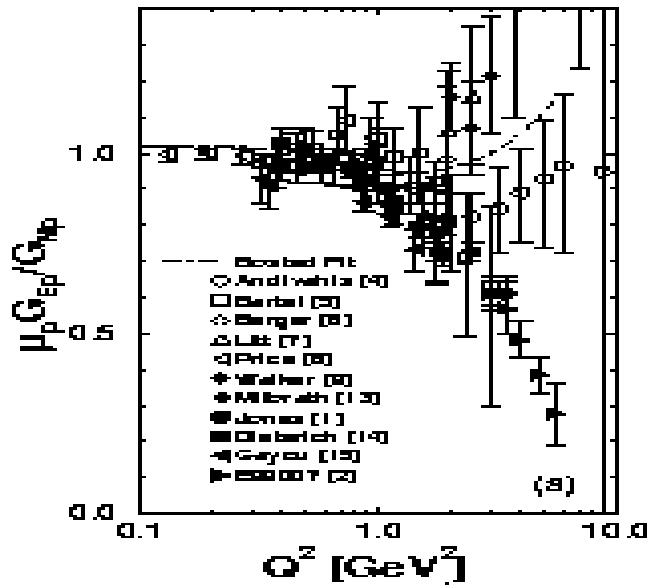


Figure 1.6: Discrepancy between the Rosenbluth technique (hollow) and polarization technique (filled circle). (adapted from [15]). See text.

## 1.2 Form Factors in the Time-like Region

Form factors in the time-like region show different features from those in the space-like region, due to the presence of resonances (poles) and continuum (branch-cuts) at thresholds at  $s = 4M_p^2$  and above. Figure 1.7 shows the lowest order Feynman diagram of the  $\bar{p}p \rightarrow e^+e^-$  process.

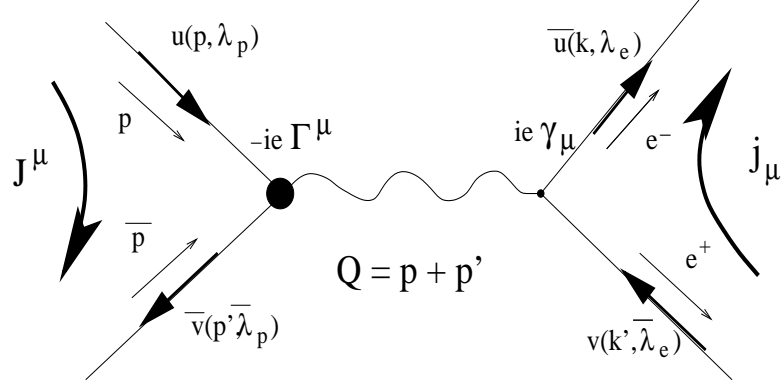


Figure 1.7: The lowest order Feynman diagram of the  $\bar{p}p \rightarrow e^+e^-$  process.

The invariant amplitude  $\mathcal{M}$  of this process is:

$$\begin{aligned} \mathcal{M} &\sim \langle 0 | J^\mu | \bar{p}p \rangle \cdot \frac{1}{q^2} \cdot \langle e^+e^- | j_\mu | 0 \rangle \\ &= \frac{4\pi\alpha}{q^2} \bar{v}(\vec{p}', \bar{\lambda}_p) \Gamma^\mu u(\vec{p}, \lambda_p) \cdot \bar{u}(\vec{k}, \lambda_e) \gamma_\mu v(\vec{k}', \bar{\lambda}_e) \end{aligned} \quad (1.20)$$

where  $\bar{v}$  ( $v$ ) is a spinor for annihilating (creating) spin-half anti-particle, with the same definition as for the space-like diagram.

$\Gamma^\mu$  in the time-like region can be obtained by applying crossing symmetry to  $\Gamma^\mu$  in the space-like region (Eq. (5)), which leads to:

$$\Gamma^\mu = \gamma^\mu F_1(Q^2) - \frac{i\sigma^{\mu\nu} q_\nu}{2M_p} F_2(Q^2) \quad (1.21)$$

Using the following Gordon identity in the time-like region,

$$\bar{v}(\vec{p}', \bar{\lambda}_p) \gamma^\mu u(\vec{p}, \lambda_p) = \bar{v}(\vec{p}', \bar{\lambda}_p) \left[ \frac{(p - p')^\mu}{2M_p} - i \frac{\sigma^{\mu\nu} q_\nu}{2M_p} \right] u(\vec{p}, \lambda_p) \quad (1.22)$$

$\Gamma^\mu$  in Eq. (1.21) can be rewritten as:

$$\Gamma^\mu = \gamma^\mu (F_1(Q^2) + F_2(Q^2)) + \frac{(p' - p)^\mu}{2M_p} F_2(Q^2). \quad (1.23)$$

In 1962 Zichichi et al. first calculated the cross section in the time-like region [20]:

$$\left( \frac{d\sigma}{d\Omega} \right)_{\bar{p}p \rightarrow e^+e^-} = \frac{\alpha^2}{4\beta_p s} \cdot \left[ |G_M|^2 (1 + \cos^2 \theta) + \frac{4M_p^2}{s} |G_E|^2 \sin^2 \theta \right] \quad (1.24)$$

where,  $\theta$  is the scattering angle of the electron in the center-of-mass system (CM) and  $\beta_p$  is the velocity of the proton in the CM, given by  $\beta_p \equiv \sqrt{1 - 4M_p^2/s}$ . The cross section for the inverse process ( $e^+e^- \rightarrow \bar{p}p$ ) can be obtained from detailed balance [3]:

$$\left( \frac{d\sigma}{d\Omega} \right)_{e^+e^- \rightarrow \bar{p}p} = \beta_p^2 \left( \frac{d\sigma}{d\Omega} \right)_{\bar{p}p \rightarrow e^+e^-}. \quad (1.25)$$

The value of the cross-section in the time-like region falls quickly with increasing momentum transfer and this makes separate measurements of  $|G_M|$  and  $|G_E|$  very difficult due to limited statistics in the continuum. So far, in the time-like region  $|G_M|$  is extracted from data by making one of two different assumptions: either  $|G_E| = |G_M|$  or  $|G_E| = 0$ . The first equality holds only at threshold ( $s = 4M_p^2$ ), while the

second appears somewhat arbitrary. Table 1.2 is a compendium of all the results for  $|G_E|$  of the proton in the time-like region: all made that  $|G_E| = |G_M|$ .

Experiment E760, the predecessor experiment of E835, was the first experiment to measure the magnetic form factor of the proton at high  $Q^2$  ( $> 9 \text{ GeV}^2$ ) and found that the results obtained for  $|G_M|$  values were insensitive to the choice of assumption [23]. All the time-like measurements of  $|G_M|$  are plotted in Figure 1.8.

A measurement of the form factor ratio ( $|\frac{G_E}{G_M}|$ ) is also possible from the angular distribution of the process  $\bar{p}p \rightarrow e^+e^-$ , or its inverse. The event rate as a function of the center-of-mass (CM) angle  $\theta^*$  is:

$$\frac{dN}{d\cos\theta^*} \propto |\overline{\mathcal{M}}|^2 \propto 1 + \lambda \cos^2 \theta^* \quad (1.26)$$

and then

$$\left| \frac{G_E}{G_M} \right| = \frac{\sqrt{s}}{2M_p} \sqrt{\frac{1-\lambda}{1+\lambda}}. \quad (1.27)$$

where,  $\theta^*$  is the angle between an electron and  $\bar{p}$  direction in the CM system. A full derivation is given in Appendix A.

The relative helicities for  $\bar{p}p$  annihilation into one photon are 0 and 1 due to the quantum numbers of the photon ( $1^{--}$ ): The amplitudes  $C_0$  and  $C_1$  for relative helicity 0 and 1, respectively, are proportional to  $|\frac{2M_p}{\sqrt{s}}G_E|$  and  $|G_M|$ . With the normalization condition  $|C_0|^2 + 2|C_1|^2 = 1$ , the relative helicity amplitude ratio can be written as:

$$\left| \frac{C_0}{C_1} \right| = \sqrt{\frac{1-\lambda}{1+\lambda}} \quad (1.28)$$

This result is derived in Appendix B using the helicity formalism [21].

In the region of applicability of perturbative QCD (pQCD) at large  $Q^2$  and far from any resonances, this ratio is expected to vanish: In this limit, the basic QCD interaction only allows the annihilation of quarks of a given helicity with anti-quarks of the opposite helicity. Several measurements of the parameter  $\lambda$  have been made at the  $J/\psi$  resonance ( $s = 9.61 \text{ GeV}^2$ ) in the process  $e^+e^- \rightarrow \bar{p}p$ . Table 1.3 lists the

results, the extracted ratios of the Sachs form factors and the ratios of the helicity amplitudes at the  $J/\psi$ .

There are several predictions of  $\lambda$  at the  $J/\psi$  and  $\psi'$ . The prediction by Claudson et al. was based on the assumption that  $|G_E| = |G_M|$  [75]. In Carimalo's prediction, a crude estimate was made of quark mass effects ( $m_q \sim \frac{M_p}{3}$ ) in the proton wave function [76]. Table 1.4 gives their predictions for  $\lambda$ , the extracted ratios and the ratios of the helicity amplitudes at the  $J/\psi$  and  $\psi'$ . The subject of this thesis is to measure the angular distribution of  $\bar{p}p \rightarrow e^+e^-$  at the  $\psi'$  resonance ( $s = 13.54 \text{ GeV}^2$ ) and then to extract the  $\left|\frac{G_E}{G_M}\right|$  and  $\left|\frac{C_0}{C_1}\right|$ .

In the following section, the asymptotic properties of the form factors will be briefly discussed for completeness.

### 1.3 Asymptotic Property of Form Factors

Long before QCD became the accepted theory of the strong interaction, Sachs discussed the high energy behavior of form factors in the space-like region. Sachs's argument was that as  $Q^2$  goes to infinity, a bare nucleon should be seen with its bare charge and magnetic moment so that [32]:

$$G_E \rightarrow Z_2 q, \quad G_M \rightarrow Z_2 \frac{q}{2M} \quad (1.29)$$

where  $Z_2$  is a constant,  $q$  is the charge, and  $M$  is the mass of the nucleon. Sachs made the point that if  $Z_2$  is zero at high  $Q^2$ , then the particle is composite but if  $Z_2$  is a non-zero constant at high  $Q^2$ , then the particle is fundamental.

In the lowest order pQCD, the quark counting rules [33, 34] predicts the following relation:

$$G_M(Q^2) \sim F_1(Q^2) \sim \frac{1}{Q^4} \quad (1.30)$$

The above scaling behavior, however, is modified by quark-gluon and gluon-gluon

$s$ (GeV <sup>2</sup> )	$ G_M  \times 10^2$	# of events	Experiment (Machine, Lab)	Year
3.52	51±8	29	ELPAR (PS, CERN)	1977
3.52	53 <sup>+6</sup> <sub>-8</sub>	1830	PS-170 (LEAR, CERN)	1994
3.55	39±5	34	PS-170 (LEAR, CERN)	1991
3.57	34±4	40	PS-170 (LEAR, CERN)	1991
3.60	31±3	50	PS-170 (LEAR, CERN)	1991
3.61	46 <sup>+15</sup> <sub>-9</sub>	5	ELPAR (PS, CERN)	1977
3.69	36±5	16	FENICE (Adone, Frascati)	1994
3.69	28.1±1.4	348	PS-170 (LEAR, CERN)	1991
3.76	25.5±1.3	375	PS-170 (LEAR, CERN)	1991
3.8	39±6	16	DM-1 (DCI, Orsay)	1979
3.83	24.9±1.0	284	PS-170 (LEAR, CERN)	1991
3.9	25±8	9	DM-1 (DCI, Orsay)	1979
3.94	24.6±1.1	210	PS-170 (LEAR, CERN)	1991
4.0	26±3	22	DM-2 (DCI, Orsay)	1983
4.00	24±3	18	FENICE (Adone, Frascati)	1994
4.1	26±3	27	DM-1 (DCI, Orsay)	1979
4.18	23.7±0.9	496	PS-170 (LEAR, CERN)	1991
4.2	22±2	24	DM-2 (DCI, Orsay)	1983
4.4	27±4	25	Castellano et al. (Adone, Frascati)	1973
4.4	19±2	20	DM-2 (DCI, Orsay)	1983
4.41	22±2	28	FENICE (Adone, Frascati)	1994
4.6	21±4	11	DM-1 (DCI, Orsay)	1979
4.6	17±2	17	DM-2 (DCI, Orsay)	1983
4.8	19±2	19	DM-2 (DCI, Orsay)	1983
5.0	14±4	3	DM-2 (DCI, Orsay)	1983
5.1	<20	-	Hartill et al. (AGS, BNL)	1969
5.69	8.4 <sup>+1.7</sup> <sub>-1.3</sub>	7	DM-2 (DCI, Orsay)	1990
5.95	15±3	-	FENICE (Adone, Frascati)	1994
6.6	<16	-	Hartill et al. (AGS, BNL)	1969
6.8	<25	-	Conversi et al. (PS, CERN)	1965
8.84	3.59 <sup>+0.18</sup> <sub>-0.19</sub>	93	E835 (AA, FNAL)	1999
8.9	<5.2	-	R-704 (ISR, CERN)	1985
8.9	14	3.3 <sup>+0.6</sup> <sub>-0.4</sub>	E-760 (AA, FNAL)	1993
9.6	21±3	14	DASP (DORIS, DESY)	1975
10.78	2.13 <sup>+0.70</sup> <sub>-0.84</sub>	3	E835 (AA, FNAL)	1999
11.63	1.74 <sup>+0.18</sup> <sub>-0.16</sub>	32	E835 (AA, FNAL)	2002
12.4	1.3 <sup>+0.3</sup> <sub>-0.2</sub>	11	E-760 (AA, FNAL)	1993
12.43	1.43 <sup>+0.12</sup> <sub>-0.13</sub>	33	E835 (AA, FNAL)	1999
12.43	1.48 <sup>+0.15</sup> <sub>-0.13</sub>	34	E835 (AA, FNAL)	2002
12.5	<4.2	-	R-704 (ISR, CERN)	1985
13.0	1.3 <sup>+0.5</sup> <sub>-0.3</sub>	4	E-760 (AA, FNAL)	1993
13.11	1.12±0.16	14	E-835 AA FNAL	1999
14.36	1.39 <sup>+0.91</sup> <sub>-0.54</sub>	1	E-835 (AA, FNAL)	1999
14.40	<1.38	-	E835 (AA, FNAL)	2002
18.22	<2.77	-	E835 (AA, FNAL)	2002
18.40	<4.40	-	E-835 (AA, FNAL)	1999

Table 1.2: All measurements of magnetic form factor of the proton in the time-like region under the assumption that  $|G_E| = |G_M|$ .

Experiment	$\lambda_{J/\psi}$	$\left \frac{G_E}{G_M}\right _{J/\psi}$	$\left \frac{C_0}{C_1}\right _{J/\psi}$
Mark I [24]	$1.45 \pm 0.56$	Unphysical	Unphysical
DASP [25]	$1.70 \pm 1.70$	Unphysical	Unphysical
Mark II [26]	$0.61 \pm 0.23$	$0.88 \pm 0.30$	$0.49 \pm 0.18$
DM2 [27]	$0.62 \pm 0.11$	$0.80 \pm 0.15$	$0.48 \pm 0.09$
Mark III [28]	$0.58 \pm 0.14$	$0.90 \pm 0.18$	$0.52 \pm 0.11$
World average [74]	$0.63 \pm 0.08$	$0.86 \pm 0.10$	$0.48 \pm 0.06$

Table 1.3: Measured values of  $\lambda$ ,  $\left|\frac{G_E}{G_M}\right|$  and  $\left|\frac{C_0}{C_1}\right|$  at the  $J/\psi$ .

Theory	$\lambda_{J/\psi}$	$\left \frac{G_E}{G_M}\right _{J/\psi}$	$\left \frac{C_0}{C_1}\right _{J/\psi}$	$\lambda_{\psi}$	$\left \frac{G_E}{G_M}\right _{\psi'}$	$\left \frac{C_0}{C_1}\right _{\psi'}$
Claudson et al. [75]	0.46	1.0 (input)	0.61	0.59	1.0 (input)	0.51
Carimalo [76]	0.69	0.69	0.42	0.80	0.65	0.33

Table 1.4: Predicted values of  $\lambda$ ,  $\left|\frac{G_E}{G_M}\right|$  and  $\left|\frac{C_0}{C_1}\right|$  at the  $J/\psi$  and  $\psi'$ .

interactions. These are mostly taken into account through the  $Q^2$  dependence of the effective coupling,  $\alpha_s$ , with an additional logarithmic term [35]:

$$\frac{G_M(Q^2)}{\mu_p} \sim \frac{C}{Q^4} \alpha_s^2(Q^2) \left[ \ln \left( \frac{Q^2}{\Lambda^2} \right) \right]^{-\frac{4}{3\beta}} \quad (1.31)$$

where,

$$\alpha_s(Q^2) = \frac{4\pi}{\beta \ln \left( \frac{Q^2}{\Lambda^2} \right)}, \text{ and } \beta = 11 - \frac{2}{3}n_f. \quad (1.32)$$

Here, the constant  $C$  can in principle be calculated given the wave function of the nucleon,  $\Lambda$  is the QCD scale parameter, and  $n_f$  is the number of flavors.

Since by the Phragmén-Lindelöf theorem [5], the form factors in the space-like region and in the time-like region should have the same asymptotic behavior in the region of large  $Q^2$ , it follows that the form factors in the time-like region become real



functions in the large  $Q^2$  limit, and the constant  $C$  from the two regions should be the same. To test this, the coefficient  $C$  in the space-like region ( $C_s$ ) was obtained in  $2.9 \text{ GeV}^2 < Q^2 < 31.3 \text{ GeV}^2$  region by Bilenky et al. [36] using data from SLAC [37], while in the time-like region  $C_t$  was obtained using data from E760 ( $Q^2 = 8.9, 12.4, 13.0 \text{ GeV}^2$ ) [23], the predecessor experiment of E835. The results showed that  $C_t$  is  $3\sigma$  higher than  $C_s$ . Recent  $G_M$  measurements by E835 ( $Q^2 = 11.63, 12.43, 14.40, \text{ and } 18.22 \text{ GeV}^2$ ) [38] have been consistent with the earlier results obtained by E760 and the first run of E835 ( $Q^2 = 8.8, 10.8, 12.4, 13.1, \text{ and } 14.4 \text{ GeV}^2$ ) [39], and their time-like  $G_M$  values were approximately a factor of two higher than space-like  $G_M$  values at  $Q^2 \approx 15.0 \text{ GeV}^2$ .

This can be understood to mean that the asymptotic pQCD region has not yet been reached at  $Q^2 \approx 15.0 \text{ GeV}^2$ . However, we note that experimental results both in the time-like and space-like regions seem to show the same functional dependence of  $Q^2$  as would be expected from the pQCD scaling behavior expressed in Eq. (1.31).

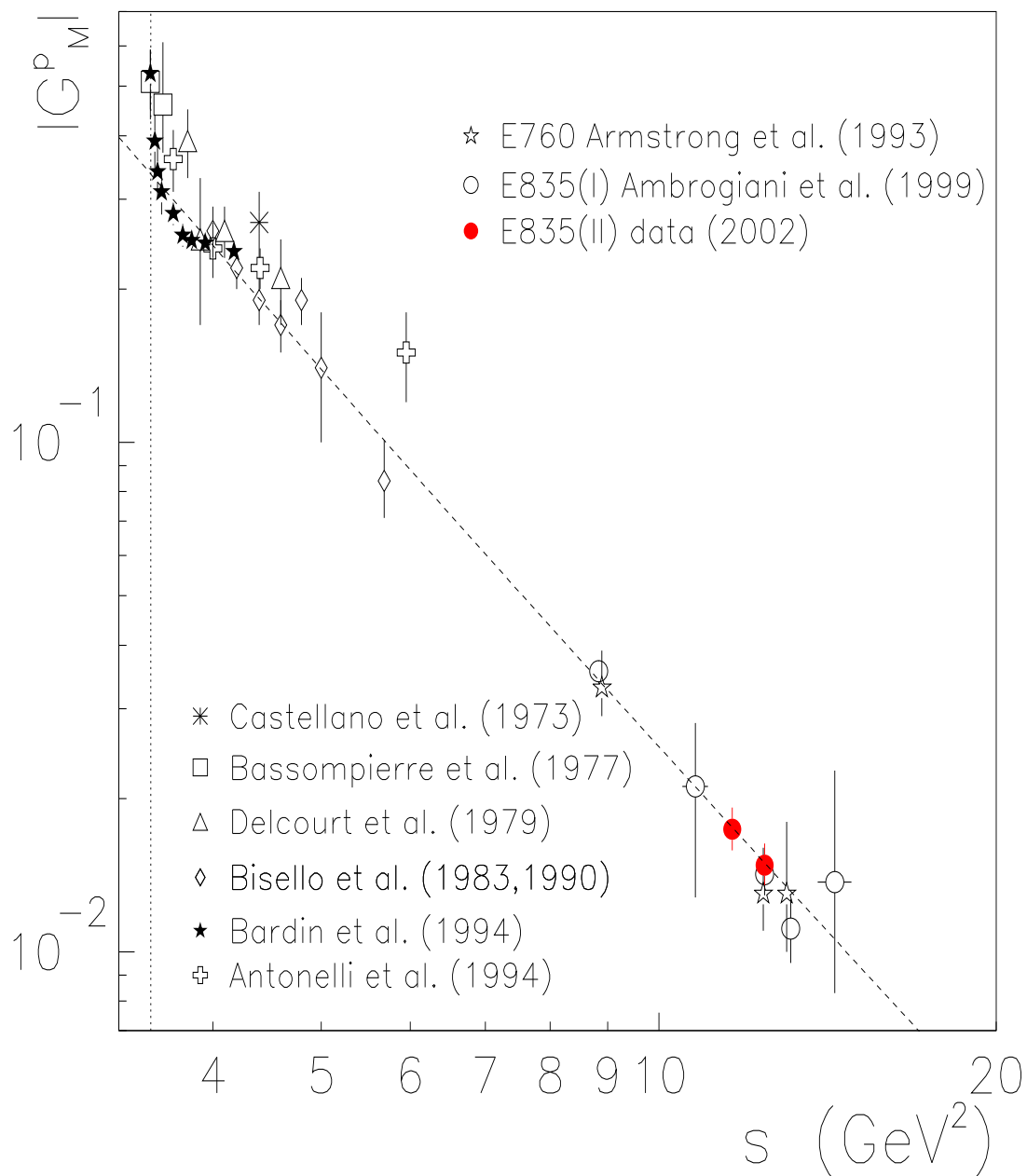


Figure 1.8: All measurements of  $|G_M|$  vs.  $Q^2$  in the time-like region under the assumption that  $|G_E| = |G_M|$  [38].

# Chapter 2

## Experimental Setup

The first matter–anti-matter collider was an  $e^+e^-$  machine called “Anello d’Accumulazione”<sup>1</sup> (AdA) built in Frascati in 1960. In 1978, acceleration and storage of intense antiproton ( $\bar{p}$ ) beams became possible with the invention of the “stochastic cooling” technique by van der Meer [40]. Using this technique, the first  $\bar{p}p$  collisions were observed in 1981 at the CERN  $SP\bar{P}S$  collider and led to the discovery of the  $W$  and  $Z$  bosons by the UA1 and UA2 experiments in 1983. After this success of the  $\bar{p}p$  collider in Europe, the Antiproton Accumulator was built at Fermilab and the Tevatron was able to achieve its first  $\bar{p}p$  collider run in 1986. Since then the Tevatron collider has been the highest energy machine in the world, with its best known achievement the discovery of the top quark in 1995.

This thesis concerns E835, a fixed target experiment at Fermilab using the  $\bar{p}$  beam in the accumulator incident on an internal hydrogen gas jet target. A stochastically cooled 8 GeV/c  $\bar{p}$  beam is stored in the Antiproton Accumulator (AA). The AA is a triangular shaped ring with a perimeter of 474 m. Figure 2.1 shows a schematic of the  $\bar{p}$  source, which consists the Main Injector<sup>2</sup> (MI) for the proton acceleration, the  $\bar{p}$  target station, transport lines, Debuncher (outer ring) for  $\bar{p}$  beam cooling and the AA (inner ring) for  $\bar{p}$  beam storage. The 120 GeV proton beam in

---

<sup>1</sup>Italian for “accumulation ring”. Its diameter was about 1 m.

<sup>2</sup>Its elliptical circumference is about 2 miles. The MI can accelerate protons from 8 GeV up to 120 GeV for  $\bar{p}$  production and 150 GeV for proton injection to the Tevatron.

the MI is sent to the target station and hits a nickel target <sup>3</sup> producing secondary particles. Of these, only negatively charged particles are focused by a lithium conducting lens, and a beam of nearly monoenergetic  $\bar{p}$ 's with 8 GeV/c momenta is sent to the Debuncher, where it is debunched and cooled. After debunching and cooling, the  $\bar{p}$  beam is sent to the AA for stacking and storage until it is used.

The following subsections describe in detail the process leading from  $\bar{p}$  beam production to dump. In addition, we describe the hydrogen gas jet target, luminosity monitor, control of the center-of-mass energy  $E_{CM}$ . Finally we will close this chapter by describing the experimental technique.

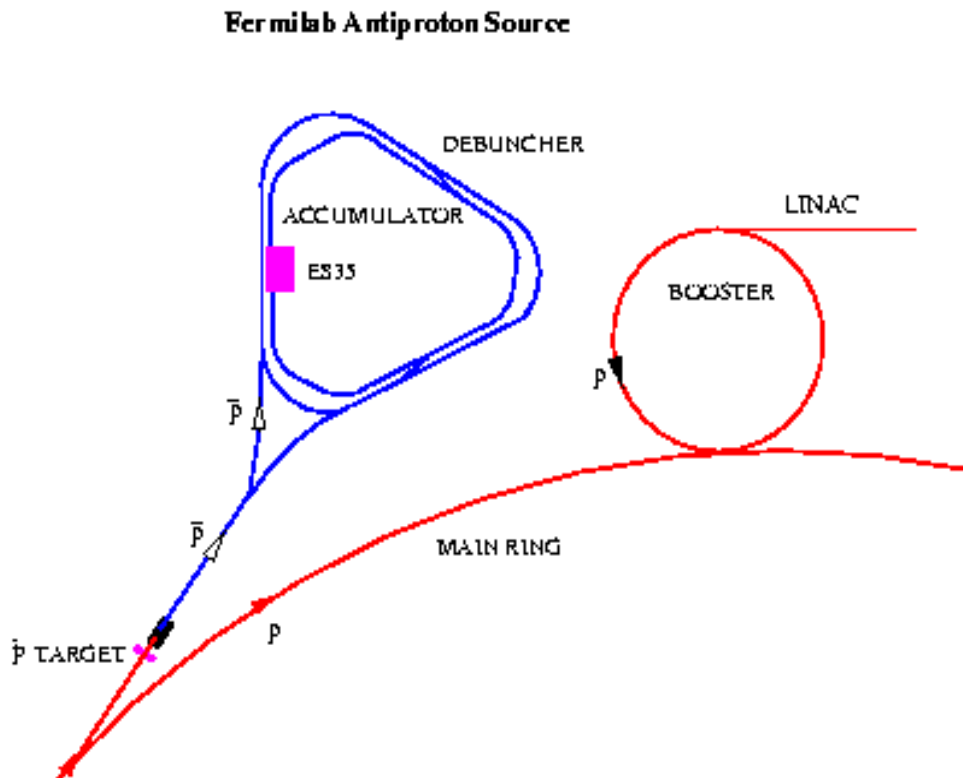


Figure 2.1:  $\bar{p}$  source at Fermilab.

---

<sup>3</sup>Nickel is chosen because it provides a good combination of  $\bar{p}$  yield and longevity under mechanical and heat stresses.

## 2.1 Antiproton ( $\bar{p}$ ) Beam

Five steps are needed to produce the  $\bar{p}$  beam for this experiment: production, cooling and storage (or stacking), deceleration, collision with target, and dump [41].

### 2.1.1 $\bar{p}$ Production

In the first step, the  $\bar{p}$ 's are produced by directing 120 GeV protons from MI onto a target where approximately 1  $\bar{p}$  is produced for every  $10^5$  protons on target.

A batch of protons (up to  $\sim 5 \times 10^{12}$  protons) <sup>4</sup> in the Main Injector (MI) are accelerated to 120 GeV <sup>5</sup> and are rotated by  $90^\circ$  in phase space to make a beam with small momentum spread and large time spread. These protons are sent to the target vault where they are focused to a small spot size by quadrupole magnets. Once focused, the protons strike a nickel target, producing secondary particles. The target disk is 10 cm in diameter and 2 cm in thickness. There is an air circulation hole in the middle through the target assembly cylinder. Copper disks are layered alternatively with nickel target disks to cool it.

The secondary particles produced in the target consist of several types of particles including  $\bar{p}$ 's. Only negatively charged secondaries are focused by a solid state lithium <sup>6</sup> conducting lens (2 cm diameter and 15 cm length cylinder) where the divergent beam becomes a collinear one by the induced magnetic fields <sup>7</sup> which are generated by currents passing through the lens. A pulsed dipole magnet follows the collection lens to select only particles with momentum of approximately 8 GeV/c. The 8 GeV/c is the peak in the  $\bar{p}$  production from the 120 GeV proton beam [41].

### 2.1.2 $\bar{p}$ Cooling and Storage

The selected negatively charged 8 GeV/c beam consists overwhelmingly of  $\bar{p}$ 's, because unstable particles originally present have decayed away. The  $\bar{p}$  beam at

---

<sup>4</sup>A batch of protons in MI is comprised of about 84 bunches injected with 53 MHz from Booster.

<sup>5</sup>The 120 GeV proton beam was optimized for  $\bar{p}$  production, involving considerations of targeting efficiency, repetition rate and constraints from the transport line [41].

<sup>6</sup>Lithium is the least-dense conductor, which minimizes scattering and absorption of the secondary particles.

<sup>7</sup>The operating field gradient is about 740 Tesla/m at a peak current of  $6.7 \times 10^5$  A [41].

this stage is bunched and has a large momentum spread: The next step is injection into the Debuncher where the beam is debunched and stochastically cooled.

Stochastic cooling is achieved by the combined action of pick-up and kicker electrodes. There are two types of stochastic coolings: betatron (transverse) cooling and momentum (longitudinal) cooling [40]. The betatron cooling technique is used to reduce the transverse beam size, or the betatron oscillations that are caused by the beam focusing magnets. The deviation of the  $\bar{p}$  beam particle from an ideal orbit is measured by a pick-up electrode and converted to the electrical signal: This signal is amplified and sent to a kicker electrode and the electrical impulse that corrects for the deviation is applied in time with arrival of the beam. The kicker is usually located at  $90^\circ$  apart in betatron phase from the pick-up, and thus the position displacement at the pick-up will be the angular displacement at the kicker. Figure 2.2 shows a schematic of the betatron cooling made possible by the pick-up and the kicker.

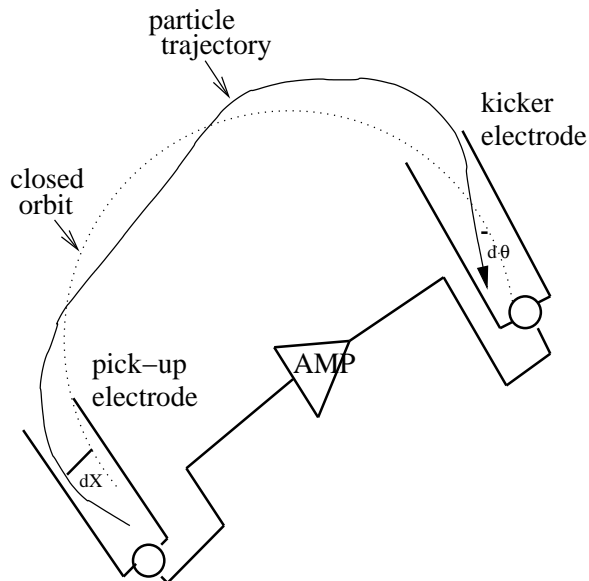


Figure 2.2: Schematic of stochastic (betatron) cooling (from [43]).

Momentum cooling is the method used to reduce beam momentum spread, which is critical for stacking of the  $\bar{p}$  beam. Depending on the types of pick-ups and kickers, momentum cooling is further classified into three methods: the Palmer, the filter,

and the transit time [44]. In E835, the Palmer cooling method was used. This is based on the correlation between the position and momentum in the high dispersion region of the machine (Debuncher and AA).

After stochastic cooling, the  $\bar{p}$  beam is transferred to the AA just before another batch of un-cooled beam arrives from the target station to the Debuncher [42].

The stored  $\bar{p}$  beam is kept at 8 GeV/c in the AA where it undergoes both betatron and momentum coolings until the desired amount in a stack is reached. The AA in Fermilab can stack up to  $2.2 \times 10^{12}$   $\bar{p}$ 's with a peak stacking rate of  $7.2 \times 10^{10}$   $\bar{p}$ /h [45]. During the 2000 run of E835 the average number of stacked  $\bar{p}$ 's was about  $4 \times 10^{11}$  with a typical stacking rate of  $3 \times 10^{10}$   $\bar{p}$ /h. Once in the AA, the  $\bar{p}$  beam had a lifetime of approximately 1000 hours under a vacuum level of  $3 \times 10^{-10}$  torr.

### 2.1.3 $\bar{p}$ Deceleration

Deceleration of the  $\bar{p}$  beam after stacking the desired amount of cooled 8 GeV/c  $\bar{p}$ 's, was performed at the AA to reach the momentum required for the experiment ( $4 \sim 9$  GeV/c). The deceleration rate was approximately 20 MeV/s and the total deceleration time until data taking for E835 was approximately 3 hours.

### 2.1.4 Collision and Data taking

During data taking the hydrogen gas jet target intercepted the antiproton beam which required continued stochastic cooling of the beam: Betatron cooling was applied to compensate for the increase of the beam emittance due to scattering with the residual gas in the target region and to compensate for energy losses in the target, while momentum cooling was applied to adjust the energy of the beam after its interaction with the target. The lifetime of the  $\bar{p}$  beam when the gas jet target was on was approximately 30 - 50 hrs depending on the stack size. The data taking time was approximately 1.5 times the  $\bar{p}$  beam lifetime  $\tau$  which is defined in terms of the number of  $\bar{p}$ 's  $N(t) = N_0 e^{-t/\tau}$ .

### 2.1.5 $\bar{p}$ Dump

As the  $\bar{p}$  beam density decreased, the jet density was increased to maintain an approximately constant instantaneous luminosity. The  $\bar{p}$  beam was dumped at the end of data taking when the beam density was too low for further compensating adjustments of the jet density to be possible.

## 2.2 The Hydrogen Gas Jet Target

In E835, hydrogen gas was selected as a target because the Fermi motion of nucleons in a heavier nuclear target would have caused a broadening of the  $c\bar{c}$  resonance.

To achieve a high instantaneous luminosity, a high target density was required, and thus the hydrogen gas was condensed into a much denser state of clusters or microdroplets. These clusters were formed by passing the hydrogen gas through a convergent and divergent nozzle (Figure 2.3 (left)) at low temperature ( $20 \sim 50$  K) and high pressure ( $10 \sim 100$  psi) with a typical cluster consisting of  $10^7 \sim 10^8$  hydrogen molecules. The nominal velocity of these hydrogen clusters was approximately 800 to 900 m/s depending on the nozzle pressure and the temperature of the jet. The direction of the hydrogen jet clusters was perpendicular to the  $\bar{p}$  beam direction and parallel to the ground (Figure 2.3 (right)): The cross sectional diameter of the jet target was 7 mm while that of the  $\bar{p}$  beam was 5 mm. The remnants of the hydrogen gas after the interaction were pumped out to reduce the contamination of the vacuum in the beam pipe.

The density of the hydrogen gas could be varied between  $10^{13} \sim 10^{14}$  atoms/cm<sup>3</sup> by adjusting the nozzle pressure and temperature. Figure 2.4 shows the nozzle pressure and temperature, and the corresponding jet target density. During data taking the operating pressure and temperature were set near the hydrogen saturation curve so as to obtain the highest possible instantaneous luminosity.

The nominal instantaneous luminosity was set as near as possible to  $\sim 2.5 \times 10^{31}$  cm<sup>-2</sup>sec<sup>-1</sup> during data taking. Figure 2.5 shows the density of the  $\bar{p}$  beam (decreasing line), the density of gas jet target (filled circles), and the instantaneous luminosity (white circles) as a function of time during a typical run.



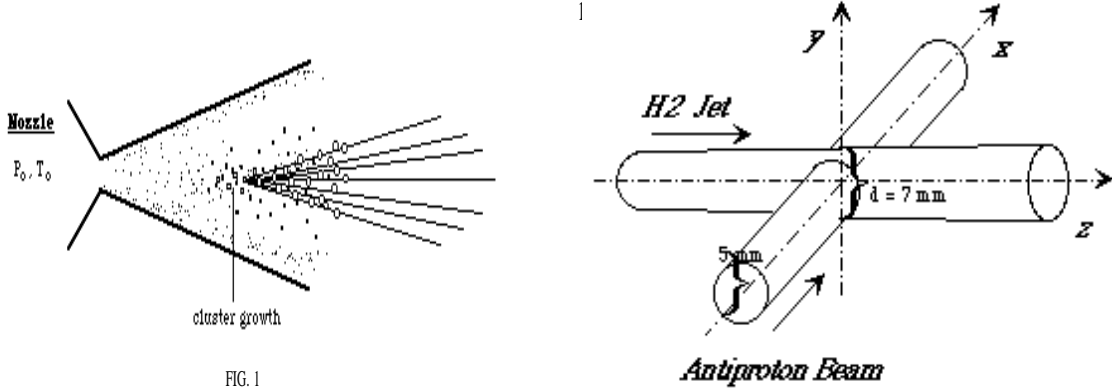


Figure 2.3: The formation of clusters of hydrogen gas jet target inside the trumpet shaped nozzle (left) and cross sectional view of the gas jet target perpendicular to the  $\bar{p}$  beam direction (right).

## 2.3 Luminosity Monitor

In order to measure the cross section for the production of a charmonium state, the absolute luminosity needs to be known to high precision. A monitor [47] was used which measured the recoil protons at normal angle corresponding to forward angle elastic scattering of  $\bar{p}$ 's. Total-energy-loss solid state detectors are ideal for recoil detection because they are compact and the energy resolution is excellent [47], and thus they were used in the E835 luminosity monitor.

The monitor was composed of three solid state detectors each with a surface area of  $1 \text{ cm} \times 5 \text{ cm}$  located  $150 \text{ cm}$  away underneath the  $\bar{p}p$  interaction point at  $4.6^\circ$  from the normal. The thickness of the detectors was  $\sim 500 \mu\text{m}$  which was sufficient to completely stop the recoil protons at this angle, where their kinetic energy was only a few MeV. Figure 2.6 shows the schematic of this detector: The central detector was movable but the two side detectors were fixed and located symmetrically on either side.

Measurement of the luminosity ( $\mathcal{L}$ ) was performed by counting the number ( $N$ ) of recoil protons with low momentum transfer ( $|t| < 0.05 \text{ GeV}^2$ ) where the elastic scattering of  $\bar{p}$  is the dominant process, and given by

# **JET DENSITY** **E835 run II**

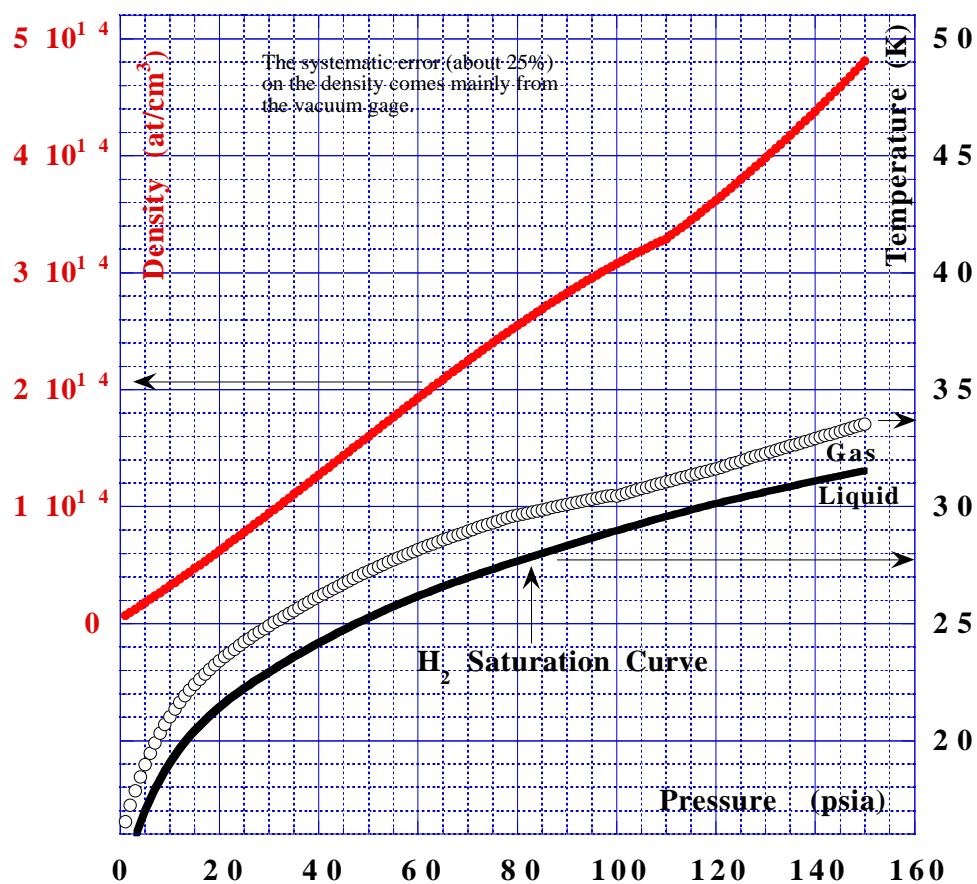
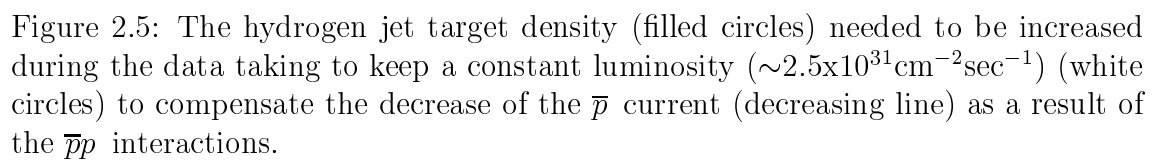


Figure 2.4: The hydrogen jet density vs. pressure curve for a given temperature (top line), operating temperature vs. pressure curve for a given density (open circles), and the hydrogen saturation curve (bottom line).



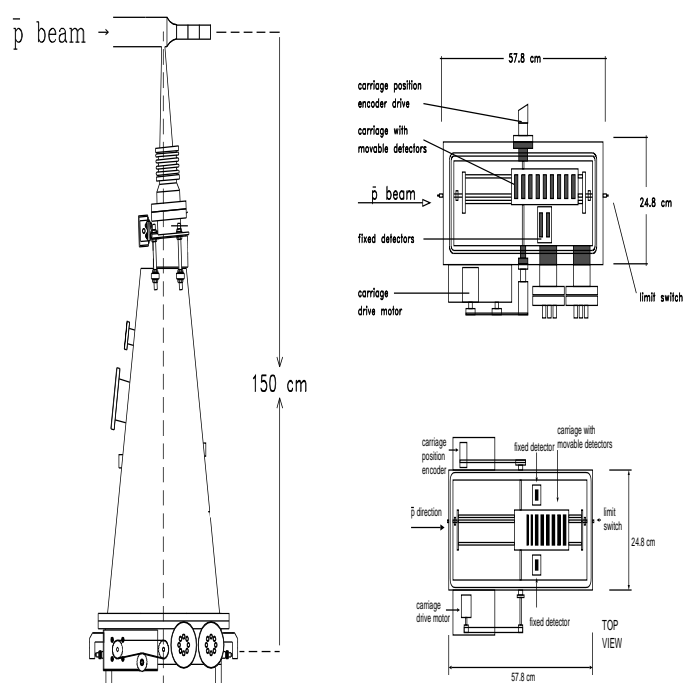


Figure 2.6: Luminosity monitor: side view (left and top right), top view (bottom right).

$$N = \mathcal{L} \cdot \int_{\Delta\Omega} \frac{d\sigma_{el}}{dt} \frac{dt}{d\Omega} d\Omega \quad (2.1)$$

where  $\frac{d\sigma_{el}}{dt}$  is the differential cross section for elastic  $\bar{p}p$  scattering and  $\Delta\Omega$  is the solid angle in the acceptance region.

The systematic error of the luminosity measurement was  $\sim 2.5\%$  while the statistical error was  $\sim 0.3\%$  for  $100 \text{ nb}^{-1}$ . The main sources of the systematic error were from the error in the fit to the world data for the cross section and the uncertainty in the detector solid angle. More details on the luminosity monitor can be found in reference [47].

## 2.4 Measurement of the Center of Mass Energy

A precise measurement of the  $\bar{p}$  beam energy was also critical to the experiment. The  $\bar{p}$  beam energy in the lab system ( $E_{lab}$ ) was determined indirectly by measuring the beam orbit length ( $L$ ) and revolution frequency ( $f_{rev}$ ) around the ring (AA) and then using the relationship:

$$E_{lab} = \frac{m_p c^2}{\sqrt{1 - \beta_{lab}^2}} = \frac{m_p c^2}{\sqrt{1 - \left(\frac{L f_{rev}}{c}\right)^2}} \quad (2.2)$$

where  $\beta_{lab} = \frac{L f_{rev}}{c}$  and  $m_p$  is the mass of the proton. From the lab energy of the beam, the total center of mass energy ( $E_{cm}$ ) can be found using a Lorentz transformation with the result:

$$\begin{aligned} E_{cm} &= \sqrt{2} m_p c^2 \sqrt{1 + \frac{E_{lab}}{m_p c^2}} \\ &= \sqrt{2} m_p c^2 \left( 1 + \frac{1}{\sqrt{1 - \left(\frac{L f_{rev}}{c}\right)^2}} \right)^{1/2}. \end{aligned} \quad (2.3)$$

From Eq. (2.3), the uncertainty in  $E_{cm}$  is calculated to be,

$$\frac{\delta E_{cm}}{E_{cm}} = \gamma_{lab} \left( \frac{pc}{E_{cm}} \right)^2 \left( \frac{\delta L}{L} + \frac{\delta f_{rev}}{f_{rev}} \right) \quad (2.4)$$

where  $\gamma_{lab} = \sqrt{1 - \beta_{lab}^2}$ . From Eq. (2.4) it can be seen that the uncertainty in  $E_{cm}$  depends on how well the orbit length and the revolution frequency are known. The nominal estimated uncertainty in orbit length  $\delta L$  was 1.2 mm while that in  $f_{rev}$  was  $\delta f_{rev}$  0.1 Hz [48]. Given the approximate orbit length and revolution frequency  $L \simeq 474$  m and  $f_{rev} \simeq 0.6$  MHz, the corresponding contributions to the uncertainty of  $E_{cm}$  at the  $\psi'$  resonance were 11 keV from  $\delta f_{rev}$  and 179 keV from  $\delta L$  [48]. Thus the main source of uncertainty in  $E_{cm}$  comparable to the widths of resonances like the  $J/\psi$  and  $\psi'$ , would come from  $\delta L$ : A precise measurement of  $L$  was called for and performed by beam position monitors (BPMs: a total of 48 horizontal and 42 vertical BPMs) at AA. The revolution frequency was measured by a spectrum analyser.

### 2.4.1 Measurement of the Orbit Length

A well measured resonance like the  $J/\psi$  or  $\psi'$  gave a precise orbit length which could be used as a “reference length” ( $L_{ref}$ ) and the measured orbit length was compared with this to obtain  $E_{cm}$ . The measurement of the orbit length ( $L$ ) was achieved by measuring the reference orbit length ( $L_{ref}$ ) and the difference between the two ( $\Delta L = L - L_{ref}$ ) with high precision. Reference [48] describes the method of obtaining  $\Delta L$  in detail.

From Eq. (2.3) the relationship between the resonance mass ( $M_{res}$ ) and  $L_{ref}$  is then:

$$M_{res} = \sqrt{2} m_p c^2 \left( 1 + \frac{1}{\sqrt{1 - \left( \frac{L_{ref} f_{rev}}{c} \right)^2}} \right)^{1/2}. \quad (2.5)$$

The error on  $L_{ref}$  arises mainly from the uncertainty in the value of the resonance mass ( $\delta M_{res}$ ) through the following relationship:

$$\delta L_{ref} = \frac{L_{ref} M_{res}}{\gamma_{lab} (pc)^2} \delta M_{res}. \quad (2.6)$$

At the  $\psi'$  ( $3686.00 \pm 0.090$  MeV<sup>2</sup>/c<sup>2</sup>), the value of  $\delta L_{ref}$  was 0.6 mm.

### 2.4.2 Measurement of the Revolution Frequency

To calculate  $E_{CM}$  in Eq. (2.3) and to measure the beam momentum distribution described in following section, the revolution frequency of the beam needs to be known.

When  $N$  charged particles ( $\bar{p}$ 's) with a mean revolution frequency ( $f_{rev}$ ) circulate, the random motion of the particles causes noise in addition to the main DC current of the beam ( $I_{DC} = Ne f_{rev}$ ). This is ‘‘Schottky noise’’, related to the root mean square of the beam current ( $I_{rms} = \sqrt{2N} e f_{rev}$ ) [49]. The noise in the current is detected at ‘‘Schottky pick-ups’’ where the number of beam particles is counted. To measure the frequency of the beam, the Schottky noise is sent to a spectrum analyser where a Fourier expansion of the current ( $I_{rms}$ ) is performed to measure the  $f_{rev}$  in the frequency domain [49]:

$$I_{rms}^2 = \left\langle \left[ \sum_{k=1}^N i(t; t_k) \right]^2 \right\rangle \quad (2.7)$$

with  $i(t; t_k)$  given by the Fourier expansion of the current for a single particle:

$$\begin{aligned} i(t; t_k) &= e \sum_m \delta(t - t_k - mT) \\ &= i_0 + \sum_{n=1}^{\infty} i_n \cos n\omega(t - t_k) \end{aligned} \quad (2.8)$$

where  $e$  is the charge of  $\bar{p}$ ,  $m$  is an integer,  $t_k$  is an initial condition,  $T = 1/f_{rev}$ ,  $i_0 = ef_{rev}$ ,  $i_n = 2i_0$ ,  $\omega = 2\pi f_{rev}$ , and  $n$  is the  $n^{th}$  harmonic (or band) of the  $f_{rev}$ . In the spectrum analyser, the spectral density of noise for a given frequency band  $n$ , is obtained from [49]:

$$\frac{dI_n^2}{df} = 2e^2 f_{rev}^2 \frac{dN}{df}. \quad (2.9)$$

The noise power is found by the integration of Eq. (2.9) over frequency ( $f$ ), and is constant for any given frequency band  $n$ :

$$P \propto \int \frac{dI_n^2}{df} df = 2Ne^2 f_{rev}^2. \quad (2.10)$$

Figure 2.7 shows a typical noise band ( $\frac{dI^2}{df}$  vs.  $f$  diagram) or Schottky power spectrum (area under the plot) at the 127<sup>th</sup> harmonic where a total of six Schottky pick-ups in AA are sensitive. The uncertainty in the measured value of the revolution frequency was  $\frac{\delta f_{rev}}{f_{rev}} \sim 10^{-7}$ , which corresponded to  $\delta f_{rev} \simeq 0.1$  Hz [48].

Further details on Schottky noise and Schottky pick-ups are well described in reference [50].

### 2.4.3 Measurement of the Beam Energy Spectrum

The beam energy spectrum was then determined from a measurement of the frequency spectrum through the relationship [51]:

$$\frac{dp_{\bar{p}}}{p_{\bar{p}}} = -\frac{1}{\eta} \cdot \frac{df_{rev}}{f_{rev}} \quad (2.11)$$

with  $\eta$  the “machine slip factor”, which depended on the beam momentum and magnetic field around the machine as follows:



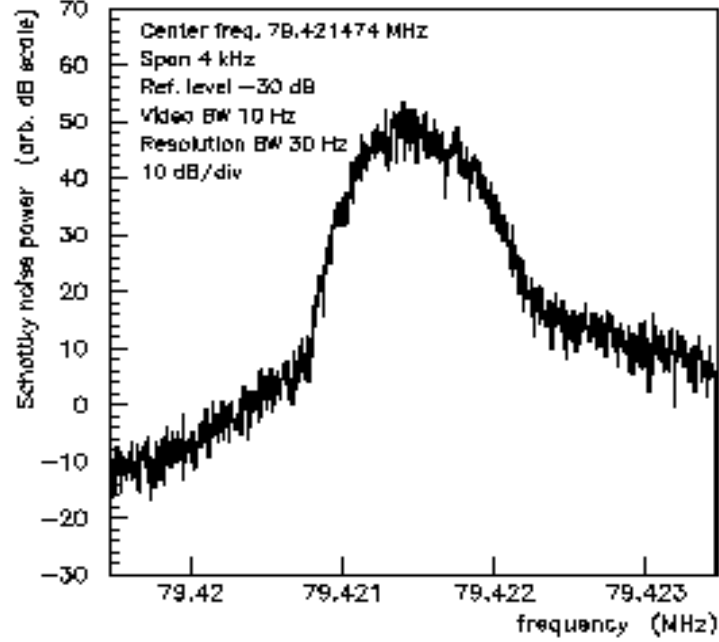


Figure 2.7: Schottky noise power spectrum at the 127th harmonic.

$$\eta \equiv \frac{1}{\gamma_t^2} - \frac{1}{\gamma_{\bar{p}}^2} \quad (2.12)$$

and where  $\gamma_t$  is related to the transition energy ( $E_t$ ) of the accelerator, at which the beam became so unstable that it was largely lost, via  $E_t = \gamma_t m_{\bar{p}} c^2$ . The value of  $\eta$  was  $\sim 10^{-2}$  for the AA in the  $\bar{p}$  momentum range of 4 to 9 GeV/c [51]. Further details on this relationship and measurement can be found in reference [51].

## 2.5 Experimental Technique

The production of a charmonium state in  $\bar{p}p$  annihilation is studied by scanning through the resonance and obtaining the excitation curve. Generally it takes several

steps to scan a charmonium state. Initially, several  $E_{CM}$  points near the resonance are selected and a stack of  $\bar{p}$  beam is decelerated to one of the  $E_{CM}$  points, where data is collected. At each  $E_{CM}$  point, the number of events ( $N$ ) is counted and the efficiency ( $\epsilon$ ) and geometrical acceptance ( $\alpha$ ) are obtained: Then, using the corresponding luminosity ( $\mathcal{L}$ ), the total cross section ( $\sigma_T$ ) at the  $E_{CM}$  point can be obtained using the relationship:

$$\sigma_T = \frac{N}{\epsilon \cdot \alpha \cdot \mathcal{L}} \quad (2.13)$$

These steps continue until all the  $E_{CM}$  points selected are completed. Finally, all the  $\sigma_T$  measurements for each  $E_{CM}$  give an excitation curve such as shown in the Figure 2.8 ( $\chi_0 \rightarrow J/\psi\gamma$ ).

Since resonances like the  $J/\psi$  and  $\psi'$  (with widths of  $\sim 100$  keV and  $\sim 300$  keV, respectively) are narrower than the beam energy spread ( $\Gamma_B \sim 500$  keV), the total cross section is obtained by deconvoluting the Breit-Wigner cross section ( $\sigma_{BW}$ ) with the beam energy distribution ( $G$ ) in the following way:

$$\sigma_{obs} = \epsilon\alpha \int \sigma_{BW}(\sqrt{s'})G(\sqrt{s'} - \sqrt{s})d\sqrt{s'} \quad (2.14)$$

with

$$\sigma_{BW} = \frac{\pi(2J+1)}{(s-4m_p^2)} \frac{\Gamma_R^2 B_{in} B_{out}}{(\sqrt{s} - M_R)^2 + \Gamma_R^2/4} \quad (2.15)$$

and where  $J$ ,  $M_R$  and  $\Gamma_R$  are the total angular momentum, mass and full width of the resonance, respectively.  $B_{in}$  is the branching ratio from  $\bar{p}p$  to the resonance and  $B_{out}$  is the branching ratio from the resonance to a particular decay channel of interest. Thus the measurements of the resonance parameters (mass and full width) for these narrow states depend on the precise measurements of the  $\bar{p}$  beam energy and its distribution rather than on the detector resolution.

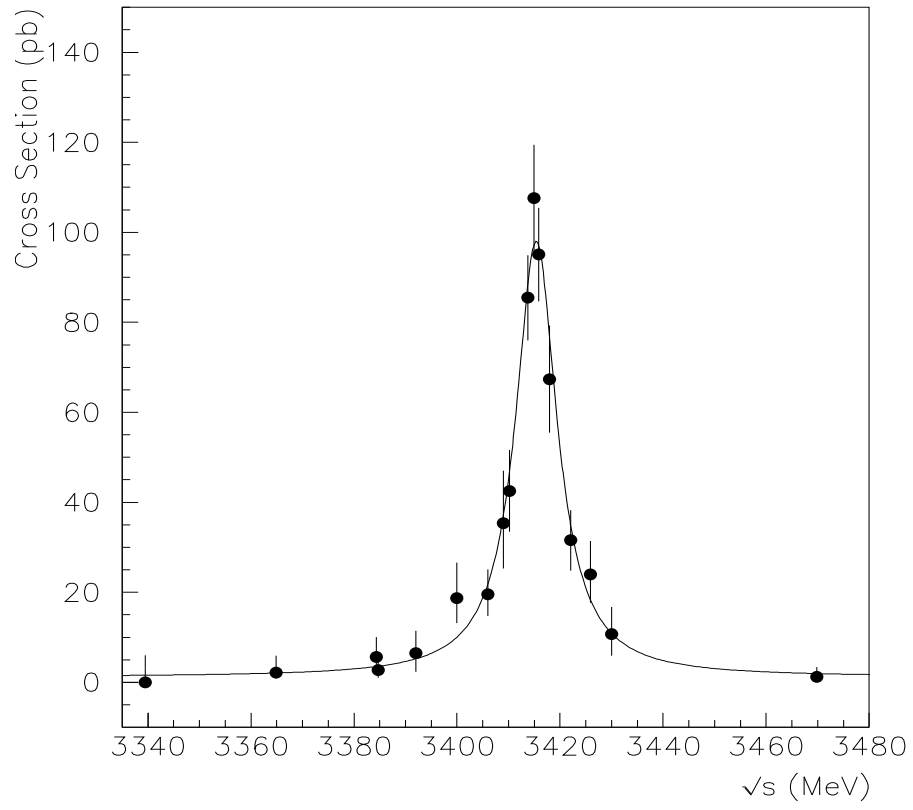


Figure 2.8: Excitation curve of  $\chi_0 \rightarrow J/\psi\gamma$ .

# Chapter 3

## The Detector

The detector was a highly segmented non-magnetic spectrometer, optimized for the detection of electromagnetic (EM) final states, in the presence of the very large hadronic background ( $\sim 50$  mb) from  $\bar{p}p$  annihilation. Figure 3.1 shows a section through the detector as it was configured during the data taking run of 2000.

The detector was composed of three distinct parts with different functions. These were inner tracking detectors, a segmented threshold Čerenkov counter, and electromagnetic calorimeters.

### 3.1 Inner Detectors

The inner tracking detector was used to track the charged particles and as input to the trigger. The tracking detector consisted of three scintillator hodoscopes, two layers of straw drift chambers and two sets of scintillating fibers arranged in concentric cylinders. These inner detectors were housed in a cylinder of 34 cm x 60 cm (diameter x length). The total radiation length of the inner detectors was less than  $0.07X_0$  at  $90^\circ$ . In Figure 3.2 a section through the inner detector is shown.

## E835 EQUIPMENT LAYOUT (Y2K)

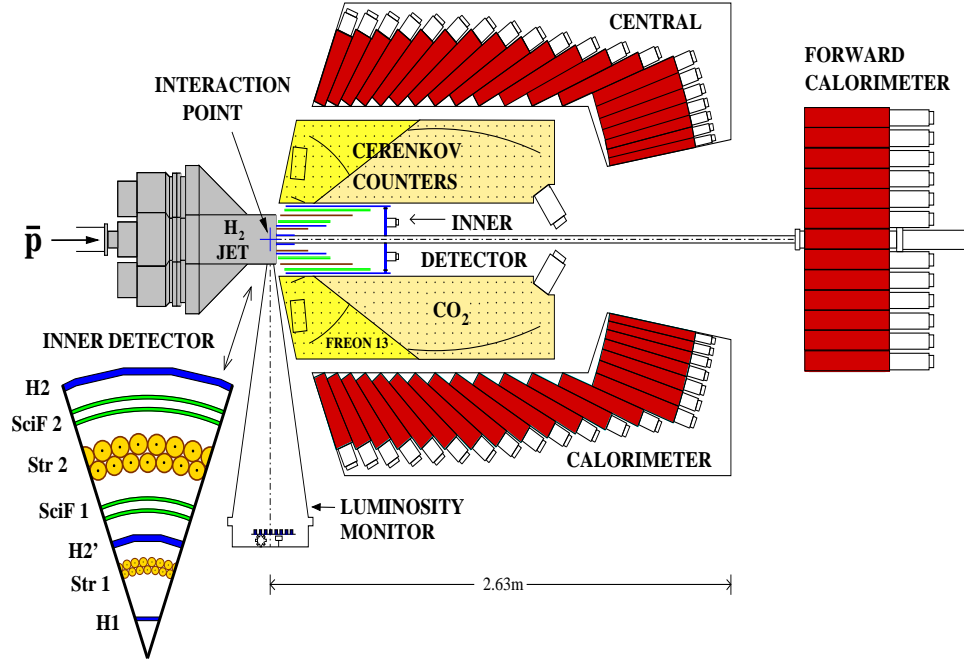


Figure 3.1: Cross section of E835 detector for the 2000 run.

### 3.1.1 Hodoscopes

Hodoscopes<sup>1</sup> are groups of scintillation counters: in this experiment they were made of acrylic plastic of density  $1.03 \text{ g/cm}^3$ , and refractive index 1.58. They fulfilled a dual role, being used to measure  $\frac{dE}{dX}$  as well as providing input signals for the charged particle triggers. There were three sets of concentric hodoscopes: H1, H2' and H2 at radii of 2.2 cm, 7 cm and 16 cm, respectively. All of them had full coverage in the azimuthal angle ( $\phi$ ). H1 consisted of 8 modules forming a cone surrounding the beam pipe. H2' was composed of 24 modules forming a cylinder. The outermost H2 consisted of 32 modules arranged in a cylinder. To minimize particle leakage, the gaps between the modules in H2' were not aligned with those in H1 and H2. Each module of these three sets of hodoscopes was connected to a photo multiplier tube (PMT) via a light guide. The  $\frac{dE}{dX}$  measurement in H2 and H2'

<sup>1</sup>Hodoscope is from the Greek “hodos” and “scopos” meaning path-observer.

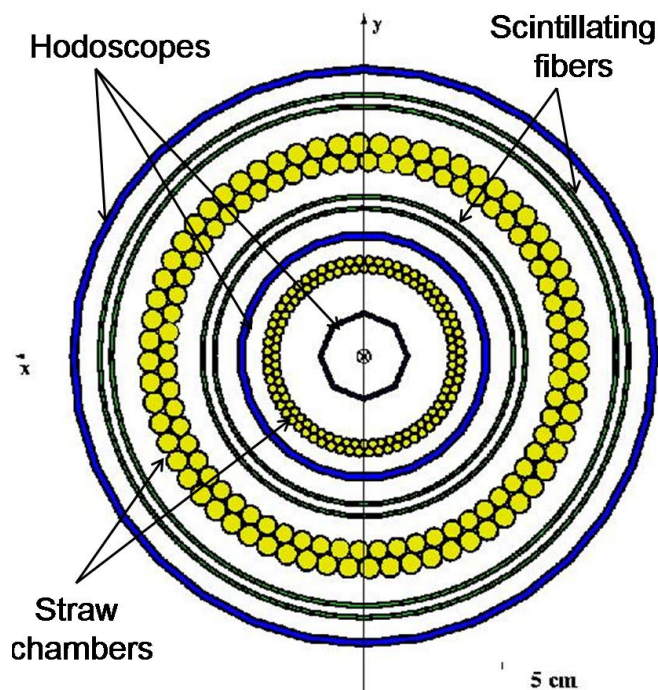


Figure 3.2: Beam's view of the inner detectors.

were performed better than in H1 due to more light yields for a single minimum ionizing particle (m.i.p.). Table 3.1 lists the characteristics of the three sets of hodoscopes.

There was another hodoscope called Forward Charged Hodoscope (FCH), positioned perpendicular to the beam pipe at the endcap of the inner detectors. The FCH was used to veto charged particles in a forward direction ( $2^\circ < \theta_{lab} < 10^\circ$ ) where there was no charged tracking system. It was composed of 8 trapezoidal modules of plastic scintillator with a thickness of 2 mm. Each module had a  $\phi$  coverage of approximately  $50^\circ$  with a  $2.5^\circ$  overlap and were directly connected to a PMT (Philips XP2982).

### 3.1.2 Straw Chambers

The Straw chambers were drift chamber used to measure the azimuthal angle ( $\phi$ ) of the charged particles. They were composed of straw tubes whose walls were made with  $80 \mu\text{m}$  thick aluminiumized mylar. Each straw had a gold-plated tungsten wire

	H1	H2'	H2
Radial distance (cm)	2.2	7	16
Number of modules	8	24	32
Dimension (mm x cm x cm) (thickness x x width x length)	2 mm	4 x 3 x 40.8	4 x 3 x 60
Polar angle coverage	$9^0 < \theta_{lab} < 65^0$	$9^0 < \theta < 65^0$	$12^0 < \theta_{lab} < 65^0$
Light yield ( $\frac{p.e.}{m.i.p.}$ )	10 ~ 20	50 ~ 100	50 ~ 100
PMT type	Philips XP2982	Hamamatsu R1398	Philips XP2982

Table 3.1: Characteristics of scintillating hodoscopes.

(20  $\mu\text{m}$  diameter) at its center, which was kept at positive high voltage. The inner surface of each straw was grounded and served as a cathode. They were filled with a mixture of gases (Ar : C<sub>4</sub>H<sub>10</sub> : (OCH<sub>3</sub>)<sub>2</sub>CH<sub>2</sub> = 82 : 15 : 3); this mixture is efficient at relatively low voltages. The electron drift velocity is about 40  $\mu\text{m}/\text{ns}$  at operating voltage. In Figure 3.3 the mechanical structure of the straw chamber is shown.

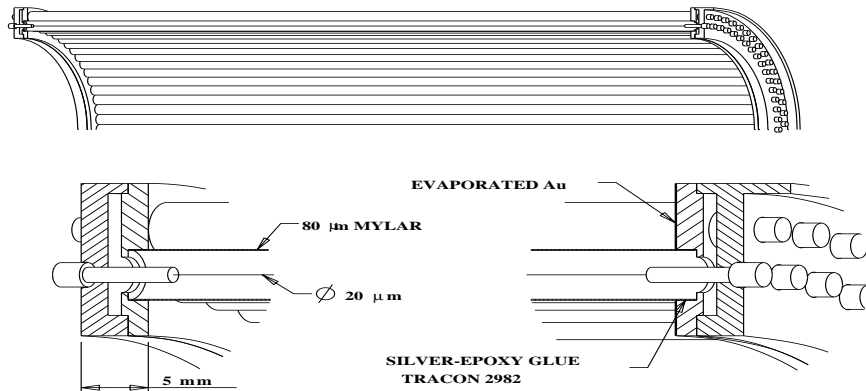


Figure 3.3: Mechanical structure of the straw chamber.

There were two sets of straw chambers (Str1 and Str2), mounted parallel to the beam with a full coverage in azimuth at radial distances of  $r = 5.4$  cm and 12.0 cm, respectively. Each set consisted of 64 straws that formed two staggered layers so that any left-right ambiguity could be resolved. In Table 3.2 the geometrical characteristics of the straw chambers are listed.

	Radial position (cm)	$\theta$ coverage	Straw tube diameter (cm)	Length (cm)
Str1	5.4	$15^\circ < \theta < 58^\circ$	1.00, 1.08	18.20
Str2	12.0	$15^\circ < \theta < 65^\circ$	2.22, 2.42	41.4

Table 3.2: Characteristics of straw chambers.

The efficiency to detect a charged particle varied from 100% (near the wire) to 80% (near the tube surface) and the azimuthal resolution ( $\sigma_\phi$ ) was measured as 9 mrad using a clean sample of the  $J/\psi \rightarrow e^+e^-$  [52].

### 3.1.3 Scintillating Fiber Trackers

A scintillating fiber tracker [53, 54] was used to measure the polar angle ( $\theta$ ) of the charged particles. Two sets of scintillating fibers<sup>2</sup> were wrapped around two hollow concentric cylindrical supports at different radii. These were referred to as the SciF1 and SciF2 detectors. Each set consisted of two staggered layers to minimize cracks: Since they wrapped around the detector they had a full coverage in  $\phi$ . Figure 3.4 shows the side cross section of the scintillating fiber trackers. Table 3.3 lists their characteristics.

The scintillation light from the fibers was detected by Visible Light Photon Counters (VLPCs) [53, 54]. The VLPCs were solid state photo-sensitive devices, kept in a cryostat and maintained at a temperature between 6.5 - 7.2 K. The quantum efficiency of the VLPC is about 70% at 550 nm and the amplification was  $\sim 10^4$ .

---

<sup>2</sup>Kuraray SCSF-3HF-1500.



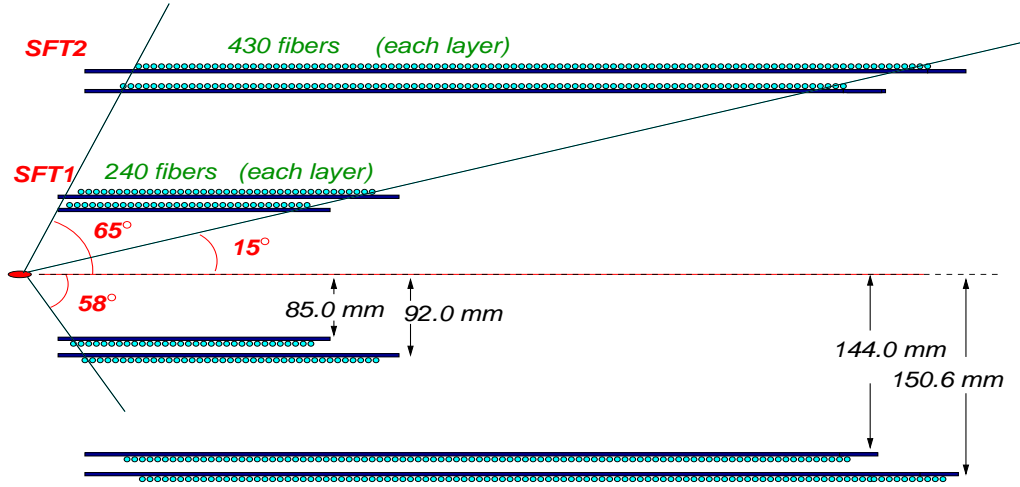


Figure 3.4: Side cross section of the scintillating fibers.

	Radial distance inner, outer (cm)	$\theta_{lab}$ coverage	Fiber diameter (mm)	# of channels
SciF1	8.50, 9.20	$15^\circ < \theta_{lab} < 55^\circ$	0.835 (0.74 active core)	240, 240
SciF2	14.40, 15.06	$15^\circ < \theta_{lab} < 65^\circ$	0.835 (0.74 active core)	430, 430

Table 3.3: Characteristics of the scintillating fibers.

A group of 128 fiber channels were arranged in a VLPC cassette. In all twelve VLPC cassettes were required. Figure 3.5 shows the the schematic of the light path from the scintillating fibers to the VLPC cryostat. The electronic signals from the VLPC's were sent to Analog-to-Digital-Convertors (ADCs) and Time-to-Digital-Converters (TDCs), and also used as input to the first level trigger due to its good intrinsic time resolution and the fast response. A Monte Carlo study showed that the detector efficiency was greater than 98% (for  $\theta_{lab} < 40^\circ$ ) and 90% (for  $\theta_{lab} > 40^\circ$ ) [54]. The average efficiency from both SciF1 and SciF2 was greater than 95%. The detection efficiency was relatively smaller at larger  $\theta_{lab}$  since there was less overlap of the fibers. To estimate the precision of the position of the interaction vertex ( $z$ ),  $\bar{p}p$  elastic scattering was used to compare the  $z$  values from the two adjacent

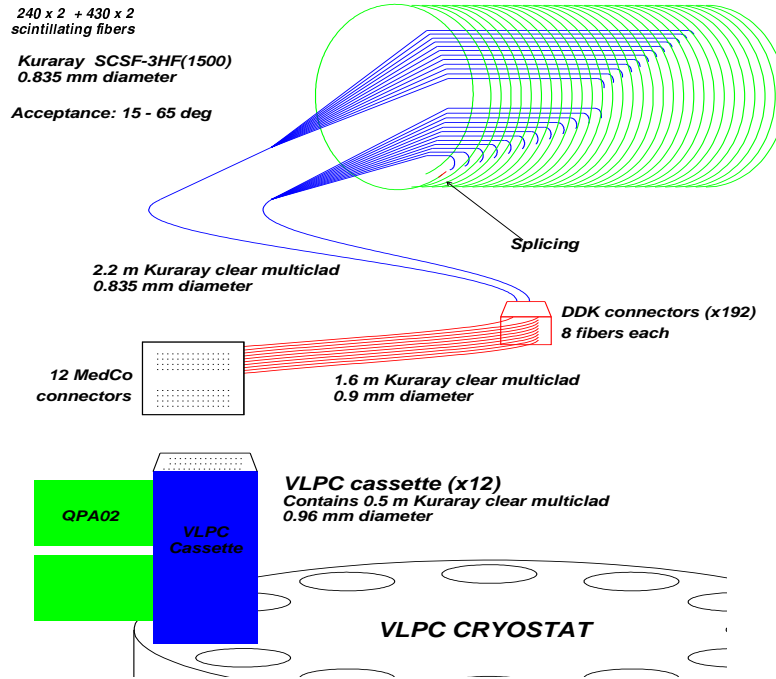


Figure 3.5: Schematic of the light path from the scintillating fibers to the VLPC cryostat.

staggered layers. The vertex resolution were found to be  $\sigma(z_{inner} - z_{outer}) = 0.48$  mm for SciF1 and 0.55 mm for SciF2 and the combined resolution was  $0.22 \pm 0.07$  mm ( $0.5 \pm 0.1$  mm) for  $\theta_{lab} < 40^\circ$  ( $\theta_{lab} > 40^\circ$ ). The analog signals from the fibers were used to measure the  $\frac{dE}{dx}$  of the tracks [54]. By using the  $\frac{dE}{dx}$  measurement and the information on the number of clusters (defined as a set of adjacent hit fibers), the scintillating fibers also provided good discriminating power against a single  $e^+e^-$  track caused by a small opening angle from  $\pi^0$  Dalitz decay and by photon conversion in the beam pipe, as well as against double  $e^+e^-$  tracks from the  $J/\psi$  and  $\psi'$  decays. Further details on the scintillating fiber trackers can be found in references [53, 54].

For the analysis in this thesis the 1996-1997 data were used as well as the 2000 data. In the 1996-1997 run, a silicon detector was located between H2' and Str2.

After this run, the silicon detector was replaced by SciF1 which was operational during data taking in 2000.

## 3.2 Threshold Čerenkov Counter

A set of segmented Čerenkov counters on the outside of all tracking detectors was used to distinguish electron tracks from the hadronic tracks. The signals from these counters were included in the charged particle trigger. Each Čerenkov counter was a gas-filled hollow cylinder with a radius of from 17 cm to 65 cm. The cross section of the Čerenkov counter is shown in Figure 3.6. It was divided in polar angle into two parts, a small angle cell ( $15^\circ < \theta_{lab} < 38^\circ$ ) and a large angle cell ( $34^\circ < \theta_{lab} < 65^\circ$ ). The two cells overlapped in the region of  $34^\circ < \theta_{lab} < 38^\circ$  called septum, and were filled with different gases at room temperature and atmospheric pressure. The small angle cell was filled with  $\text{CO}_2$ , while the large angle cell was filled with either Freon13 or Freon12<sup>3</sup>. Each cell was divided into eight sections in azimuth each equipped with a PMT. To increase the light collection efficiency, the light was focused into the PMTs by converging mirrors. In the small angle cell, each section was equipped with an ellipsoidal mirror to focus the light on to the PMT, while in the large angle cell, each section had a spherical mirror followed by a plane mirror. This extra mirror was required due to the complexity of the geometry (See Fig. 3.6). The gases in the two cells were selected to provide a threshold so that pions with their estimated maximum velocity, the major background of the  $e^+e^-$  events, would not generate Čerenkov radiation. Table 3.4 lists the characteristics of each cell.

Signals from PMTs were amplified by about a factor of ten and then split into two. One signal was sent to the trigger logic and the other was sent to an ADC for charge integration. The photo-electron (p.e.) yields per electron track were higher for smaller  $\theta_{lab}$ . The average number of photo-electrons was  $13 \sim 16$  for  $\theta_{lab} < 34^\circ$  and  $8 \sim 9$  for  $\theta_{lab} > 34^\circ$ . The detector efficiency was determined with  $e^+e^-$  events from  $J/\psi$  decays. The technique was to count the number of events with at least one tagged electron track (1e) and count the number of events with both electrons tagged (2e). The efficiency was then defined as  $\epsilon \equiv \frac{2r}{1+r}$  with  $r \equiv \frac{2e}{1e}$ . In this way,

---

<sup>3</sup>Only Freon13 was used for the 2000 run and last month runs of the 1997.

the efficiency was measured to be  $\epsilon = 98.1 \pm 0.5\%$ . Further details on the Čerenkov detectors and their operation are described in reference [55].

### 3.3 Electromagnetic Calorimeters

The electromagnetic (EM) calorimeters were used for energy, position and timing measurements of the EM final state particles. The calorimeters were made with lead glass blocks. The detector had two sets of EM calorimeters distinguished by their locations: a central calorimeter ( $12^\circ < \theta_{lab} < 70^\circ$ ) (CCAL) and a forward calorimeter ( $2^\circ < \theta_{lab} < 11^\circ$ ) (FCAL). The CCAL was the outermost part of E835 detector and surrounded the inner detectors and the Čerenkov counter, while the FCAL was located in the downstream portion. Each block in these EM calorimeters was attached to a PMT. The following subsections describe the characteristics, calibration and performance of the CCAL and the FCAL.

	Small angle cell	Large angle cell
$\theta$ coverage $\phi$	$15^\circ \sim 38^\circ$ $45^\circ$ (x 8)	$34^\circ \sim 65^\circ$ $45^\circ$ (x 8)
Gas (at STP) n (refractive index) $\theta_c$ $\pi$ threshold (GeV/c)	CO <sub>2</sub> 1.000410 $1.64^\circ$ 4.873	Freon13 or Freon12 1.000720 or 1.001080 $2.17^\circ$ or $2.66^\circ$ 3.677 or 3.003
Focusing mirror (mirror material) Retro-reflec. mirror	Ellipsoidal (plexy, carbon-fiber) N/A	Spherical (glass) plane glass (1 mm thickness)
PMT type PMT diameter Number of PMTs Radiator length (cm) Light collection efficiency	Hamamatsu R1332Q 8/2" 8 93 $\sim$ 72 0.84 $\sim$ 0.90	Hamamatsu R1332Q 8/2" 8 34 $\sim$ 39 0.84 $\sim$ 0.98 or 0.75 $\sim$ 0.88

Table 3.4: Characteristics of the two cells of the threshold gas Čerenkov counter.

### 3.3.1 Central Calorimeter

#### CCAL Characteristics

The central calorimeter consisted of 1280 lead glass modules pointing towards the interaction region. Schott F2 lead glass, was used, which consists of lead (42.2%), oxygen (29.5%) and silicon (21.4%) by weight. It has a density of 3.61 g/cm<sup>3</sup> and a refractive index of 1.651 at 404.7 nm. The radiation length was  $X_0 = 3.141$  cm. The lengths of the CCAL blocks ranged from 12  $X_0$  to 16  $X_0$  with decreasing polar angle. Figure 3.5 shows a side view of the CCAL. The CCAL blocks can be divided into separate rings and wedges representing  $\theta_{lab}$  and  $\phi$ , respectively. There were a total of 20 rings and 64 wedges. Each ring was composed of 64 blocks, where each block had the same  $\theta_{lab}$  but different  $\phi$  (coverage of each block  $\Delta\phi = 5.625^\circ$ ). Each wedge was composed of 20 blocks, where each block had the same  $\phi$  but different

$\theta_{lab}$  ( $\langle \Delta\theta_{lab} \rangle = 2.9^\circ$ ).

The signal in a lead glass block is Čerenkov radiation from electrons in the EM shower. To collect this emanating light from an EM shower, Hamamatsu PMTs were attached to the back face of each CCAL block. The diameter of the PMT varied depending on the block size. The geometrical characteristics of the CCAL blocks and their PMTs are listed in Table 3.5.

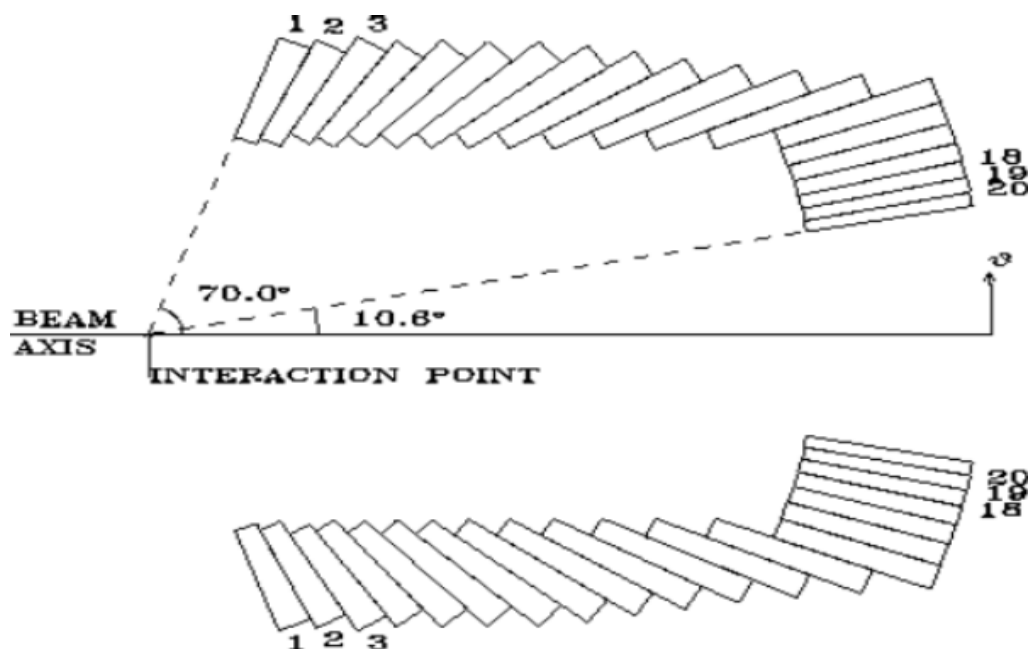


Figure 3.7: Cross section of the CCAL.

Ring #	Block Length (cm)	Central $\theta$ (degree)	Block Width (degree)	Distance from Target (cm)	PMT Diameter (inch)	Fractional PMT Coverage (%)
1	37.80	67.387	5.226	72.44	3.0	47.3
2	38.65	62.259	5.031	75.87	3.0	47.5
3	39.88	57.342	4.803	80.07	3.0	47.6
4	41.50	52.664	4.552	85.08	3.0	47.8
5	43.54	48.246	4.284	90.96	3.0	47.9
6	46.03	44.101	4.007	97.79	3.0	48.1
7	48.98	40.234	3.728	105.62	3.0	48.2
8	50.00	36.644	3.451	114.54	3.0	49.7
9	50.00	33.327	3.183	124.66	3.0	52.0
10	50.00	30.273	2.925	136.07	3.0	54.4
11	50.00	27.472	2.679	148.89	3.0	56.8
12	50.00	24.908	2.449	163.26	3.0	59.3
13	50.00	22.567	2.233	179.34	3.0	61.7
14	50.00	20.434	2.033	197.28	3.0	64.1
15	50.00	18.493	1.848	197.29	2.5	54.6
16	50.00	16.730	1.678	197.29	2.5	66.4
17	50.00	15.130	1.522	197.30	2.0	52.7
18	50.00	13.679	1.380	197.30	2.0	64.4
19	50.00	12.364	1.250	197.30	1.5	44.3
20	50.00	11.174	1.131	197.30	1.5	54.3

Table 3.5: Geometrical characteristics of the CCAL blocks and their PMTs.

### CCAL Calibration

The signal from the PMTs was converted to a digital signal by ADCs. The calibration of the calorimeter was required to provide the relationship between the ADC counts and the corresponding energy. This relationship is quantified as a gain constant ( $G$ ) defined as:

$$G \equiv \frac{Energy}{(\#of ADC)} \quad (3.1)$$

The CCAL calibration in E835 was performed using the copious  $\pi^0\pi^0$  events [56]. To illustrate this method, assume that a total of  $N$   $\pi^0$ s are associated with a block which needs calibration. Then a  $j^{th}$   $\pi^0$  ( $j \in [1, N]$ ) energy is calculated as:

$$M_j = \sum_{i=1}^n G_i A_{ij} \quad (3.2)$$

where  $n$  is the total number of blocks related to the  $j^{th}$   $\pi^0$  and  $A_{ij}$  is the ADC counts from the  $i^{th}$  block of the  $j^{th}$   $\pi^0$ . The determination of  $G$  for each block was done by minimizing the following  $\chi^2$  defined as:

$$\chi^2 \equiv \sum_{j=1}^N \frac{(M_j - E_j)^2}{\sigma_j^2} \quad (3.3)$$

where  $E_j$  is the predicted energy using measured position of the  $j^{th}$   $\pi^0$  and  $\sigma_j$  is the estimated error on  $E_j$ . In this way the gain constant was obtained for every individual block of each stack. For the ring number 20 where statistics of the  $\pi^0\pi^0$  events was low, punch-through particles were used for the calibration [56, 57].

### CCAL Performance

The CCAL resolution was measured by  $e^+e^-$  events from the  $J/\psi$  decay and the measured energy resolution of the CCAL was:

$$\frac{\sigma_E(E)}{E} = \frac{6\%}{\sqrt{E(GeV)}} \oplus 1.4\% \quad (3.4)$$

The average angular resolution of the CCAL was measured as  $\sigma_\theta = 6$  mrad and  $\sigma_\phi = 11$  mrad. The CCAL monitoring was performed during data taking by using laser system. Figure 3.8 shows the schematic of the CCAL laser monitoring system.



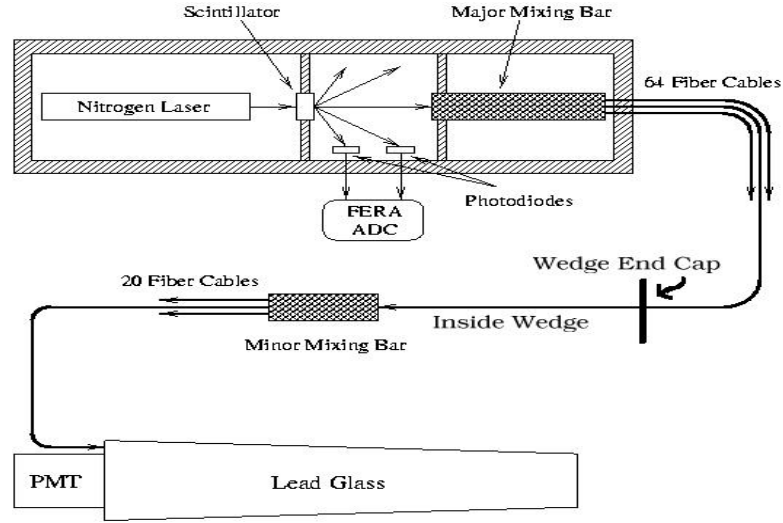


Figure 3.8: Schematic of the laser monitoring system for CCAL.

The Nitrogen monitoring laser (430 nm) was pulsed every 10 seconds and light was injected into all the lead glass blocks. The distribution system consisted of a mixing bar connected to 64 fibers for each wedge; the light was distributed to back face of each block through a second small mixing bar connected to 20 fibers for each ring. The laser light itself was also monitored by two photodiodes positioned just before the main mixing bar.

### 3.3.2 Forward Calorimeter

#### FCAL Characteristics

The Forward calorimeter (FCAL) consisted of a total of 144 SF2 and Schott SF2 lead glass blocks. The FCAL were arrayed perpendicularly to the beam direction surrounding beam pipe and located at the endcap. They were classified as small (48), medium (80) and large blocks (16) in the order of increasing size with the smaller ones were located at smaller polar angle region. Figure 3.9 shows the beam's view of the FCAL. Each block was attached to a RCA PMT. Table 3.6 lists the characteristics of the FCAL blocks and their PMTs. The FCAL was also used to veto particles in the forward region.

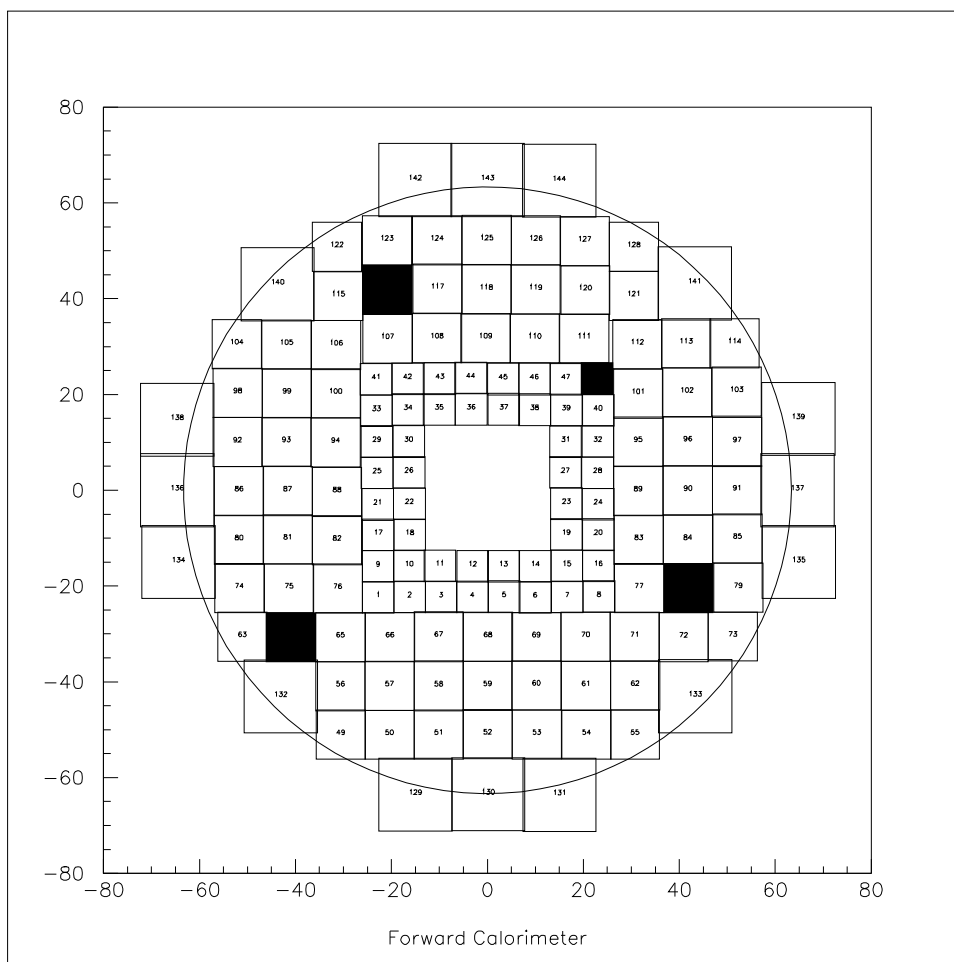


Figure 3.9: Beam's view of FCAL consisted of a total of 144 lead glass blocks (black rectangles represent dead blocks).

	Small block	Medium block	Large block
Glass type	SF2	Schott SF2	SF2
Number of modules	48	80	16
Radiation length ( $X_0$ )	21	14	13
Cross section ( $\text{cm}^2$ )	6.3 x 6.3	10 x 10	15 x 15
Length (cm)	58.6	38	36
PMT (RCA)	6342A	6342A	4335
PMT diameter (inch)	2.5	2.5	5

Table 3.6: Characteristics of the FCAL blocks and their PMTs.

### FCAL Calibration

A preliminary calibration of FCAL was performed by reconstructing  $\pi^0$ s from  $3\pi^0$ ,  $\eta\pi^0$ , and  $\eta\eta\pi^0$  events from data requiring 5 photons in the CCAL and 1 photon from  $\pi^0$  in the FCAL. Figure 3.10 shows the invariant mass distribution for the pair of photons of  $\pi^0$  candidate. The final calibration constant was determined by using data from laser monitoring system, taking advantage of its high statistics. This was done after rescaling the laser data to the 6 photon data [59]. Figure 3.11 shows the calibration constant as a function of the integrated luminosity obtained by the rescaled laser data (white triangles).

### FCAL Performance

The energy resolution of the FCAL was measured to be:

$$\frac{\sigma_E(E)}{E} = \frac{6\%}{\sqrt{E(\text{GeV})}} \oplus 4\% \quad (3.5)$$

The FCAL was monitored during data taking using the same laser system as that was used for the CCAL.

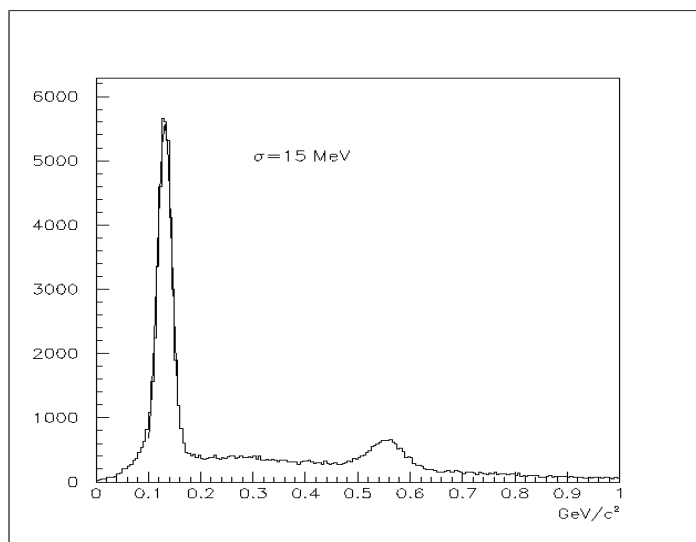


Figure 3.10: Invariant mass distribution of  $\pi^0$  candidates used for preliminary FCAL calibration.

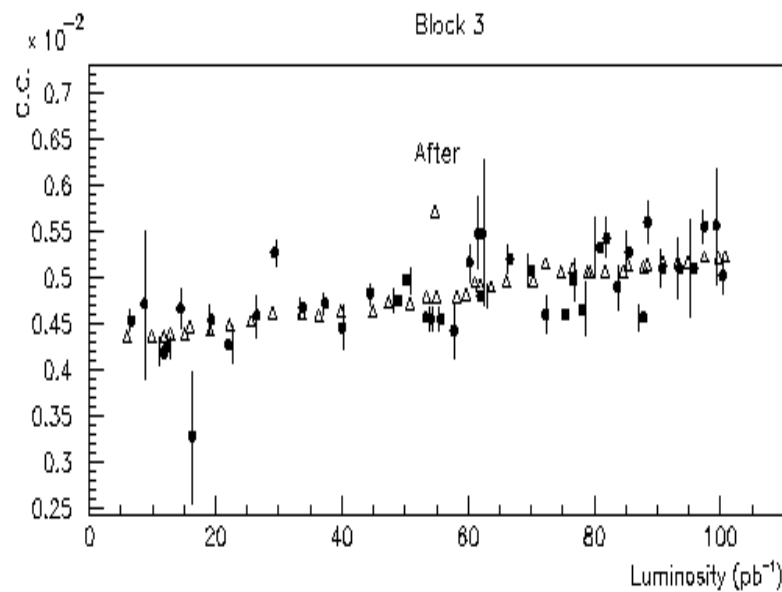


Figure 3.11: FCAL calibration constant (block #3) vs. integrated luminosity obtained from laser data (white triangles) after rescaling to the 6 photon data (black dots).

## Chapter 4

# Trigger System and Data Acquisition

When a  $\bar{p}$  beam (4~9 GeV/c) strikes a hydrogen target, two physical processes happen: elastic scattering ( $\sim 23\%$ ) and inelastic scattering processes ( $\sim 77\%$ ) including  $\bar{p}p$  annihilation into a charmonium state ( $< 0.1\%$ ). However, our interest here is in the  $\bar{p}p$  annihilation into a charmonium state that decay into EM final states. The final states of interest contain  $e^+e^-$ ,  $\gamma\gamma$  or  $\phi\phi$ <sup>1</sup>. The purpose of the E835 trigger system was to select the rare events with those EM final states and  $\phi\phi$  from amongst all types of events.

To achieve this, two types of triggers were introduced: fast (primary) and higher-level (secondary) triggers. The fast trigger, based on signals obtained directly from detectors in order to make a quick decision for event selection, is usually called a hardware trigger. The higher-level, secondary, trigger was performed by a program and thus is referred to as a software trigger.

The fast trigger detectors in E835 consisted of Hodoscopes, Scintillating fibers, Čerenkov counters and CCAL. Signals from these detectors were fed into a trigger logic system, in which the pulses were standardized by discriminators and timing correlations of signals from different detectors were determined by coincidence units. If a possible good event ( $e^+e^-$ ,  $\gamma\gamma$  or  $\phi\phi$  in the final state) occurred, a fast trigger pulse was generated and this enabled all (triggered) detectors to be read out.

---

<sup>1</sup>About 50% of  $\phi$  decays into  $K^+K^-$  which we detect as the final state.

The candidate event selected by the hardware trigger was sent to the higher level (software) trigger where more complicated criteria for event selection were applied.

The main purpose of the Data Acquisition (DAQ) system was to manage the flow of large amounts of digital or analog signals from the detector to a user level (raw data). The DAQ and trigger systems are inseparably related, since DAQ handles data which was selected by triggers, in turn operated by the DAQ system.

The DAQ system included a temporary storage unit called the buffer where data from an event was stored while the next event was being examined by the hardware trigger logic. Thus it was essential to balance trigger rate, event processing rate and buffer capabilities so as not to lose useful events. The  $\bar{p}p$  interaction rate <sup>2</sup> in E835 was  $0.5 \sim 2$  MHz. During the 2000 run, the hardware trigger reduced the  $\bar{p}p$  interaction rate to  $\sim 4$  kHz level which was further reduced to  $\sim 1.2$  kHz by the software trigger. The 1.2 kHz corresponded to the maximum speed of tape writing in E835. During the 1996-1997 run, the  $\bar{p}p$  interaction rate was reduced to  $\sim 2.5$  kHz by the hardware trigger and it was further reduced to  $\sim 500$  Hz by the software trigger.

The following sections will describe the E835 trigger and DAQ systems.

## 4.1 Hardware Trigger

Prior to the trigger, signals from the detectors were split into two parts: One part containing 5% of the original signal was used for trigger purposes and the other part (95%) was used for data read-out once the event was selected by the hardware trigger. The hardware trigger was required to make a quick decision whether to choose an event or not based on the 5% of the signals. To achieve this, the hardware trigger was further classified into Level I and Level II triggers according to the level of trigger logic combinations. Thus the Level I trigger consisted of three parallel triggers.: charged, neutral and  $\phi\phi$  triggers. The role of the charged (neutral) trigger was to find events with charged (EM) final states. The  $\phi\phi$  trigger was used to study  $\eta_c$  ( $^1S_0$ ) and  $^1P_1$  state of charmonium by looking at the resulting  $K^+K^-K^+K^-$  final

---

<sup>2</sup> $\bar{p}p$  interaction rate = total  $\bar{p}p$  annihilation cross section ( $\sim 50$  mb) x instantaneous luminosity ( $1 \sim 4 \text{ cm}^{-2}\text{s}^{-1}$ )

state. Logical elements (logics in short) from charged, neutral and  $\phi\phi$  triggers were sent to the charged, neutral and  $\phi\phi$  Memory Lookup Units (MLU), respectively, where the logics were combined in a certain way and sent to Master MLU (MMLU) where the Level II hardware trigger was performed. With further combination of logics in MMLU, the output was finally sent to a gatemaster unit where the so-called gate signal was generated in order for DAQ to enable detector read-outs. The total transit time for the hardware trigger was less than few  $\mu\text{s}$  so as to meet the  $\bar{p}p$  interaction rate.

Figure 4.1 shows a schematic of the E835 trigger system.

The following subsections describe the charged trigger in detail, as it is relevant to the analysis presented in this thesis, with only brief descriptions of the neutral trigger, MMLU and gatemaster. Details of the  $\phi\phi$  trigger are found in reference [60, 61].

#### 4.1.1 Charged Trigger (Level I trigger)

The charged trigger was dedicated to pick out an event with charged final states which contained  $e^+e^-$ . The input signals for the charged trigger were from all of the hodoscopes (H1, H2' and H2), scintillating fibers (SciF) and the Čerenkov counter. The hardware units necessary for the charged trigger were programmable CAMAC modules and NIM (Nuclear Instrument Module <sup>3</sup>) modules. Figure 4.2 shows the schematic of the charged trigger system. It consisted of three consecutive stages: discrimination, single logic and final trigger stages.

##### Discrimination Stage

In this stage, the input analog signals from each detector were converted into a standard output pulse by a discriminator once the analog signal amplitude was greater than threshold voltage. This discriminated signal was then sent to the single logic stage. The transit time in this stage was about 18 ns except the SciF which was 10 ns.

---

<sup>3</sup>NIM was introduced in 1964 to standardize the system, allowing for module interchangeability.

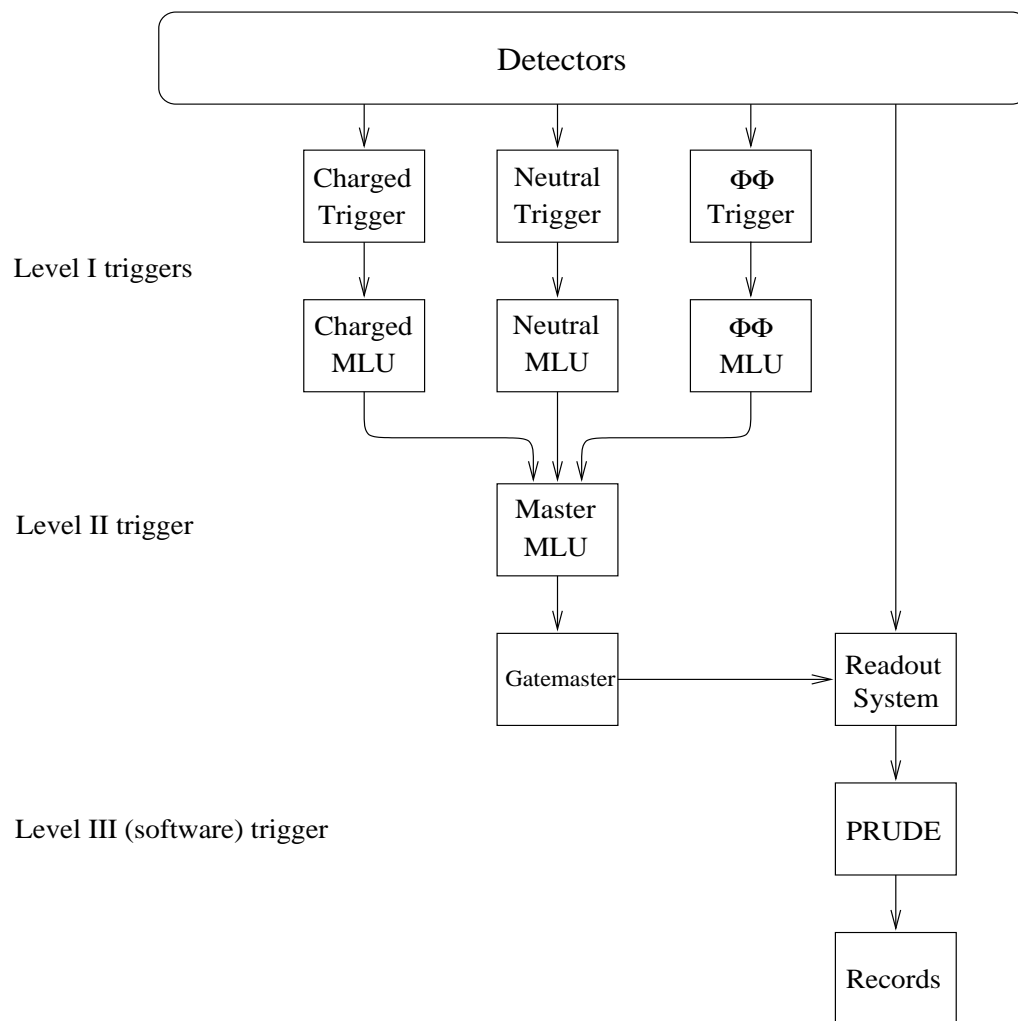


Figure 4.1: Schematic of the E835 trigger system [64].



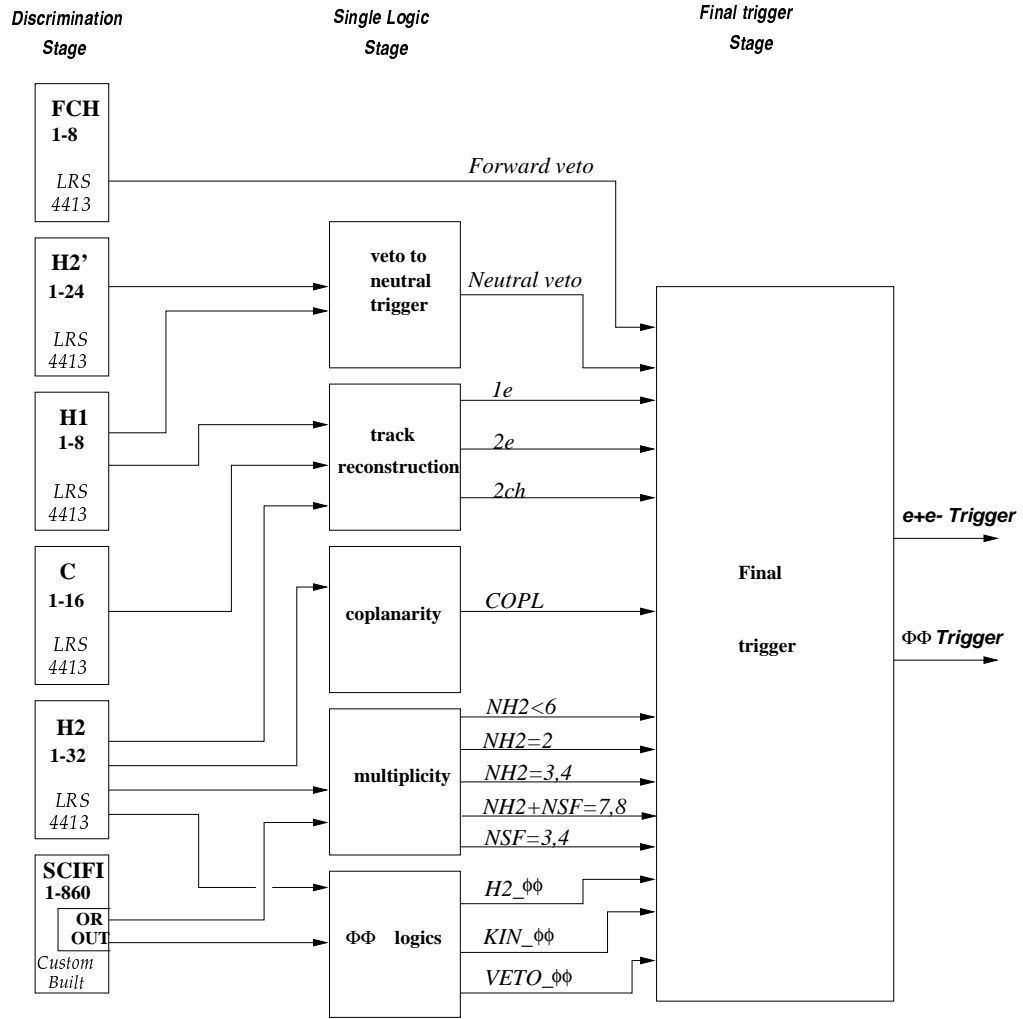


Figure 4.2: Schematic of the E835 charged trigger system.

### Single Logic Stage

In this stage, the signals from the previous discrimination stage were combined to create five single logics which had physical meaning: track reconstruction, coplanarity, multiplicity,  $\phi\phi$  logic and veto to neutral trigger. In the track reconstruction logic (70 ns transit time), the types and number of reconstructed tracks were determined. The requirement for a charged track was a coincidence between one element of H1 and the corresponding elements of H2 in the same octant. Further, an electron track required a corresponding hit in a Čerenkov octant in addition to the charged track requirements. The outputs were classified as **1e**, **2e** and **2ch** which meant 1 electron, 2 electron and 2 charged tracks, respectively. The **coplanarity** logic (50 ns transit time) required two back to back hits in H2 within  $22.5^\circ$ . In the multiplicity logic (65 ns transit time), the number of hits in H2 (**NH2**) and fiber bundles (**NSF**) were determined. The possible multiplicity outputs were: **NH2 = 2**, **NH2  $\leq$  4**, **NH2 = 3, 4**, **NSF = 3, 4** and **(NH2 + NSF) = 7, 8**. The logic of veto to neutral trigger (40 ns transit time) was defined as OR of all eight charged tracks the selection of which was based on the coincidence between H1 and H2' elements. For the tracks with small polar angle, the neutral veto was defined as OR of the FCH (Forward Charged Hodoscope). In this way a total of 14 single logics was formed, which can be summarized as:

- 1) 1e: one electron track defined as the AND of a hadron track (see input 3 below) and the OR of the two corresponding Čerenkov counters (small angle and large angle cells).
- 2) 2e: two electron tracks, i.e., 2 “1e”s.
- 3) 1ch: one charged track defined as the AND between an H1 element and the OR of the six corresponding H2 elements.
- 4) 2ch: two charged tracks, i.e., 2 “1ch”s.
- 5) H2 = 2: exactly two H2 elements hits.
- 6) H2 > 2: more than two H2 elements hits.
- 7) H2 > 4: more than four H2 elements hits.
- 8) H1 > 2: more than two H1 elements hits.
- 9) H1 > 4: more than four H1 elements hits.

10) COPL: coplanarity is defined as the AND between an H2 element and the OR of the three opposite H2 elements.

11) FCH\_OR: the OR of all FCH elements.

12) FCAL\_OR: the OR of all FCAL blocks.

13) H1\_OR: the OR of all H1 elements.

14) H2\_OR: the OR of all H2 elements.

15) Not used.

16) Not used.

### Final Trigger Stage

The output signals from the single logic stages were sent to Memory-Lookup Units (MLUs) in CAMAC. These MLUs logically combined all the input signals. The output signals of MLUs were required to be synchronized in order to compensate timing differences due to the different sources of the signals. To achieve this the timing of the output signal was determined at the leading edge of its strobe signal. The strobe signals were selected according to the types of the MLUs: charged, neutral and  $\phi\phi$  MLU's. Since the timing of a strobe signal was important, the strobe signal was reshaped by a constant fraction discriminator. The MLUs were required to receive their strobe signals within 15 ns of the corresponding input signals [60]. The strobe signal for the Charged MLU (CMLU) was the OR of the H2 hodoscope.

The logical combinations of the input signals of the CMLU produced four outputs: CMLU1, CMLU2, CMLU3 and CMLU4. For example, CMLU1 denoted as  $e^+e^-(1)$  was formed by logical combination of charged tracks and charged veto signal. In detail, the four outputs of the CMLU for the 1996-1997 run were (with  $\otimes \equiv \text{AND}$ ,  $\oplus \equiv \text{OR}$ ):

- 1)  $e^+e^-(1) = (2e) \otimes (\overline{H2 > 4}) \oplus (1e) \otimes (2ch) \otimes (H2=2) \otimes (COPL)$
- 2)  $e^+e^-(2) = (2e) \otimes (H2=2) \otimes (COPL) \otimes (\overline{FCH})$
- 3)  $\phi\phi = (2ch) \otimes (COPL) \otimes (\overline{FCH}) \otimes (\overline{FCAL})$
- 4)  $\bar{p}p = (2ch) \otimes (H2=2) \otimes (COPL) \otimes (\overline{FCH}) \otimes (\overline{FCAL})$ .

For the 2000 run, an additional trigger card was attached to the old ones in parallel to give a backup for potential failure of the old trigger system. Thus the logics with

subscript “NEW” for the 2000 run (below) were the same as for the ones in the 1996-1997 run. The outputs of the CMLU for the 2000 run were:

$$\begin{aligned}
1) \ e^+e^-(1)_{Y2k} &= (2e) \otimes (\overline{H2 > 5}) \oplus (1e) \otimes (2ch) \otimes (H2=2) \otimes (COPL) \oplus \\
&\oplus (2e\_NEW) \otimes (\overline{H2 > 5}) \oplus (1e\_NEW) \otimes (2ch\_NEW) \otimes (H2=2) \otimes (COPL\_NEW) \\
2) \ e^+e^-(2)_{Y2k} &= (2e) \otimes (H2=2) \otimes (COPL) \otimes (FCH) \oplus \\
&\oplus (2e\_NEW) \otimes (H2=2) \otimes (COPL\_NEW) \otimes (\overline{FCH}) \\
3) \ \phi\phi_{Y2k} &= (2ch) \otimes (COPL) \otimes (\overline{FCH}) \oplus \\
&\oplus (2ch\_NEW) \otimes (COPL\_NEW) \otimes (\overline{FCH}) \\
4) \ \bar{p}p_{Y2k} &= (2ch) \otimes (H2=2) \otimes (COPL) \otimes (\overline{FCH}) \oplus \\
&\oplus (2ch\_NEW) \otimes (H2=2) \otimes (COPL\_NEW) \otimes (\overline{FCH}) .
\end{aligned}$$

Table 4.1 lists the inputs and output of the CMLU. The input signals of the Charged MLU (CMLU) were also used for  $e^+e^-$  final state candidates. The outputs of the CMLU were fed into Master MLU (MMLU) where the outputs of neutral MLU (NMLU) [64] and  $\phi\phi$  MLU [61] were also received. The  $\phi\phi$  trigger logics and  $\phi\phi$  MLU are described in reference [61].

### 4.1.2 Neutral Trigger (Level I trigger)

The neutral trigger was dedicated to find EM particles in the final state. Two types of events were considered in the neutral trigger.; One was two body EM final states ( $e^+e^-$  and  $\gamma\gamma$ ) with the highest invariant mass clusters in the CCAL, while the other was multi-photon events coming from light meson decays ( $\pi^0$ ,  $\eta$ , and  $\omega$ ). CCAL was the only detector used to trigger these two types of events. The signals from 1280 CCAL blocks were combined to make a total of 40 super-clusters, each consisting of a super-ring and a super-wedge. A super-ring and a super-wedge were composed of five consecutive rings<sup>4</sup> and nine consecutive wedges, respectively. To avoid trigger inefficiency, each super-ring (super-wedge) was overlapped by one ring (one wedge). Recall that there were a total of 20 rings and 64 wedges in the CCAL.; Thus a total of five super-rings and eight super-wedges was formed and resulted in 40 super-clusters. These 40 signals were discriminated and then sent to the NMLU

---

<sup>4</sup>The super-ring 1 consisted of four rings (1-4).

Input channel #	Physical description	Output channel #	Physical description
1	1e	1	CMLU1 ( $e^+e^-$ (1) / $e^+e^-$ (1) $_{Y2k}$ )
2	2e	2	CMLU2 ( $e^+e^-$ (2) / $e^+e^-$ (1) $_{Y2k}$ )
3	1ch / 1e_NEW	3	CMLU3 ( $\phi\phi$ / $\phi\phi_{Y2k}$ )
4	2ch / Broken	4	CMLU4 ( $\bar{p}p$ / $\bar{p}p_{Y2k}$ )
5	H2 = 2	5	Unused
6	H2 > 2	6	Empty
7	H2 > 4 / H2 > 5	7	Empty
8	H1 > 2 / COPL_NEW	8	Empty
9	H1 > 4 / 2ch_NEW		
10	COPL		
11	FCH		
12	FCAL / 2e_NEW		
13	H1_OR		
14	H2_OR		
15	Empty / 2ch		
16	Empty		

Table 4.1: The inputs and outputs of the Charged MLU (1996-1997 run/2000 run).

as inputs. The NMLU combined these 40 input signals logically and produced four outputs which were PBG1 <sup>5</sup>, PBG3, ETOT-HI and ETOT-LO. The PBG1 and PBG3 were used for the two body electromagnetic events ( $e^+e^-$  and  $\gamma\gamma$ ). The ETOT-HI and ETOT-LO signals, formed by summing energies in CCAL, were used for the multi-photon events. The four outputs of neutral trigger can be summarized as:

- 1) **PBG1**: two back-to-back super-wedge signals satisfying two body kinematics. This was used for  $\gamma\gamma$  and exclusive  $e^+e^-$  trigger.
- 2) **PBG3**: the coincidence between one super-wedge and one of the three opposite super-wedge. This was mainly used for the  $e^+e^- \gamma$  events.
- 3) **ETOT-HI**: CCAL energy greater than 80% of the available energy.

---

<sup>5</sup>PBG means Pb Glass.

- 4) **ETOT-LO**: CCAL energy greater than 70% of the available energy.

For further details on the neutral trigger, see reference [64].

### 4.1.3 Master MLU (Level II trigger)

The purpose of the Master MLU (MMLU), the level II hardware trigger, was to provide a more refined version of earlier triggers by combining output logics from the CMLU, NMLU and  $\phi\phi$  MLU. This level II trigger was enabled when MMLU received its strobe signal from CCAL which triggered on EM final states. There was a total of 15 (14) inputs of the MMLU for the 1996-1997 (2000) run. These inputs consisted of the outputs from the charged, neutral,  $\phi\phi$  triggers and some charged veto signals from the charged trigger. The MMLU produced a total of eight outputs by logically combining the inputs. For example, the  $e^+e^-$  trigger was produced by the logical combination of the  $e^+e^-$  (from the CMLU) and PBG3 (from the NMLU) while the  $\gamma\gamma$  trigger was produced by the logical combination of the PBG1 (from the NMLU) and the charged veto. In detail, for the 1996-1997 run, the eight outputs of the MMLU were:

- 1)  $e^+e^- = e^+e^-(1) \otimes \text{PBG3} \oplus e^+e^-(2)$ .
- 2)  $\bar{p}p \ 90^0 = \phi\phi\text{MLU2} \otimes \text{CMLU4}$ .
- 3)  $\phi\phi = \phi\phi\text{MLU1} \otimes \text{CMLU4}$ .
- 4)  $\gamma\gamma = \text{PBG1} \otimes \overline{(H1 \otimes H2')\_OR} \otimes \overline{FCH\_OR}$ .
- 5) ETOT-HI veto =  $\text{ETOT-HI} \otimes \overline{(H1 \otimes H2')\_OR} \otimes \overline{FCH\_OR}$ .
- 6)  $\bar{p}p \ 55^0 = \phi\phi\text{MLU3} \otimes \text{CMLU3}$ .
- 7) ETOT-HI no veto =  $\text{ETOT-HI} \otimes \overline{H2 > 2}$ .
- 8) ETOT-LO veto =  $\text{ETOT-LO} \otimes \overline{(H1 \otimes H2')\_OR} \otimes \overline{FCH\_OR}$  (ETOT-LO with charged veto both in the central and forward regions).

For the 2000 run, four among eight outputs of the MMLU were different from those for the 1996-1997 run, which were:

- 1)  $e^+e^-_{Y2k} = e^+e^-(1)_{Y2k} \otimes \text{PBG3} \oplus e^+e^-(2)_{Y2k}$ .
- 2)  $\bar{p}p \ 90^0_{Y2k} = \phi\phi\text{MLU2}_{Y2k} \otimes \text{CMLU4}_{Y2k}$ .

- 3)  $\phi\phi_{Y2k} = \phi\phi\text{MLU1}_{Y2k} \otimes \text{CMLU4}_{Y2k}$ .  
 6)  $\bar{p}p$  control =  $\phi\phi\text{MLU3}_{Y2k} \otimes \text{CMLU3}_{Y2k}$ .

These differences were due to the new charged trigger cards added to the old ones in parallel as described in the previous charged trigger section, and due to different  $\phi\phi$  logics [61]. The inputs and outputs of the MMLU are listed in Table 4.2. The transit time from the CMLU/NMLU to the output of the MMLU was about 90 ns.

Input channel #	Physical description	Logical Input combinations	Output channel #	Physical description
1	PBG1	$9 \otimes 2 \oplus 10$	1	$e^+e^-/e^+e^-_{Y2k}$
2	PBG3	$15 \otimes 12$	2	$\bar{p}p \ 90^0/\bar{p}p \ 90^0_{Y2k}$
3	ETOT-HI	$14 \otimes 11$	3	$\phi\phi/\phi\phi_{Y2k}$
4	ETOT-LO	$1 \otimes \bar{5} \otimes \bar{8}$	4	$\gamma\gamma$
5	(H1 $\otimes$ H2')_OR	$3 \otimes \bar{5} \otimes \bar{8}$	5	ETOT-HI veto
6	FCAL_OR/Unused	$16 \otimes 12$	6	$\bar{p}p \ 55^0/\bar{p}p$ control
7	H2 > 2	$3 \otimes \bar{7}$	7	ETOT-HI no veto
8	FCH_OR	$4 \otimes \bar{5} \otimes \bar{8}$	8	ETOT-LO veto
9	CMLU1			
10	CMLU2			
11	CMLU3			
12	CMLU4			
13	Unused			
14	$\phi\phi\text{MLU1}$			
15	$\phi\phi\text{MLU2}$			
16	$\phi\phi\text{MLU3}$			

Table 4.2: The inputs and outputs of the Master MLU (1996-1997 run/2000 run). See the text for the explanation of the logical input combinations.

#### 4.1.4 Gatemaster

The main purpose of Gatemaster was to generate a gate signal which enabled the DAQ read-out system to collect data from the CAMAC modules and to transfer the

data to software trigger. It also reset the electronics for different types of triggers. The Gatemaster was triggered by a signal from CCAL which triggered on EM final states. The gate signal was formed by OR of all input signals of Gatemaster. The Gatemaster had a total of 12 (11) active input channels for the 1996-1997 (2000) run excluding two empty channels (#11 and #16). Eight of them were from the MMLU. The other six inputs (Laser Monitor, Silicon Strobe, Minimum Bias, Random Gate, FCAL Cosmic Ray and High Rate Minimum Bias) were from special triggers for monitoring, checking efficiency and debugging. For completeness, we summarize them here. The Silicon Strobe and FCAL Cosmic Ray triggers were not used in either of the 1996-1997 and 2000 runs. The Laser Monitor was used for checking the stability of the CCAL/FCAL gains by using a 0.1 Hz pulsed laser. The Minimum Bias trigger [64] was used for checking trigger efficiency. The Random Gate trigger was used to check the rate dependence of the analysis cuts due to pileup in the detector.; The Random Gate events were collected from a 10 kHz laser pulser during data taking. Finally, the High Rate Minimum Bias trigger was used for general debugging during the 1996-1997 run only.

The input channels of the Gatemaster and their meanings are listed in Table 4.3.

Input channel #	Physical description	Input channel #	Physical description
1	$e^+e^- / e^+e^-_{Y2k}$	9	Laser Monitor
2	$\bar{p}p \ 90^\circ / \bar{p}p \ 90^\circ_{Y2k}$	10	Silicon Strobe (unused)
3	$\phi\phi / \phi\phi_{Y2k}$	11	Empty
4	$\gamma\gamma$	12	Minimum Bias
5	ETOT-HI veto	13	Random Gate
6	$\bar{p}p \ 55^\circ / \bar{p}p \text{ control}$	14	FCAL Cosmic Ray (Unused)
7	ETOT-HI no veto	15	High Rate Min. Bias / Unused
8	ETOT-LO veto	16	Empty

Table 4.3: The inputs of the Gatemaster (1996-1997 run/2000 run).



## 4.2 Software Trigger (Level III trigger)

The purpose of the software (Level III) trigger was to further reduce the hardware trigger rate by performing crude online event reconstruction by means of a program called "PRUDE" (Program Rejecting Unwanted Data Events). Events selected by the software trigger were classified as GK, GP or GN according to types, and then stored to the corresponding tapes.

The GK tapes were prepared for charged ( $e^+e^-$ ) analysis while the GN tapes were for neutral analysis. The  $\bar{p}p$  elastic scattering and  $\phi\phi$  events were contained in the GP tapes. Table 4.4 lists the PRUDE filter IDs, their physical meanings and their output destinations in order of decreasing priorities. Some inputs (priority numbers 1 to 12) of the PRUDE were from the Gatemaster, which were automatically passed to the tapes without filtration for the purposes of triggering, monitoring, efficiency checking and debugging. The PRUDE also produced relatively refined data files where priority number was greater than 14, and this was to provide quick on-line and off-line analyses. The requirements of the  $e^+e^-$  gold file ("goldee", priority #13) were GM1 ( $e^+e^-$ ) and invariant mass greater than 2.2 (2.0) GeV for the  $\psi'$  ( $J/\psi$ ) candidate. The conditions for "goodee" (priority #14) were GM1 ( $e^+e^-$ ) and invariant mass greater than 2.0 GeV but less than 2.2 GeV. The "elec" (priority #15) contained all events from GM1 which failed both "goldee" and "goodee" conditions. The physical descriptions about  $\phi\phi$  events or neutral events (priority # > 15) are explained in reference [64].

## 4.3 Data Acquisition (DAQ)

The data acquisition (DAQ) system played a dual role: One was to monitor detectors while data taking (online), while the other was to manage data flow and to save some of the data for later (offline) analysis. DAQ system consisted of four independent parallel components: These were luminosity, scaler, beam parameter and event DAQ's. The luminosity and scalar DAQ worked through the CAMAC (Computer Automated Measurement And Control <sup>6</sup>) system. The luminosity data

---

<sup>6</sup>CAMAC is an international standard of a modular data handling electronic system established

PRUDE filter ID #	Physical description	Priority	Output stream
90	Laser Monitor (GM9)	1	GK
120	Minimum Bias (GM12)	2	GK
130	Random Gate (GM13)	3	GK
70	ETOT-HI no veto (GM7)	4	GK
80	ETOT-LO veto (GM8)	5	GK
150	High Rate Min. Bias/Unused (GM15)	6	GP
10	$e^+e^- / e^+e^-_{Y2k}$ (GM1)	7	GK
40	$\gamma\gamma$ (GM4)	8	GK
30	$\phi\phi / \phi\phi_{Y2k}$ (GM3)	9	GP
20	$\bar{p}p$ $90^\circ / \bar{p}p$ $90^\circ_{Y2k}$ (GM2)	10	GP
60	$\bar{p}p$ $55^\circ / \bar{p}p$ control (GM6)	11	GP
50	ETOT-HI veto (GM5)	12	GK
13	goldee	13	GK Gold
12	goodee	14	GK
11	elec	15	GK
31	$\phi\phi$	16	GP
48	goldgg	17	GK GNA gold
47	goodgg	18	GK GNA
42	etainv	19	GK GNA
43	piinv	20	GK GNA
44	cmainv	21	GK GNA
45	cmbinv	22	GK GNA
41	invmass	23	GK GNA
52	etaetot	24	GN GNA
53	pietot	25	GN GNA
54	cmaetot	26	GN GNA
55	cmbetot	27	GN GNA
51	etotsoft	28	GN
170	neutr	29	GN

Table 4.4: PRUDE filters, physical meaning, priority, and final data tapes.

was used to check the status of the Luminosity Monitor and to determine the interaction rate; The scalar data was used for monitoring the rate of selected counters and trigger logics. The beam parameter DAQ was operated by Fermilab Beams Division and was provided via Accelerator Network (ACTNET). The beam parameter data provided information on the status of the beam such as beam momentum, position, spread and emittance. The function of event DAQ system was to collect signals from detectors, to digitize them, to process the event, to perform a preliminary on-line analysis, and, finally, to store the raw data into storage devices. The event DAQ was based on the Data Acquisition for Real Time system (DART<sup>7</sup>) that was developed at FNAL [62].

The following subsection describes the data flow and the DAQ hardware.

### 4.3.1 Data Flow and DAQ Hardware

To monitor detectors and to manage the data flow from detectors to raw data, a number of hardware components were required: Computers, readout electronics, CAMAC crates, VME (Versa Module Europa<sup>8</sup>) crates and tape drives. The schematic of the E835 DAQ hardware system is shown in Figure 4.3.

The computers were used to coordinate, process, filter, log and monitor the data streams: made by three Silicon Graphics Inc. (SGI), there were three in total, named Indy, Challenge-L and Indigo, communicating with each other via ethernet. SGI Indy was the run control computer that coordinated the four independent data streams coming from their own DAQ sources. For debugging and programming purposes, SGI Indy communicated, via two SCSI 411 Jorway Interfaces, with the CAMAC branches where data read-out was performed. SGI Challenge-L was equipped with twelve 150 MHz CPUs<sup>9</sup> and was used for the event DAQ where the Data Flow Manager (DFM) managed the event building, filtering and logging. SGI Indigo was used for monitoring of the detectors and for the online-event-display.

---

in 1969 by the European Standards on Nuclear Electronics (ESONE) Committee [67]

<sup>7</sup>DART is a DAQ collaboration consisted of the Online Support Department under Fermilab Computing Division and 6 fixed target experiments in Fermilab: E781, E811, E815, E831, KTeV, and E835.

<sup>8</sup>VME is a flexible open-ended bus system consisting of 4 sub-buses following Eurocard standard.

<sup>9</sup>Four 150 MHz CPUs for the 1996-1997 run.

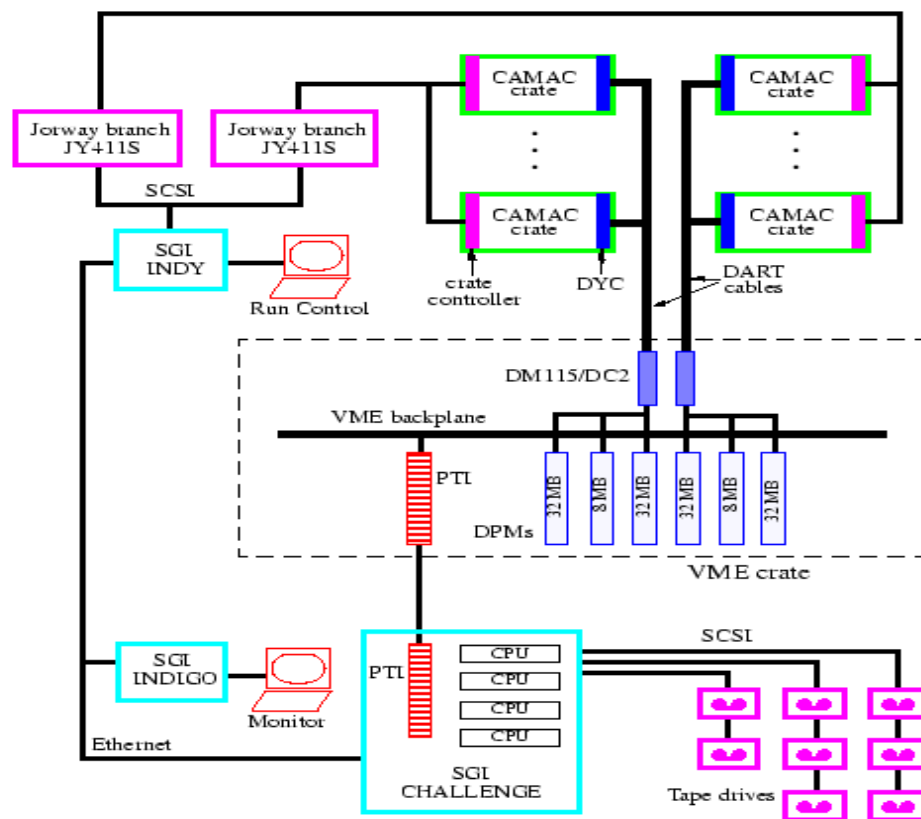


Figure 4.3: Schematic of E835 DAQ hardware system.

Data read-out started when a signal from the hardware trigger triggered all detectors to select the event of our interest. The read-out electronics were composed of 195 FERA ADCs (LeCroy 4300, 4300b) and 114 TDCs (LeCroy 3377) <sup>10</sup>. All the read-outs were housed in a total of 17 CAMAC crates <sup>11</sup> organized in 3 CAMAC branches. Each CAMAC crate had an intermediate data buffer called DYC (Damn Yankee Controller) developed by the DART, which was located in the left of all other modules. The ECL-ports in the front-end of each CAMAC transferred the data from the read-outs to the DYC modules. The DYC stored the 16-bit input data but sent them (as 32-bit data through DART cables) to two pairs of Access Dynamics DC2/DM115 modules in the VME crate under the FIFO (First-In First-out) principle. When the DYC received the data, it generated a busy signal and sent it to the trigger logic to prevent acceptance of the next event: This was done with an efficiency greater than 95%. Each DC2 was connected to two 32MB DPMs (Dual Ported Memory) and one 8MB DPM via VSBUS of the VME crate and sent the data to the two 32MB DPMs under the so-called “pingpong” algorithm: A “gateway” process running on Challenge-L read data from the ping/pong DPM while the DC2 wrote to the pong/ping DPM. The “gateway” and the DC2 communicated each other through the 8MB DPM, and this was to check their status for swapping DPMs (ping  $\leftrightarrow$  pong). The events read by the “gateway” were written to two buffers in the Challenge-L, where all CPUs shared their memories. As soon as one buffer was filled, the “gateway” released the data to an online filter (software trigger) running on each CPU of the Challenge-L before writing to the other buffer. Then the software trigger started processing the event by performing some simple online event reconstruction. Events selected by the software trigger were recorded to 8-mm tapes (5.0 GByte capacity). A total of five tape drives ran in parallel to record the data to the tapes. Two of them were for neutral events, two of them were charged events, and the last one was for efficiency study events. There was another set of five tape drives which were intended to take over the recording as soon as the other set of five tape drives finished the recording and waited for re-loading of new tapes. This swapping defined the ending of one run and the beginning of a new run. A typical

---

<sup>10</sup>166 FERA ADCs (LeCroy 4300, 4300b), 66 TDCs (LeCroy 3377), and 23 PCOS for the 1996-1997 run.

<sup>11</sup>14 CAMAC crates for the 1996-1997 run.

event size was about 1.2 KBytes and each tape drive had maximum recording rate of 1 MBytes/s (about 833 events/s). During data taking, the performance of tape drives was 350 KBytes/s (292 evnets/s) for the neutral data, 300 KBytes/s (250 evnets/s) for the charged data and 250 KBytes/s (208 evnets/s) for the efficiency study data.

# Chapter 5

## Data Analysis

The purpose of this analysis is to measure the angular distribution parameter  $\lambda$  of the process  $\bar{p}p \rightarrow e^+e^-$  at the  $\psi'$  resonance. In this chapter, the details of the analysis are described: They include a description of the data sets used in the analysis, the clustering algorithms applied to the data and the criteria for  $e^+e^-$  event selection as well as background and efficiency studies. A GEANT Monte Carlo [65] was used in this data analysis for several purposes: to optimize the analysis cuts for event selection, to calculate background levels and to investigate the detector response.

### 5.1 Data Set

Two sets of the  $\psi'$  data from two different data taking periods were collected. A total of  $10.09 \text{ pb}^{-1}$  luminosity in seven stacks was obtained in an energy scan at the  $\psi'$  ( $3685 < E_{cm} < 3687 \text{ MeV}$ ) during the 1996-1997 run. In the 2000 data taking run, we collected  $12.48 \text{ pb}^{-1}$  of luminosity ( $3684.5 < E_{cm} < 3687.5 \text{ MeV}$ ) in nine stacks. Table 5.1 lists each stack number with the corresponding luminosity and energy of the data.

For the analysis presented in this thesis, the data used came from Mini Data Summary Tape stream (MDST) which contained all the inclusive  $e^+e^-$  candidate events which were filtered from GK Gold tapes containing the gold  $e^+e^-$  events (See Table 4.4 in Chapter 4). The requirements for an event to be selected for the

MDST were:

- 1) It had to have an invariant mass pair ( $m_{e^+e^-}$ ) greater than 2.6 GeV.
- 2) Each electron candidate should have a corresponding Čerenkov hit.
- 3) Each electron candidate should have at least two out of three hodoscopes hits.

## 5.2 Clustering

An electromagnetic shower caused by a particle ( $e^+$ ,  $e^-$  and  $\gamma$ ) can spread over several calorimeter blocks since the E835 calorimeters were highly segmented. To quantify this, the concept of cluster was introduced, representing an electromagnetic shower spread over 3 x 3 blocks. Usually a shower was well represented by a single cluster, but sometimes it was detected as two separate clusters. This effect was referred to as "shower splash" when its origin could not be attributed to bremsstrahlung. The following subsections describe how a cluster is reconstructed by the CCAL clusterizer, what a "shower splash" event is, and how the timing of a cluster was determined.

### 5.2.1 CCAL Clusterizer Algorithm

The function of the CCAL clusterizer was to accurately reconstruct the energy and position of an electromagnetic interaction which appears in the calorimeter of deposited energy. To find a cluster, the clusterizer started searching for a seed, the highest energy block in a group with energy above a certain predetermined threshold (the seed threshold). Once a seed was found, all the nearest-neighbor blocks surrounding it and the seed itself were considered as a cluster candidate consisting of a 3 x 3 group. The process of searching for cluster candidates continued until no seed remained in the CCAL. Next the energies in the 3 x 3 blocks were summed up. When the summed energy was greater than another predetermined threshold (the cluster threshold), the group of blocks was identified as a cluster. In the algorithm, a seed was prevented from belonging to any of the 3 x 3 blocks surrounding other seeds. However, the possibility of overlap between two neighboring clusters, caused by two nearby hits needed to be taken into account. Two kinds of overlap were



1996-1997 Data			2000 Data		
Stack #	Luminosity ( $nb^{-1}$ )	$E_{cm}$ (MeV)	Stack #	Luminosity ( $nb^{-1}$ )	$E_{cm}$ (MeV)
2	1086.22	3685.58 $\sim 3686.02$	1	747.722	3685.2 $\sim 3687.6$
6	1435.58	3686.15	2	1008.169	3686.0
7	1085.27	3685.9	14	991.877	3686.0
8	1127.08	3686.2	29	991.911	3684.5 $\sim 3686.5$
17	1306.72	3686.16	30	396.250	3686.0 $\sim 3687.5$
39	796.10	3686.40 $\sim 3686.95$	49	2566.442	3686.0
40	1458.83	3686.00 $\sim 3686.02$	50	1275.000	3686.0
67	240.06	3685.0 $\sim 3687.0$	51	2103.259	3686.0
			54	2400.949	3686.0
Total	10121.01 ( $nb^{-1}$ )		Total	12481.58 ( $nb^{-1}$ )	

Table 5.1: Stack-by-stack luminosity and the corresponding energy from the 1996-1997 run (left) and the 2000 run (right).

considered: “shared” and “split”, these occurred when either of the two overlapping clusters had two distinct shower maxima, “shared”, or when the two clusters were so close to each other that the two maxima were indistinguishable. This type of cluster was classified as a “split” cluster, which could happen when a  $\pi^0$  decayed symmetrically into two photons too close to be distinguishable from each other. These clusters were referred to as a coalesced  $\pi^0$ <sup>1</sup>. When a cluster did not overlap at all with the nearest cluster, it was called as a “isolated” cluster. These three types of clusters are illustrated in Figure 5.1. A further distinction between an “isolated” and “split” clusters was made on the basis of the cluster masses ( $M_{cl}$ ), which was defined as:

$$M_{cl} \equiv \sqrt{\left(\sum_i E_i\right)^2 - \left(\sum_i \vec{p}_i\right)^2} \quad (5.1)$$

where  $i$  represents each block in a cluster consisting of 5 x 5 blocks<sup>2</sup>. Since most “split” clusters were coalesced  $\pi^0$ ’s, the distribution of  $M_{cl}$  for a “split” clusters was peaked at the  $\pi^0$  mass and  $M_{cl}$  for “isolated” clusters was lower. Figure 5.2 shows the cluster mass distribution. The lower peak (near 60 MeV) is from “isolated” clusters and the upper peak is from “split” clusters. Thus in the analysis, if a cluster mass was greater than a certain value, say 100 MeV, then this cluster was considered to be a “split” cluster and identified as a  $\pi^0$ .

Once a cluster was identified as being either a “shared” or a “split” cluster, a sharing algorithm was applied to estimate the new energies and positions of the two split clusters. The algorithm also performed energy and position corrections to compensate for cracks in the CCAL [72].

The cluster splitting algorithm for “split” clusters was developed for use in the  $\pi^0\pi^0$  and  $\gamma\gamma$  analyses. However it was found that for the higher energy showers from  $\psi'$  events it introduced a systematic bias. Consequently this part of the clusterizing algorithm was switched off for this analysis.

---

<sup>1</sup>The smallest possible opening angle due to a symmetric decay of a  $\pi^0$  corresponded to about 1.5 calorimeter blocks.

<sup>2</sup>Only for the purpose of cluster mass calculation, 5 x 5 blocks were considered rather than the usual 3 x 3 since coalesced  $\pi^0$  has a more widely spread shower.

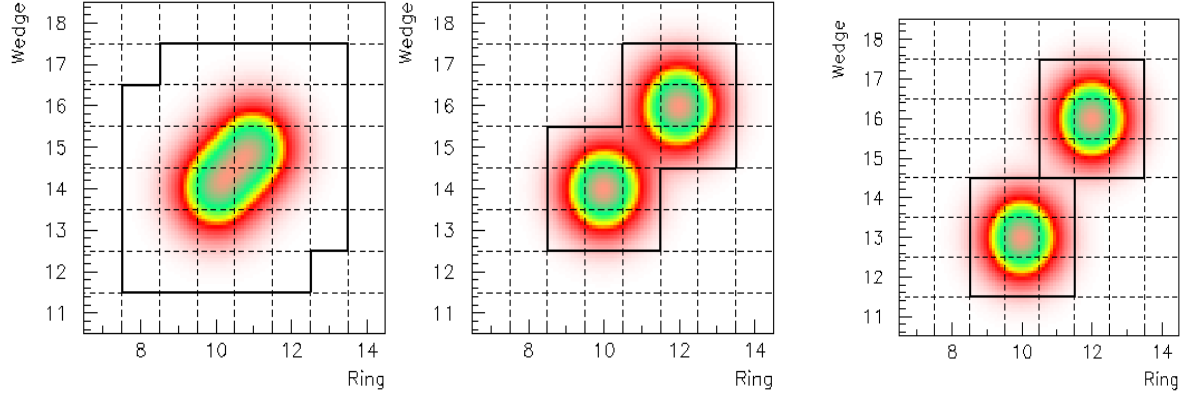


Figure 5.1: Three types of clusters: “split” (left), “shared” (middle), and “isolated” (right).

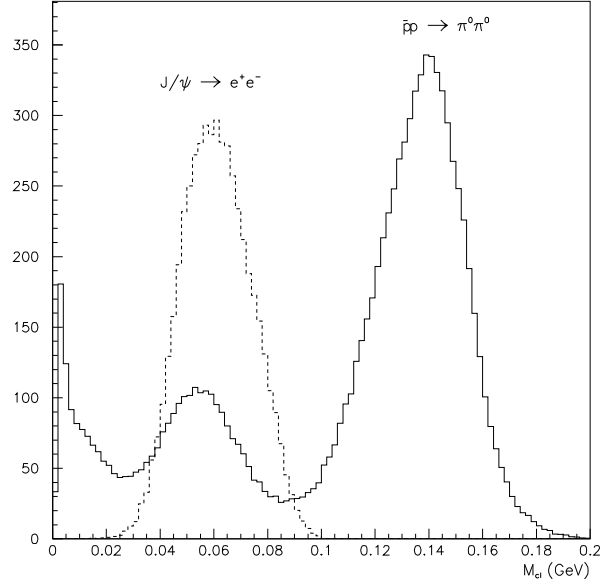


Figure 5.2: Cluster mass distribution for “isolated” clusters (peak near 60 MeV) and “split” clusters (peak near 135 MeV).

### 5.2.2 “Shower splash”

An electromagnetic shower develops through both bremsstrahlung and  $e^+e^-$  pair production. The transverse profile or lateral spread of the shower can be described by the Molière radius ( $R_M$ ), defined as [67]:

$$R_M = X_0 \frac{E_s}{E_c}. \quad (5.2)$$

Where  $X_0$  is the radiation length of the absorbing material (3.141 cm for the CCAL),  $E_s \equiv m_e c^2 \sqrt{4\pi/\alpha} \cong 21.2$  MeV and  $E_c$  is the critical energy<sup>3</sup> where the radiation energy loss and the collision energy loss are the same. On average more than 90% of an electromagnetic shower is contained within a radius equal to  $R_M$  [67]. For both the CCAL and FCAL, the  $R_M$  was 2.43 cm. So normally a shower would be contained within 3 x 3 block array and if a shower was larger than this it would be split into two distinct clusters (one main cluster and one or more secondary clusters). In certain cases a shower can spread either through a significant fluctuations or due to non-uniformities of the CCAL. This type of lateral spread of a shower resulting in two clusters, was called as a “shower splash”. Clearly a “shower splash” is not correlated to bremsstrahlung generated in either the inner detectors or the beam pipe.

In Figure 5.3, a typical  $e^+e^-$  event is displayed, generated using GEANT 3.21. The top plot shows a shower profile of the event and the bottom one shows the corresponding hits in the CCAL. In this event there is no significant bremsstrahlung at the inner detectors or the beam pipe and it would be expected that this type of event would reconstruct as a 2-cluster event. However, the clusterizer interprets it as a 3-cluster event. In Figure 5.4, the hitmap (energy deposition in the CCAL represented as rectangular boxes) of the same event is shown as a function of  $\theta$  and  $\phi$ . The size of the boxes increases as the energy deposition increases. In the same figure, the corresponding clusters are represented as triangles: Two down-pointing triangles are for two main clusters while the other shows the location of the secondary cluster.

---

<sup>3</sup>The critical energy of our calorimeter was about 27.40 MeV.

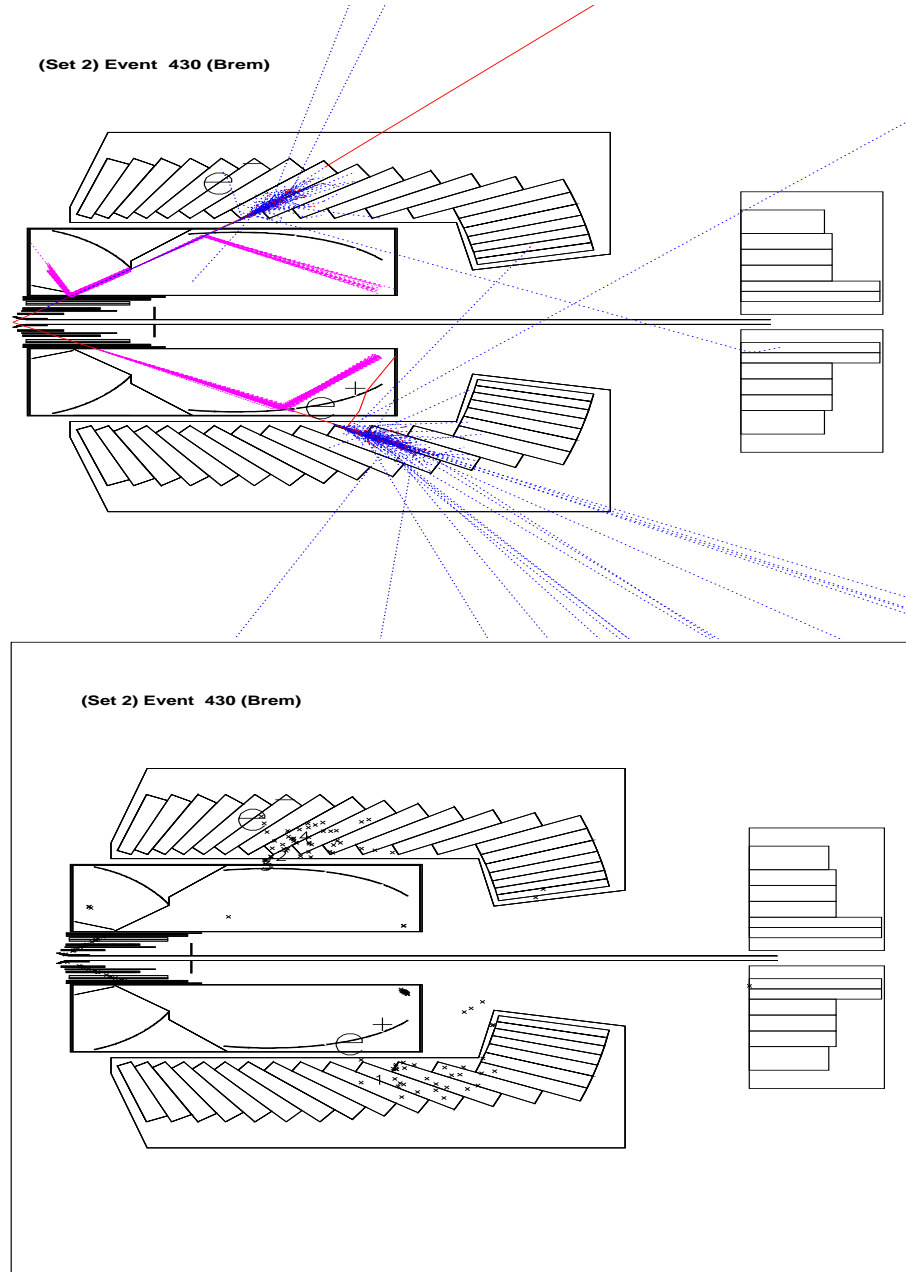


Figure 5.3: An  $e^+e^-$  event display (top) and the corresponding hits in the CCAL (bottom) obtained by the 2000 GEANT MC.

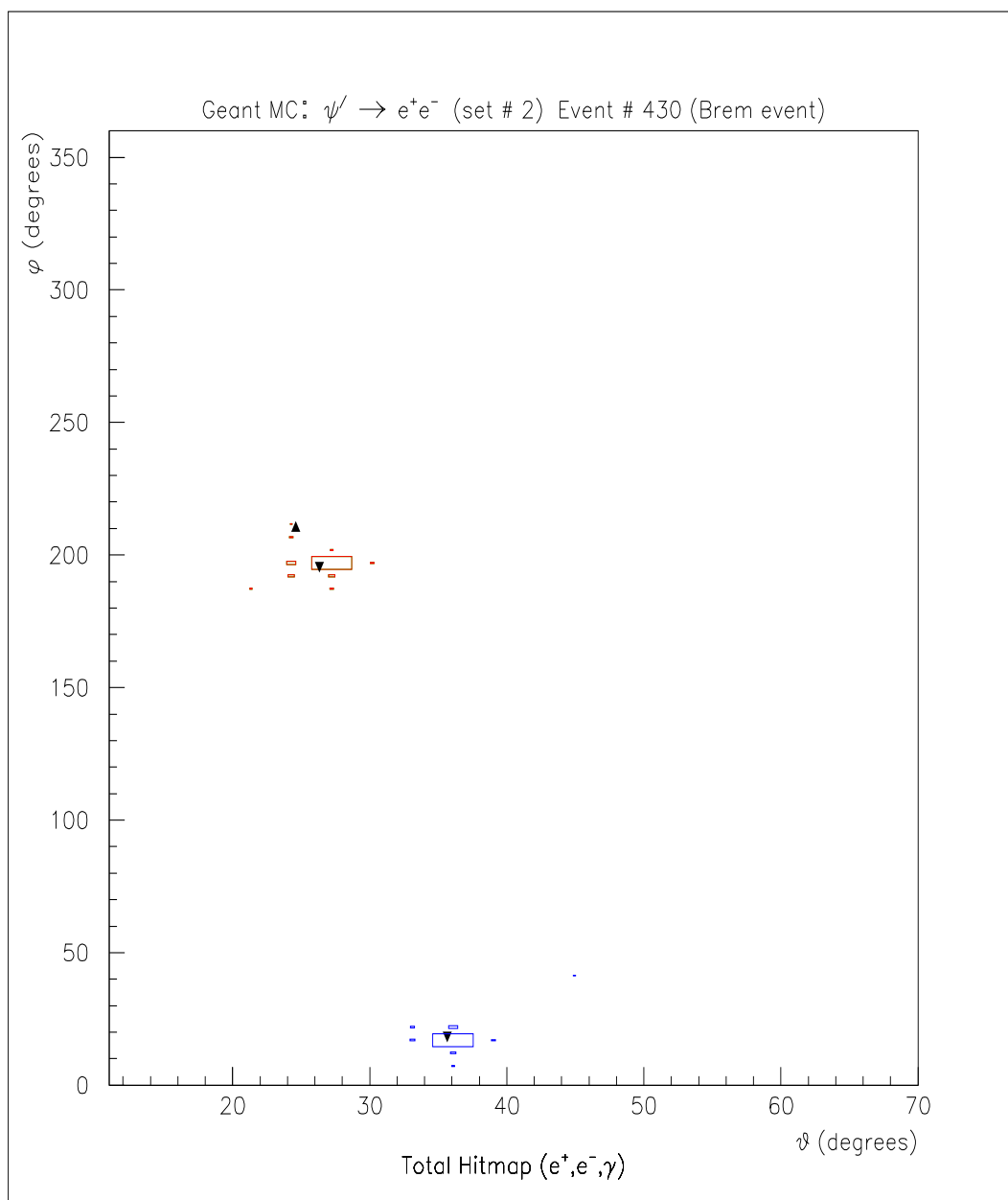


Figure 5.4: A 2-cluster event is interpreted as a 3-cluster event in the CCAL by a clusterizer Boxes represent hit map and arrows represent clusters (two down-pointing triangles represent main clusters and one up-pointing triangle represents a secondary cluster).

### 5.2.3 CCAL Timing

Another effect which needs to be taken into account in the analysis is called “pileup”. This happens when an unrelated event occurs within the same time interval as the triggered event. To minimize the effect of pileup events, the timing of the clusters in the event was used to identify clusters not associated with the interaction. This was especially significant for data taken at high instantaneous luminosities.

The timing information of each CCAL block was obtained using a multihit TDC with 1 ns resolution. This information was classified into three types: “in-time”, “out-of-time” and “undetermined”. “In-time” (“out-of-time”) was assigned to a hit within (outside of) a 20 ns window centered around the mean event time. For cases where there was no timing information, which happened when a signal was below threshold, the timing information of the block was classified as “undetermined”.

The timing of a cluster was determined by either its seed or by the second highest energy block if the seed timing was “undetermined”. If the timing of the second highest energy block was also “undetermined”, then the timing of the whole cluster was classified as “undetermined”.

The efficiency and resolution of the cluster-timing algorithm was tested using  $\pi^0\pi^0$  events with the “split” clusters excluded. The result showed that 99.5% of the clusters above a 50 MeV threshold were “in-time”. At higher instantaneous luminosities, the number of out-of-time and low-energy clusters increased.

## 5.3 Event Selection

The logical sequence of the  $e^+e^-$  event selection was 1) choosing a proper seed/cluster threshold, 2) counting the number of clusters, 3) selecting the cluster timing, 4) determining geometrical acceptance, 5) electron identification, 6) the cluster mass and the invariant mass <sup>4</sup>. The first four criteria were used to select all the exclusive  $e^+e^-$  candidate events. From these the final events were selected by applying the remaining criteria to the events. A GEANT Monte Carlo study was

---

<sup>4</sup>There are two types of invariant mass: invariant mass between a main cluster and its secondary cluster, and invariant mass between two main clusters.

conducted to estimate the selection efficiency of each of these criteria. The following subsections describe the event selection procedure in detail.

### **Seed/cluster threshold $\rightarrow$ 50/50 MeV**

The seed and cluster threshold were both set at 50 MeV. This value was selected to ensure the efficient reconstruction of the  $\psi'$ , which has large electron energies, while efficiently suppressing the  $\pi^0$  background. It was found that these thresholds were strongly correlated with the number of clusters in an event; as they were lowered the number of spurious clusters increased. It was estimated with the Monte Carlo that a higher threshold of 100/100 MeV, the number of secondary clusters would decrease to 1.2% and 0.2% in the 1996-1997 and 2000 runs, respectively (See Table 1 and 2 in Appendix C), but this change would lead to a loss in efficiency. While with a lower threshold of 25/50 MeV, the number of secondary clusters would increase to  $(5.5 \pm 0.1)\%$  and  $(5.0 \pm 0.1)\%$ . The value of 50/50 was chosen to ensure that the detector efficiency was in a well-understood region. The relation between the seed/cluster threshold and the number of clusters is discussed more in detail in the next selection and in Appendix C.

### **Number of clusters $\rightarrow$ 2 $\sim$ 4**

As discussed earlier some showers can have satellite or secondary clusters. For high-energy electrons (or positrons) this can occur with a relatively high frequency. For the cases when this occurs in the inner detectors or the beam pipe, the photon and the electron have a wide opening angle only if energy is large enough, and the two resultant showers can be detected as separate clusters. For the case where secondary clusters are due to the lateral spread of the shower (“shower splash”) in the CCAL, there may be two reconstructed clusters associated with the electron. Both these types of secondary clusters have to be considered in the analysis.

These two phenomena, “shower splash” and bremsstrahlung, were studied using the GEANT MC, described in detail in Appendix C. Results of this study showed that both “shower splash” and bremsstrahlung decrease as the seed/cluster threshold increases, with the level of decrease faster for “shower splash”. With the 50/50 MeV



threshold, it was found that  $(52.2 \pm 2.4)\%$  and  $(58.9 \pm 3.4)\%$  of all the secondary-cluster events were due to “shower splash” in the 1996-1997 MC and the 2000 MC, respectively. Figure 5.5 shows the number of events without secondary clusters divided by the total number of events as a function of the seed/cluster thresholds. These plots show how the fraction of the 2-cluster events increases as the seed/cluster threshold increases and saturates from 80/80 MeV on. The saturation level was lower in the 1996-1997 MC ( $\sim 99\%$ ) than that in the 2000 MC ( $\sim 100\%$ ), due to the presence of the silicon detector, which was removed before the 2000 run.

There are two competing effects at play here: with a higher threshold, the number of events with secondary clusters decreases but this could lead to failure of the kinematic fit discussed later, or With a lower threshold, the number of events from the cascade decay channel ( $\psi' \rightarrow J/\psi X$ ) could increase. The value of 50/50 MeV for this selection was therefore chosen.

A limit on the number of secondary clusters of two was applied to allow situations where both the two main clusters had their own secondary clusters.

### Cluster timing

For each main cluster of  $e^+e^-$  candidates, “in-time” was required. For their secondary clusters, either “in-time” or “undetermined” was accepted.

### Acceptance

The geometrical acceptance of each main cluster of the  $e^+e^-$  candidates was limited to the angular coverage of the Čerenkov counter, which was  $15^\circ < \theta_{lab} < 60^\circ$ . For secondary clusters, a relatively loose selection was applied: they were only required to be  $12^\circ < \theta_{lab} < 70^\circ$  of the CCAL.

### Invariant mass between primary and its secondary clusters

An invariant mass cut of  $m_{e\gamma} < 0.2$  GeV for the main cluster and the secondary cluster ( $m_{e\gamma}$ ) was applied. This value was selected after a GEANT MC study (See Figure 5.6). In MC, the invariant mass ( $m_{e\gamma}$ ) distribution has a clear fall-off at 0.2 GeV, but the same is not true in data. This is due to events in the data with secondary clusters that are neither from bremsstahlung nor “shower splash”. This

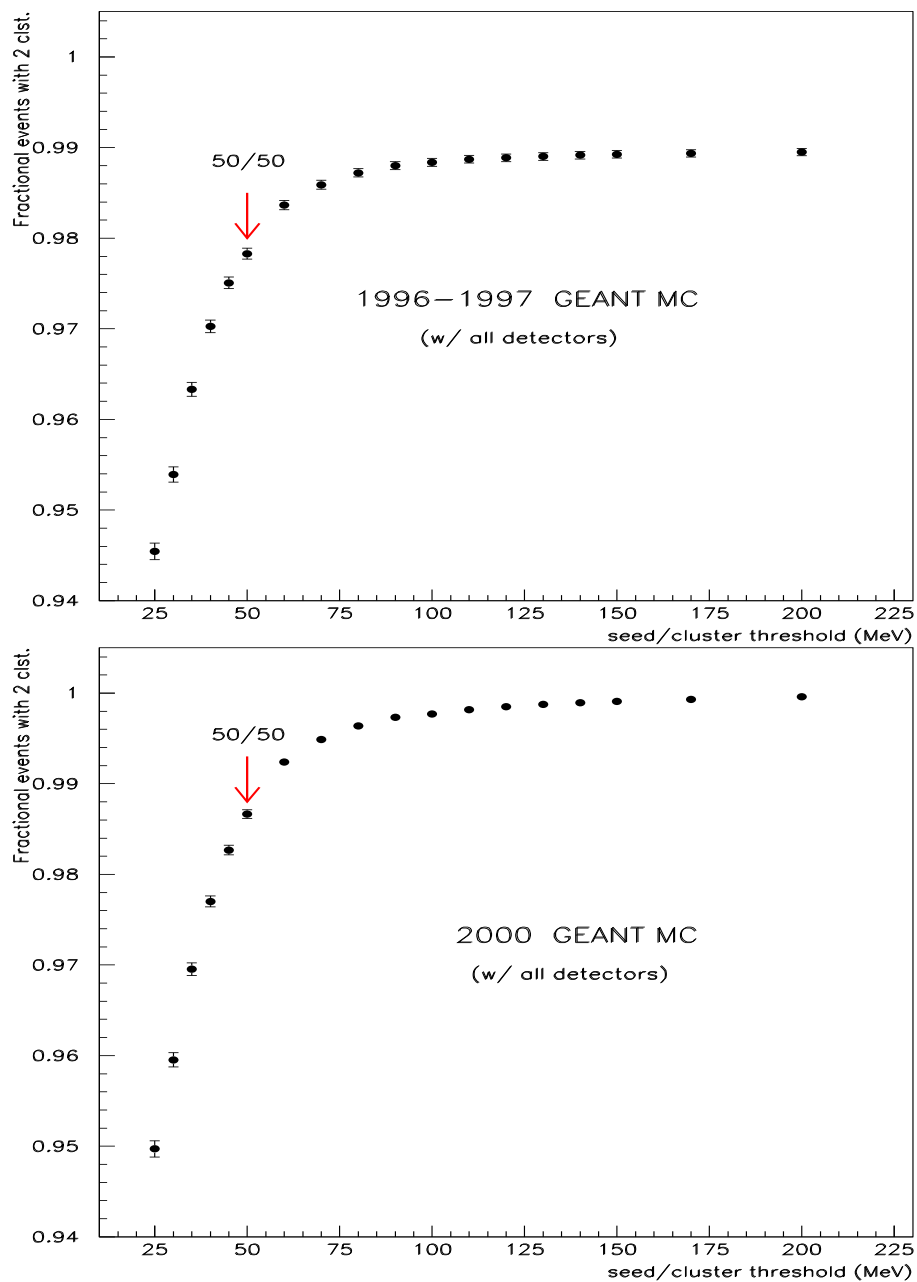


Figure 5.5: Seed/cluster threshold dependency of 2-cluster events normalized to the total # of events using the 1996-1997 MC (top) and the 2000 MC (bottom).

selection step removed many background events from the data, about 80% of the pre-selected events.

#### **4C Kinematic Fit: Probability $> 10^{-4}$**

A kinematic fit of the events was accomplished using the SLAC routine SQUAW. A 4-constraint (4C) fit was used to select events with a probability greater than  $10^{-4}$ . For the events with secondary clusters, this 4C fit was performed after combining the energy of the secondary cluster to that of its main cluster. If the event failed, then the 4C fit was repeated with the 4 momentum of the secondary cluster added to that of the main cluster. Figure 5.7 shows side-by-side the probability distributions of the 4C fits from MC (left) and from actual data (right).

#### **Electron Identification**

Reliable identification of the electron or positron produced in the decay of a charmonium state was essential as only the electromagnetic final states ( $e^+$ ,  $e^-$  and  $\gamma$ ) were detected. Possible backgrounds for the electron or positron from a charmonium decay were misidentified pions ( $\pi^+$  or  $\pi^-$ ) as well as conversion of a photon in the beam pipe or from Dalitz decay of  $\pi^0$ . To quantify this, a variable called electron weight (EW) was defined [68]. It was the ratio of the likelihood function for an electron (positron) hypothesis ( $L_e$ ) to the likelihood function for background hypothesis ( $L_{bg}$ )<sup>5</sup>:

$$EW(x_1, \dots, x_n) = \frac{L_e(x_1, \dots, x_n)}{L_{bg}(x_1, \dots, x_n)} \quad (5.3)$$

where  $x_1, \dots, x_n$  are a set of variables for an event measured by the detectors for electron (positron) identification. These were the three sets of hodoscopes (H1, H2' and H2), the Čerenkov counter and the CCAL. The hodoscopes provided information on the energy loss of a charged particle in the plastic scintillators. The Čerenkov counter was set to discriminate against charged pions. The CCAL was used to determine the cluster mass shape, which is different for electrons and the backgrounds

---

<sup>5</sup>This method is also known as the Neyman-Pearson test [69].

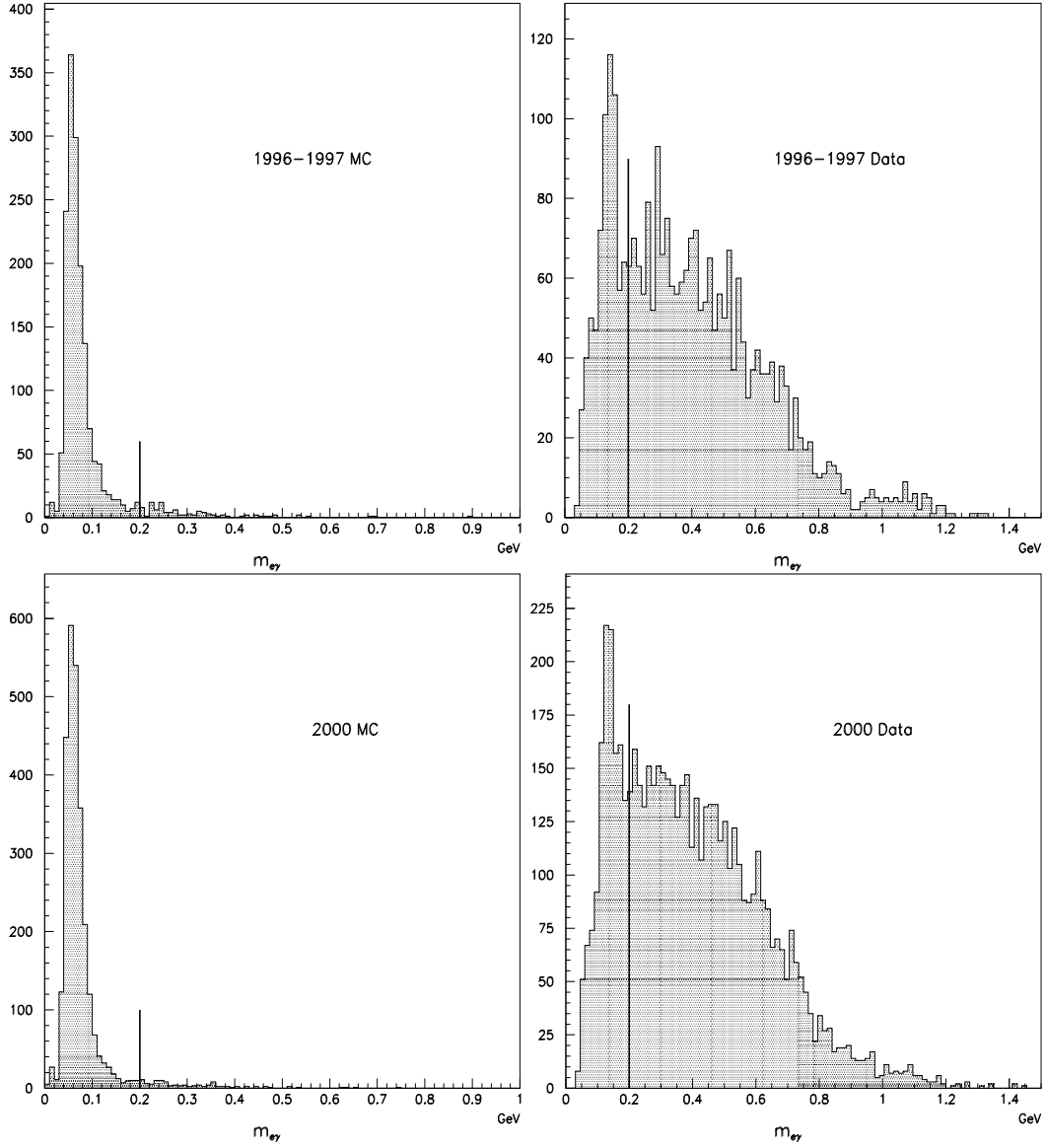


Figure 5.6: Invariant mass distribution between  $e^-$  ( $e^+$ ) and its secondary cluster. Top: the 1996-1997 MC (left) and data (right), Bottom: the 2000 MC (left) and data (right). No other selections were applied except for pre-selection criteria (see Table 5.2).

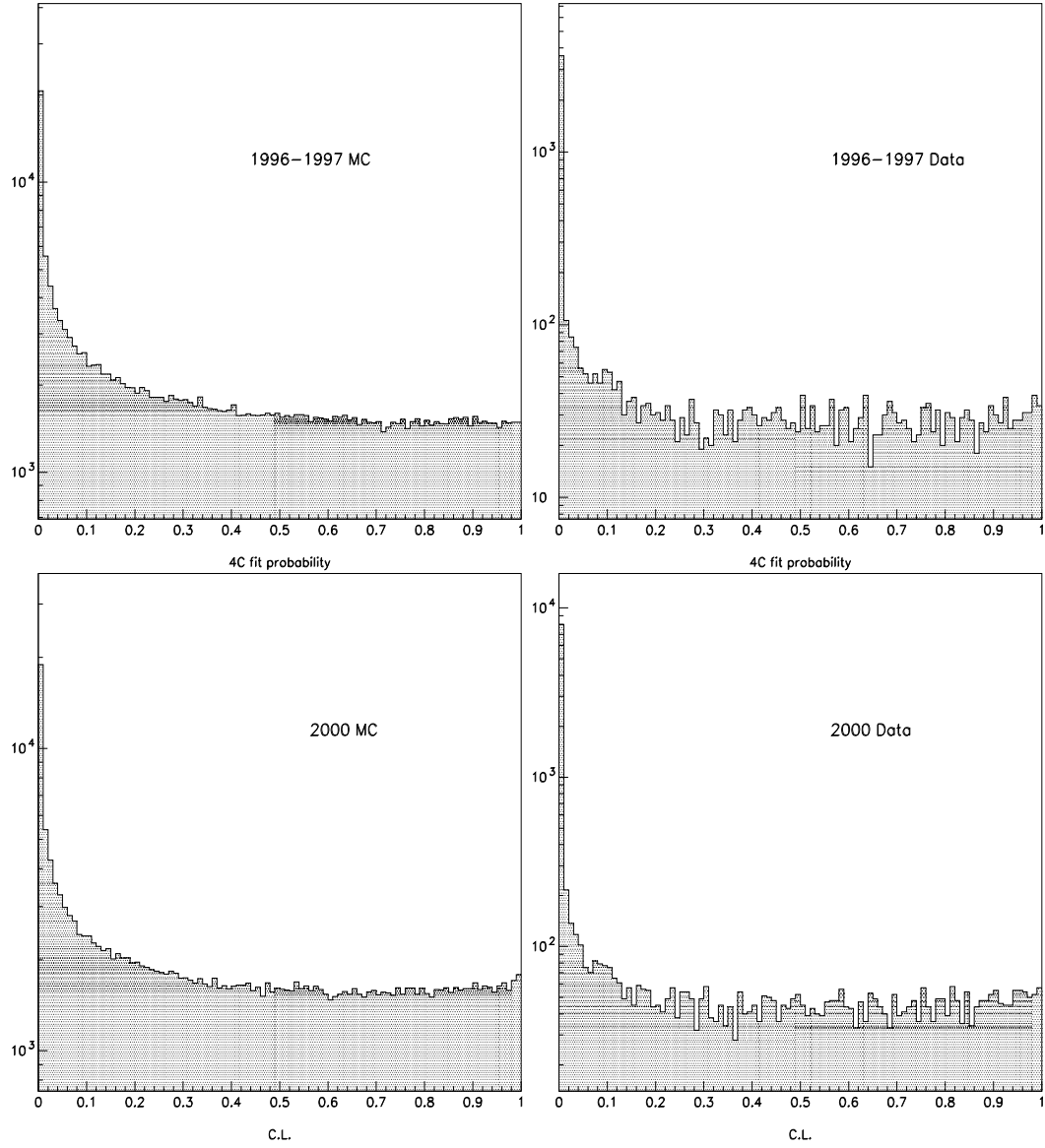


Figure 5.7: The probability distribution of the 4C fit. Top: the 1996-1997 MC (left) and data (right), Bottom: the 2000 MC (left) and data (right). No other selections were applied except for pre-selection criteria (see Table 5.2).

(see Figure 5.2).

Specifically, the input variables  $x_i$  for the EW are as follows:

- 1)  $\frac{dE}{dx}$  in H1, H2' and H2, respectively.
- 2) Čerenkov pulse height.
- 3) second moments ( $s.m.$ ) of a cluster measured along rings ( $r$ ) and wedges ( $w$ ) defined as:

$$s.m.(r) = \frac{\sum_{r,w=1}^3 E(r, w) \cdot (r - r_0)^2}{\sum_{r,w=1}^3 E(r, w)}$$

$$s.m.(w) = \frac{\sum_{r,w=1}^3 E(r, w) \cdot (w - w_0)^2}{\sum_{r,w=1}^3 E(r, w)}$$

where  $E(r, w)$  is the energy deposited in ring  $r$  and wedge  $w$  of the CCAL.

- 4) ratio of the energy deposited in a 3 x 3 to that in a 5 x 5 cluster.
- 5) ratio of the energy deposited in a 2 x 2 to that in a 4 x 4 cluster.
- 6) the cluster mass.

The value of EW for each of the two clusters was combined to form a single variable EW defined as  $EW(e^+) \times EW(e^-)$ . This combined variable was used to quantify the probability that an event was electron. Figure 5.8 shows the  $\log_{10}$  distributions of the combined EW from the pre-selected  $e^+e^-$  candidates (white) and from the background data <sup>6</sup> (hatched). Based on this distribution an  $EW > 10^{-4}$  threshold was adopted. Further investigation showed that selecting  $10^{-5}$  or  $10^{-3}$  had a negligible effect ( $< 1.5\%$ ) on the final event selection process.

### **Cluster mass of $e^+e^-$ candidates $< 0.12$ GeV**

For  $e^+e^-$  candidate events, the cluster mass ( $m_{cl}$ ) of the main clusters was required to be less than 0.12 GeV, to prevent a potential contamination of the data by coalesced  $\pi^0$ 's. In the analysis the cluster splitting procedure for "split" clusters was turned off. Figure 5.9 shows the cluster mass ( $m_{cl}$ ) distribution from MC and

---

<sup>6</sup>The background data was from the stack 54 where  $E_{cm} \sim 3704$  MeV and  $E_{cm} \sim 3666$  MeV.

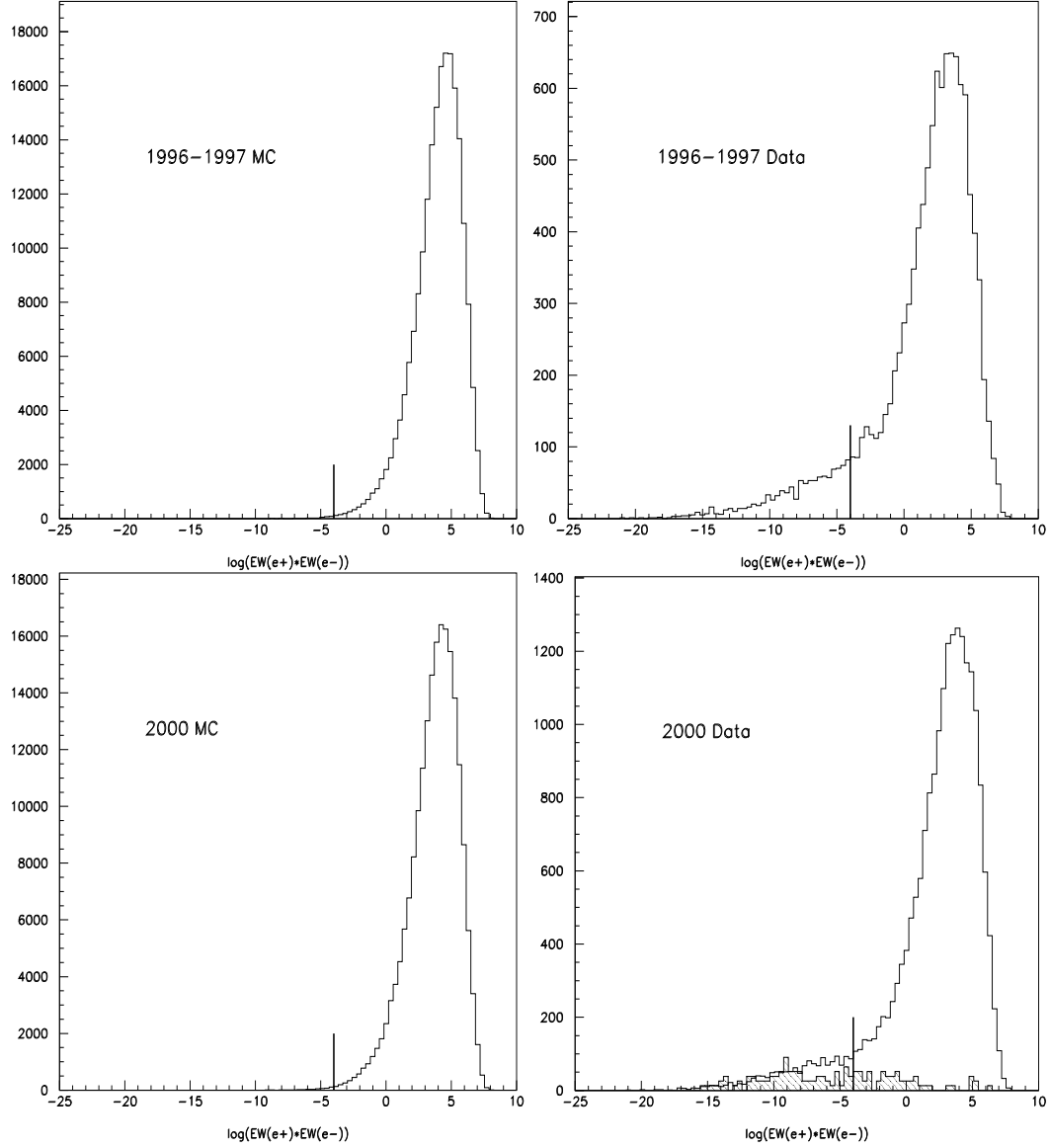


Figure 5.8: A  $\log_{10}$  plot of the electron weight (EW) distribution. Top: the 1996-1997 MC (left) and data (right), Bottom: the 2000 MC (left) and data (right). The hatched area in the 2000 data was obtained by background events. No other selections were applied except for pre-selection criteria (see Table 5.2).

data. The cluster mass of the MC events did not exceed 0.12 GeV while data had a tail extending beyond 0.12 GeV, attributed to background  $\pi^0$ 's.

### **Invariant mass between the two main clusters $> 3.4$ GeV**

A selection on the invariant mass ( $m_{ee}$ ) between the two main clusters of  $e^+e^-$  candidates was made with  $m_{ee} > 3.4$  GeV. This was to remove  $e^+e^-$  events from  $J/\psi$  decays, where the  $J/\psi$  is produced inclusively. Figure 5.10 shows the invariant mass distribution between the two main clusters of the  $e^+e^-$  events from MC and data. The white area represents the preselected events and the shaded area ( $> 3.4$  GeV) represents the finally selected events.

As part of pre-selection of events, clusters identified as “split” clusters are not to be split (“split” OFF). As described in the previous section, the purpose of introducing the “split” cluster was to split (“split” ON) a coalesced  $\pi^0$  which was detected as one cluster. For this  $e^+e^-$  analysis, there was less chance of finding “split” clusters which were caused by coalesced  $\pi^0$ s when as a good electron identification had been already made. To check the effect of “split” OFF, the GEANT MC study was performed. This was established as follows: A total of 100,000  $e^+e^-$  events was generated using the 2000 MC with a uniform angular distribution ( $\lambda = 0$ ) and passed through the detector. To avoid potential sources of a fake angular distribution, all dead blocks were revived and no septum existed in the Čerenkov counter; In this condition, the detector was considered to be an ideal one. The  $e^+e^-$  events were selected requiring 4C kinematic fit (probability  $> 10^{-5}$ ), acceptance ( $15^\circ < \theta_{lab} < 60^\circ$  for  $e^+e^-$  and  $12^\circ < \theta_{lab} < 70^\circ$  for the secondary clusters) and timing (“in-time” for  $e^+e^-$  and “in-time” or “undetermined” for the secondary clusters). In Figure 5.11 the lower lines show the angular distribution of the reconstructed 2-cluster events (top plot) and of the reconstructed events with up to 2 secondary clusters (bottom plot). The upper lines represent generated  $e^+e^-$  events. Allowing events with secondary clusters, the efficiency was improved.

All selections used for the  $e^+e^-$  event selection are summarized in Table 5.2. Table 5.3 lists the number of 2-cluster events, 3-cluster events and 4-cluster events in the data. The similar statistics were obtained from the GEANT MC (Table 5.4).



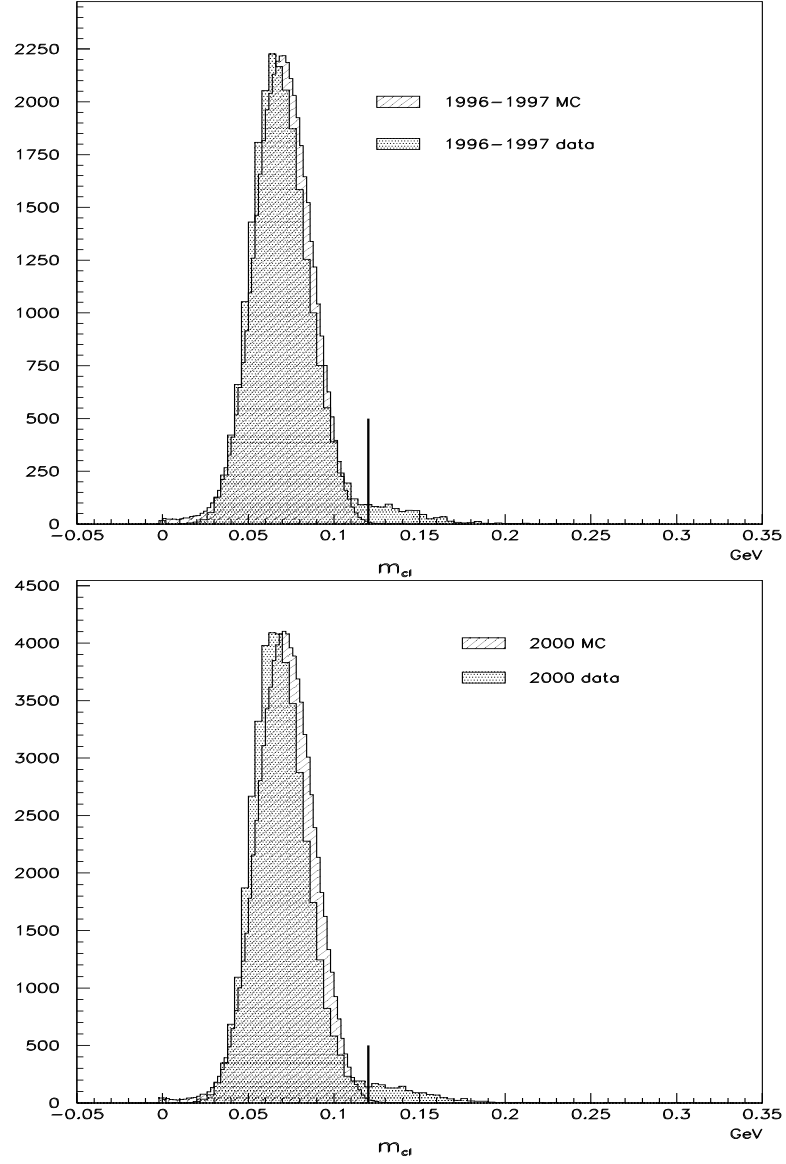


Figure 5.9: The cluster mass ( $m_{cl}$ ) distribution of the  $e^+e^-$  candidates. Top: the 1996-1997 MC (left) and data (right), Bottom: the 2000 MC (left) and data (right). No other selections were applied except for pre-selection cuts (see Table 5.2).

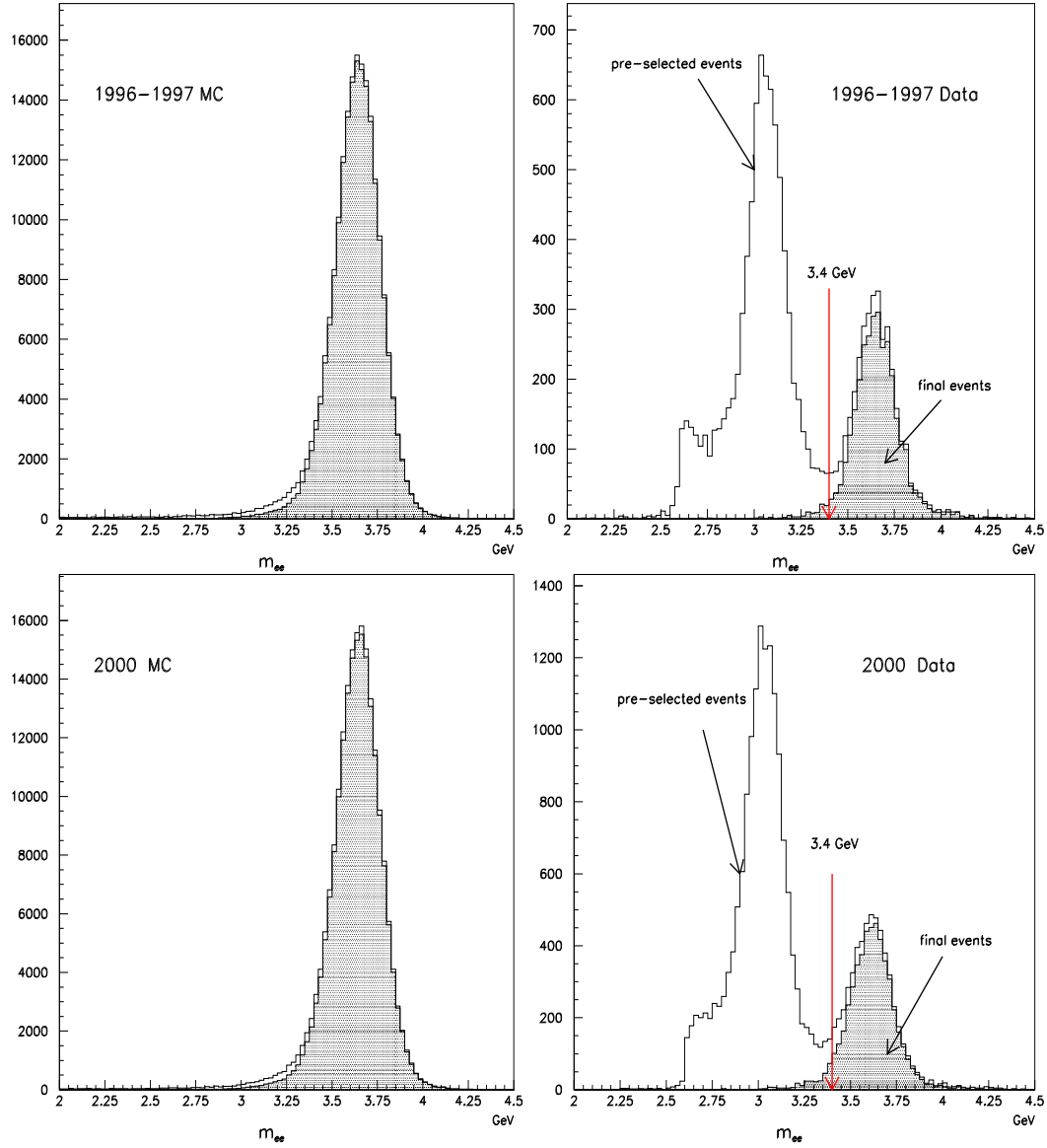


Figure 5.10: Invariant mass distributions of the  $e^+e^-$  candidates. Top: the 1996–1997 MC (left) and data (right), Bottom: the 2000 MC (left) and data (right). Shaded area ( $> 3.4$  GeV) represents finally selected events.

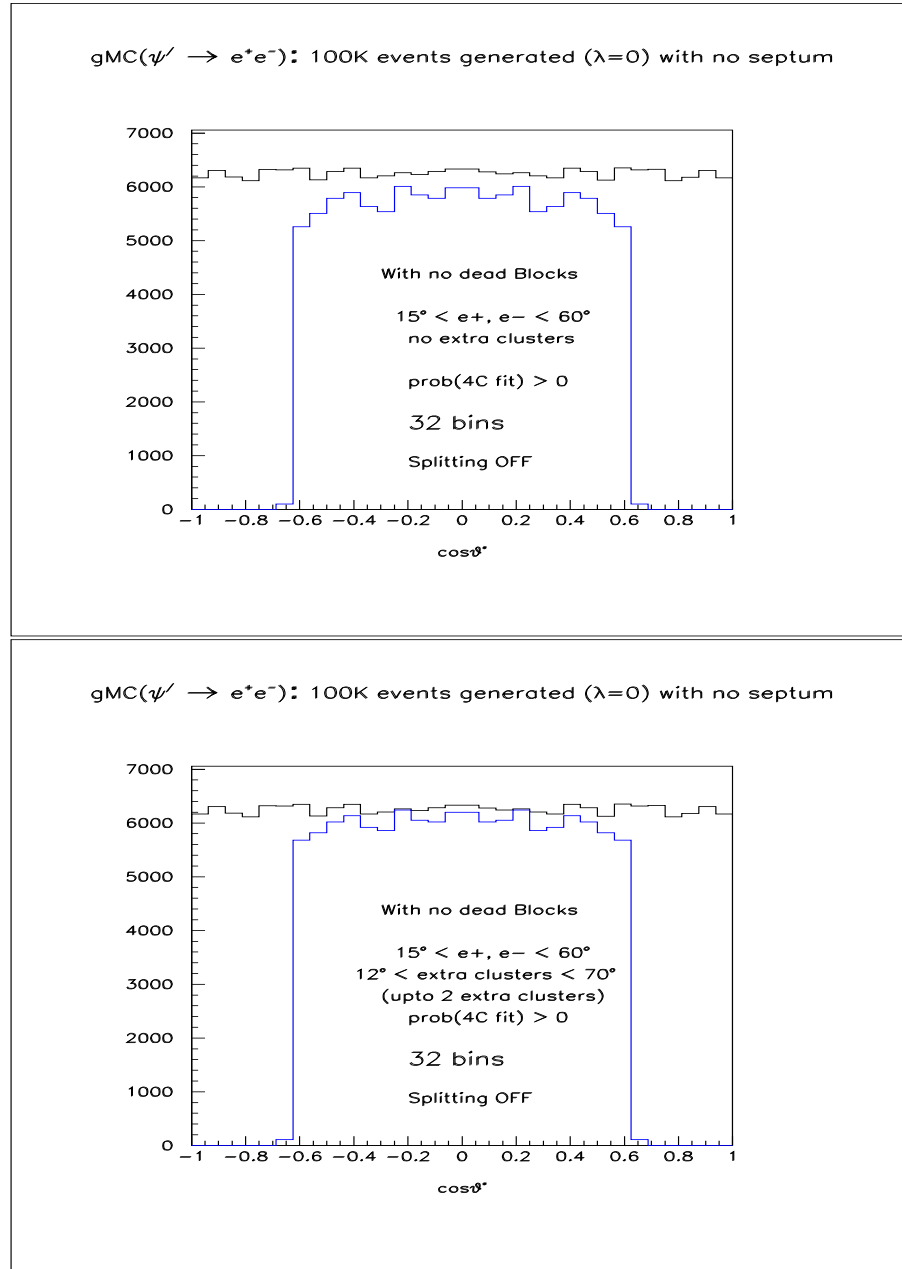


Figure 5.11: Angular distribution of the reconstructed events (lower lines) with “split” OFF. A total of 100,000  $e^+e^-$  events was generated using the 2000 GEANT MC with  $\lambda = 0$  (upper lines). (top: 2-cluster events, bottom: including events with up to 2 secondary clusters.)

Criteria	Selection value
Seed/cluster threshold *	$> 50/50$ MeV
“Split” cluster *	no splitting
# of clusters *	2 - 4
Timing *	“In-time” for the highest invariant mass pair “In-time” or “undetermined” for secondary clusters
Acceptance *	$15^\circ < \theta_{lab} < 65^\circ$ for the highest invariant mass pair $12^\circ < \theta_{lab} < 70^\circ$ for secondary clusters
Invariant mass between secondary cls. & its main cls.	$< 0.2$ GeV
Probability (4C fit)	$> 10^{-4}$
EW of $e^+e^-$ candidate	$> 10^{-4}$
Cluster mass of $e^+e^-$ candidate	$< 0.12$ GeV
Invariant mass between $e^+e^-$ candidate ( $m_{ee}$ )	$> 3.4$ GeV

Table 5.2: The different selections criteria applied for event selection (criteria with \* were used for the pre-selection of the events).

Data	# of events w/ 2 clsters	# of events w/ 3 clsters	# of events w/ 4 clsters	Total
1996-1997 pre-selection	2891 (29.8%)	2764 (28.5%)	4047 (41.7%)	9702
1996-1997 final selection	2176 (84.4%)	362 (14.0%)	41 (1.6%)	2579
2000 pre-selection	6151 (30.2%)	5821 (28.6%)	8400 (41.2%)	20372
2000 final selection	4691 (97.3%)	124 (2.6%)	8 (0.2%)	4823

Table 5.3: The number of pre-selected events and the number of finally selected events from the 1996-1997 data (top 2 rows) and from the 2000 data (bottom 2 rows).

GEANT MC	# of events w/ 2 clusters	# of events w/ 3 clusters	# of events w/ 4 clusters	Total
1996-1997 pre-selection	199129 (97.8%)	3788 (1.9%)	683 (0.3%)	203600
1996-1997 final selection	176852 (98.0%)	3035 (1.7%)	547 (0.3%)	180434
2000 pre-selection	200888 (98.6%)	2777 (1.4%)	39 (0.0%)	203704
2000 final selection	180056 (98.8%)	2096 (1.2%)	26 (0.0%)	182178

Table 5.4: The number of pre-selected events and the number of finally selected events from the 1996-1997 (top 2 rows) and the 2000 GEANT MC (bottom 2 rows). A total of 330,000 MC  $e^+e^-$  events was generated with  $\lambda = 0$  at the  $\psi'$ .

Using these event selection criteria, a total of 2579 and 4823 events were selected in the range of  $0 < \cos\theta^* < 0.6$  for the 1996-1997 and 2000 data, respectively. The final number of events, normalized for luminosity, in the 1996-1997 data was less by  $(34 \pm 2.4)\%$  than that in the 2000 one. The most likely reason why there were fewer events in the 1996-1997 data is that the beam energy distribution was broader during the 1996-1997 run than during the 2000 run. However, this cannot be verified because no information on the beam energy distribution is available for the 1996-1997 data.

## 5.4 Background Study

A study was conducted to investigate the probability that  $e^+e^-$  events could have their origin in processes other than direct  $\psi' \rightarrow e^+e^-$  decay. The limited geometrical acceptance of the detector could lead to  $\psi'$  cascade decays to final states such as  $J/\psi \eta$ ,  $J/\psi \pi^0\pi^0$  and  $J/\psi \pi^+\pi^-$ , being selected as  $\psi' \rightarrow e^+e^-$  events. The level of these backgrounds was studied using the GEANT MC. The MC events of each channel were generated with their own angular distribution. The same selection criteria were applied to the events. Table 5.5 lists the possible channels and the predicted number of background events from them. The number of these background events were normalized to the total number of selected  $\psi' \rightarrow e^+e^-$  events. The estimated background levels is 0.05% and 0.14% from all of these processes for the 1996-1997 and 2000 data, respectively. Since these levels of background are negligible compared to the number of selected events, no background subtraction from these sources were made.

## 5.5 Contribution from Continuum

To estimate the number of events coming from the direct continuum process,  $\bar{p}p \rightarrow e^+e^-$ , off-resonance data were used with the same event selection criteria. The 1996-1997 off-resonance data were taken at the center-of-mass energies between  $3576 \sim 3660$  MeV ( $32.7 \text{ pb}^{-1}$ ) and from this the contribution to the signal from the

Background channel	Predicted # of BG events (1996 - 1997)	Predicted # of BG events (2000)
$J/\psi \eta$	0.28	0.24
$J/\psi \pi^0 \pi^0$	0.10	1.21
$J/\psi \pi^+ \pi^-$	1.17	5.23
Total	1.35	6.68

Table 5.5: Possible  $e^+e^-$  background channels and the corresponding number of mis-identified background events.

continuum process was estimated to be  $(9.5 \pm 1.7)$  events. The 2000 off-resonance data were at 3526 MeV ( $32.4 \text{ pb}^{-1}$ ) and at 3666 and 3705 MeV ( $0.9 \text{ pb}^{-1}$ ). From these data the estimated number of continuum events was  $(10.9 \pm 2.1)$  from the lower energy region and  $(6.8 \pm 6.8)$  from the higher energy region. These continuum levels were negligible compared with the 2579 and 4823 events.

## 5.6 Efficiency

Measuring the angular distribution does not require an overall efficiency correction, but, any non-uniform inefficiency that can affect the angular distribution, must be taken into account. To investigate this, the efficiency of the pileup correction and the selection efficiency including geometrical acceptance were studied using GEANT MC. This is described in detail in the following subsections.

### 5.6.1 Pileup Efficiency

The pileup correction efficiency was studied to investigate there was any influence from pileup events on the angular distribution, since excluding some events due to pileup in the course of event selection, could cause a change in the angular distribution measurement. To obtain the pileup efficiency, data collected using the



10 kHz pulser during data taking, were used to mimic pileup events in the MC simulation. The strategy is to count the number of events after applying all analysis cuts separately to two sets of data generated with GEANT MC, one with pulser data overlayed and one without. The pileup efficiency was defined as the ratio of the two final number of events:

$$\epsilon_{pileup} \equiv \frac{\# of events w/ pileup}{\# of events w/o pileup} \quad (5.4)$$

Since the number of pileup events increases with a higher  $\bar{p}p$  interaction rate, the pileup efficiency ( $\epsilon_{pileup}$ ) depends on the interaction rate as well. To estimate the pileup efficiency for any given instantaneous luminosity ( $L_{inst}$ ), three pileup efficiencies are obtained for different values of  $L_{inst}$  and then from a fit to these value the pileup efficiency for any  $L_{inst}$  can be estimated. In Figure 5.12 is shown the  $\epsilon_{pileup}$  as a function of the instantaneous luminosity ( $L_{inst}$ ). Three data points in the 1996-1997 plot were taken at MCRUN 1281, 2221 and 1276 and using the corresponding RG events. The average instantaneous luminosities were (1.59, 2.01 and 2.81)  $\times 10^{31}\text{cm}^{-2}\text{s}^{-1}$ , respectively. Their pileup efficiencies were obtained as  $0.9039 \pm 0.0020$ ,  $0.8774 \pm 0.0021$  and  $0.8206 \pm 0.0020$ , respectively. Three data points in the 2000 plot were taken at MCRUN 5258, 5830 and 5571 and using the corresponding RG events. The average instantaneous luminosities were (0.967, 1.52 and 3.01)  $\times 10^{31}\text{cm}^{-2}\text{s}^{-1}$ , respectively. Their pileup efficiencies were obtained as  $0.8752 \pm 0.0012$ ,  $0.8366 \pm 0.0017$  and  $0.7127 \pm 0.0011$ , respectively.

A linear fit was applied to these data points and the fit result was obtained as:

$$\epsilon_{pileup} = 1.014 - 0.069 \times L_{inst} \quad for \quad 1996 - 1997 \text{ MC} \quad (5.5)$$

$$\epsilon_{pileup} = 0.954 - 0.080 \times L_{inst} \quad for \quad 2000 \text{ MC} \quad (5.6)$$

which was used to estimate the pileup efficiency for any given  $L_{inst}$ .

The effect of pileup on the angular distribution measurement was studied. Figure 5.13 shows  $\epsilon_{pileup}$  as a function of  $\cos\theta^*$  at  $L_{inst} = 2.02 \times 10^{31}\text{cm}^{-2}\text{s}^{-1}$  for the

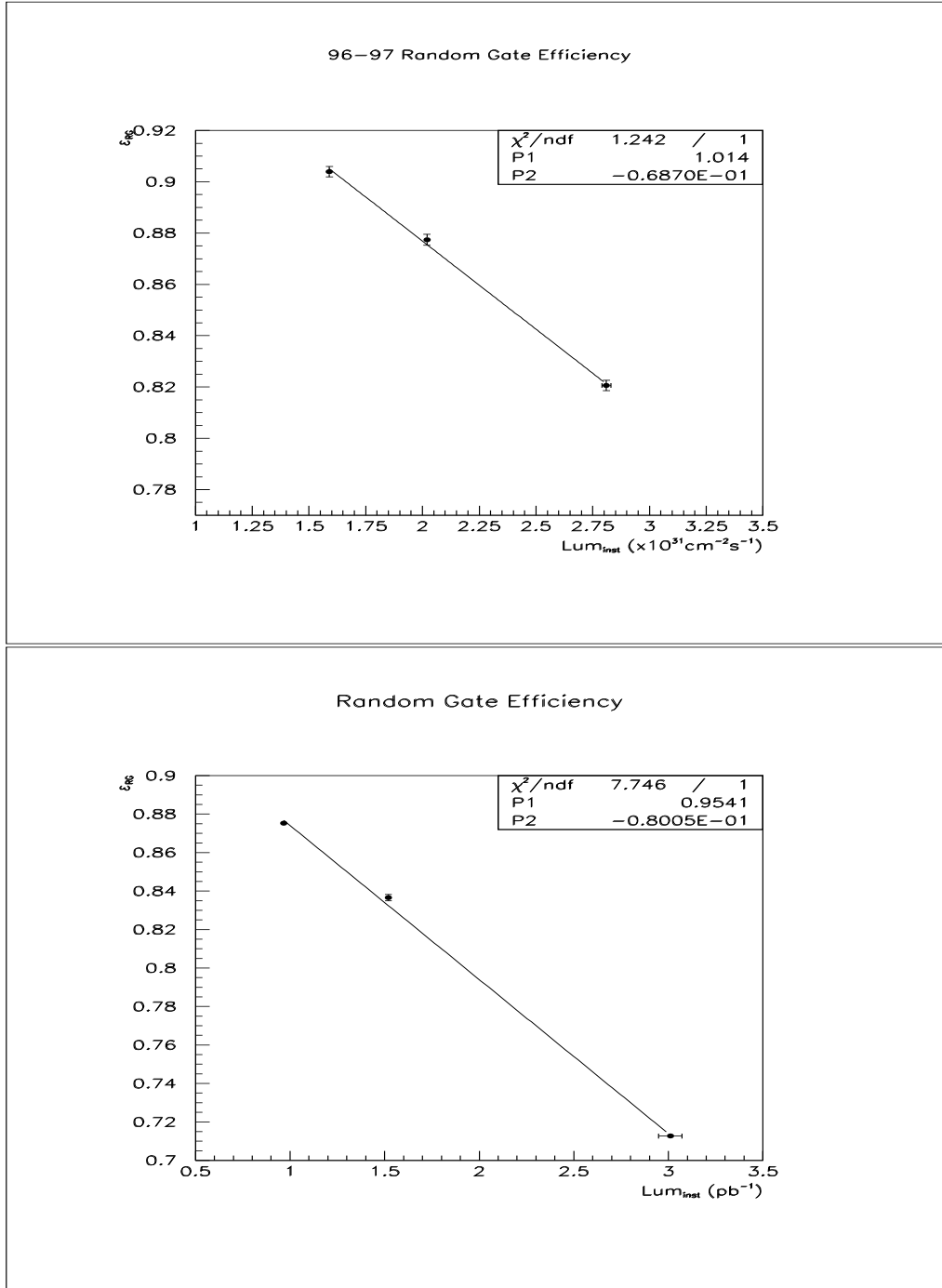


Figure 5.12: Pileup efficiency ( $\epsilon_{pileup}$ ) vs. instantaneous luminosity ( $L_{inst}$ ) from the 1996-1997 MC (top) and from the 2000 MC (bottom). The line is a fit to the MC data.

1996-1997 MC and  $L_{inst} = 3.01 \times 10^{-31} \text{cm}^{-2} \text{s}^{-1}$  for the 2000 MC. The pileup efficiency did not affect the angular distribution as shown in Figure 5.13, leading to the conclusion that the random events do not lead to a bias in the angular distribution measurement.

### 5.6.2 Event Selection Efficiency and Geometrical Acceptance

The only remaining efficiency which could affect our angular distribution was the event selection efficiency, which included the geometrical acceptance. To estimate this, the GEANT MC was used to generate a total of 330,000  $e^+e^-$  events with a uniform angular distribution ( $\lambda = 0$ ) at the  $\psi'$ . Figure 5.14 shows the selection efficiency, including the acceptance, as a function of  $\cos\theta^*$  from the 1996-1997 (top) and 2000 MCs (bottom). The overall efficiencies were  $\sim 90\%$  in both MCs. However, there were three inefficient regions (dips) at  $\cos\theta^* = 0.2$ ,  $0.35$  and  $0.6$ .

The inefficiency at  $\cos\theta^* = 0.2$  was caused by two dead calorimeter blocks in the CCAL ring number 8. (Figure 5.15 shows CCAL ring number as a function of  $\cos\theta^*$ .) In Figure 5.16 is shown the azimuth  $\phi$  as a function of  $\cos\theta^*$ . The two empty spots in the  $\cos\theta^* = -0.2$  region correspond to the two dead blocks. In the opposite direction, where  $\cos\theta^* = +0.2$ , the other particle of the pair does in fact register a signal but as this fails the kinematic fit for pairs, this region appears to have “mirror image” empty spots as well. A MC study was consistent with the conclusion that the dip in  $\cos\theta^* = 0.2$  was caused by the dead calorimeter blocks in that region. The selection efficiency as a function of  $\cos\theta^*$  with all dead blocks revived, is shown in Figure 5.17: the inefficiency at  $\cos\theta^* = 0.2$  has disappeared.

The inefficiency at  $\cos\theta^* = 0.35$  was due to the inefficient geometry in that region corresponding to CCAL ring number 13 and 14 (See Figure 3.5 in Chap. 3). Figure 5.18 shows the efficiency as a function of ring number. The solid, dashed and dotted lines are the efficiencies with 4C kinematic fit probability greater than  $10^{-5}$ , 1% and 5%, respectively. As the kinematic fit probability increases the inefficiency increases in the region, which means the region is inefficient.

The inefficiency in the  $\cos\theta^* = 0.6$  region was due to the limitation of the geometrical acceptance (edge of the detector).

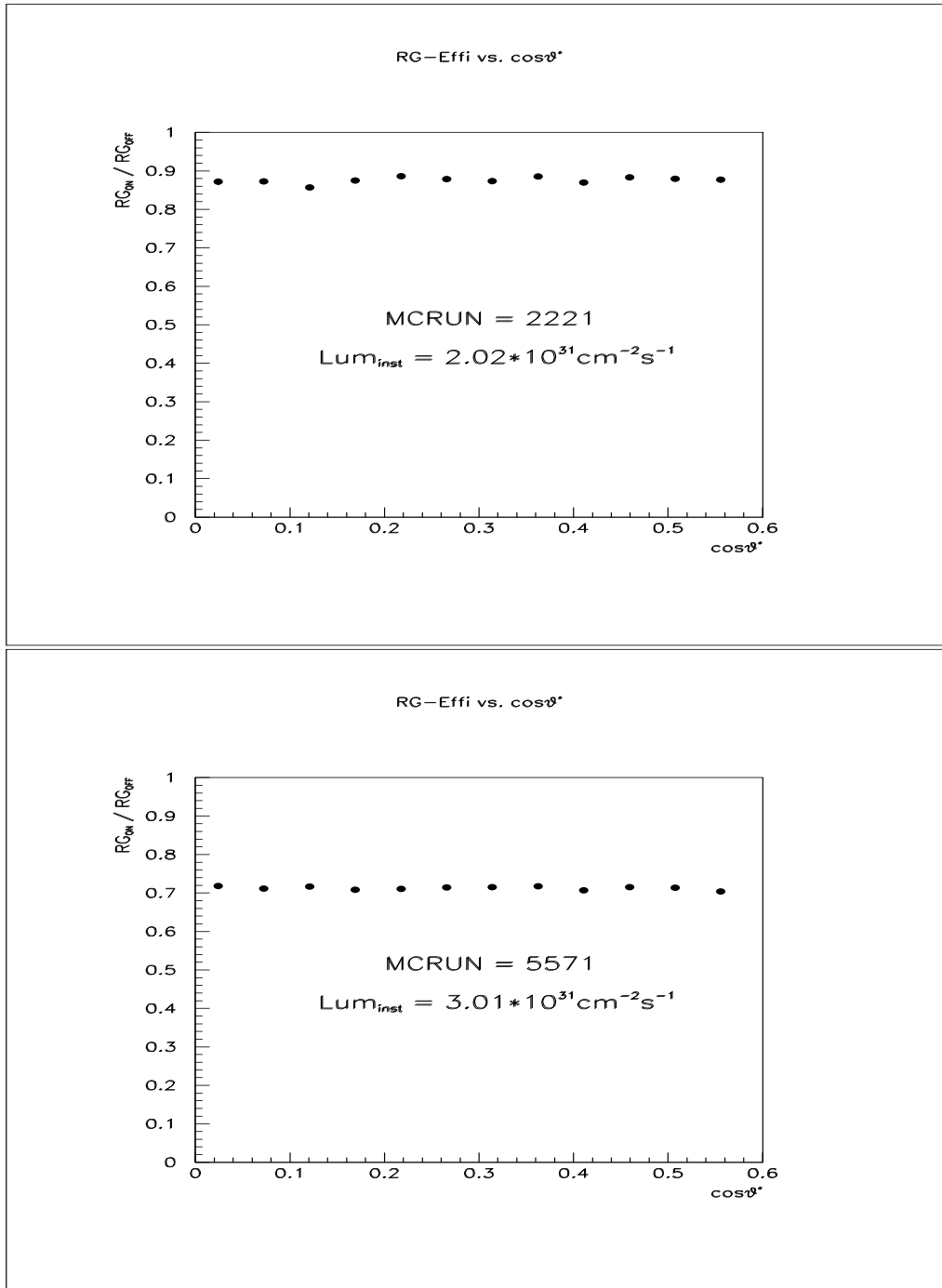


Figure 5.13: Pileup efficiency ( $\frac{RG_{ON}}{RG_{OFF}}$ ) vs.  $\cos\theta^*$  from the 1996-1997 MC (top) and from the 2000 MC (bottom).

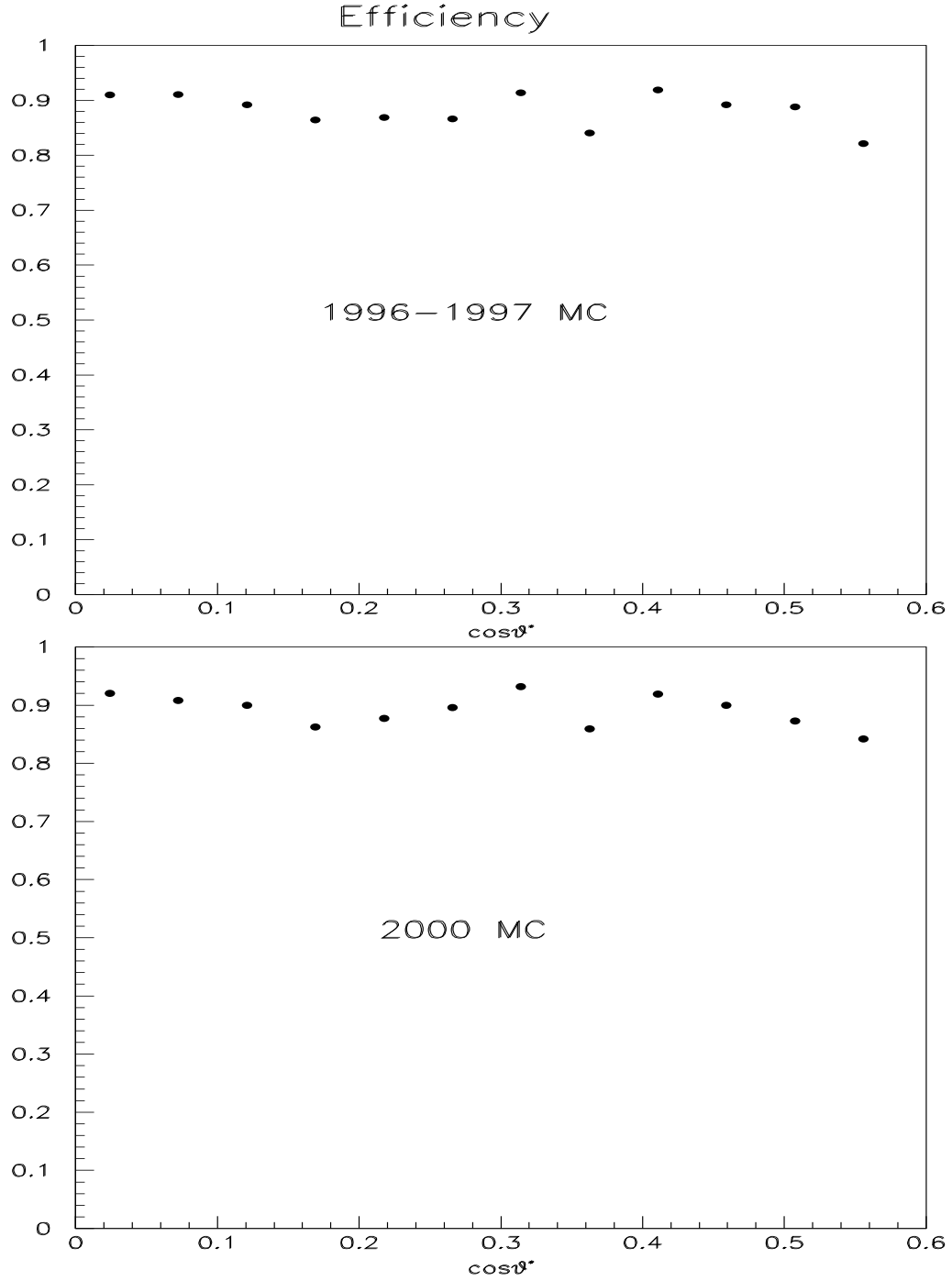


Figure 5.14: Event selection efficiency as a function of  $\cos\theta^*$ . A total of 330,000  $e^+e^-$  events with  $\lambda = 0$  was generated using the GEANT MC (top: from the 1996-1997 MC, bottom: from the 2000 MC).

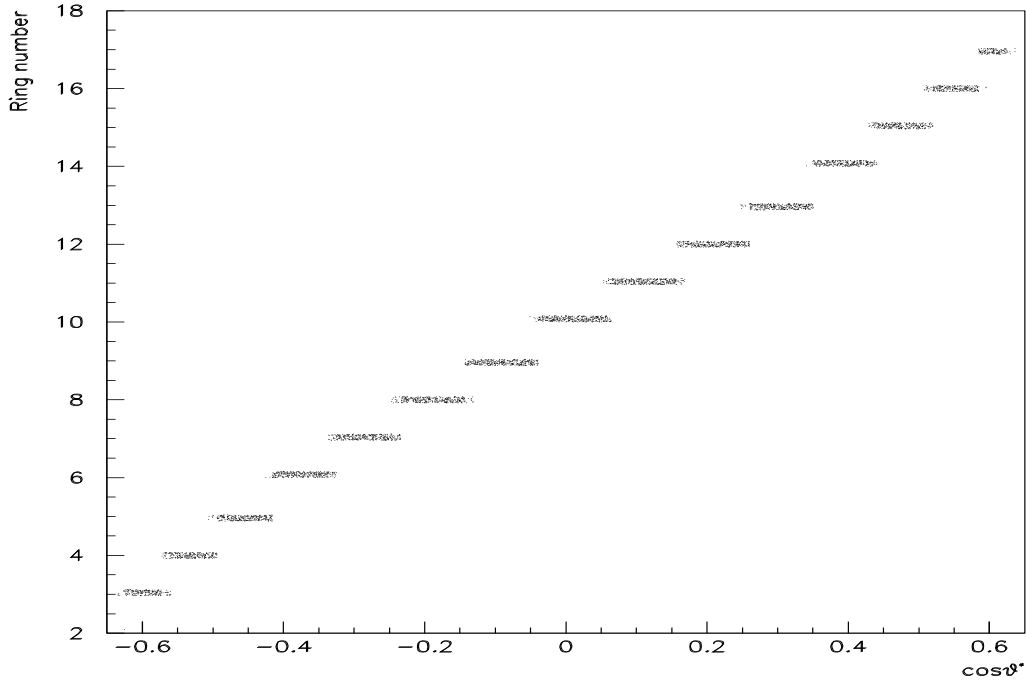


Figure 5.15: CCAL ring number vs.  $\cos\theta^*$  coverage.

An efficiency correction to the data was necessary and was made on a bin-by-bin basis. The bin size used to determine the efficiency was  $\Delta\theta_{lab} = 2.08^\circ$ , within the angular range of one CCAL block size ( $1.52^\circ \sim 4.80^\circ$ ), and the same bin size was used to bin the data. Figure 5.19 shows the angular distribution of the selected events before (black) and after (hatched) this efficiency correction.

The corrected data were used to extract the angular distribution parameter  $\lambda$ , which is described in the following chapter.

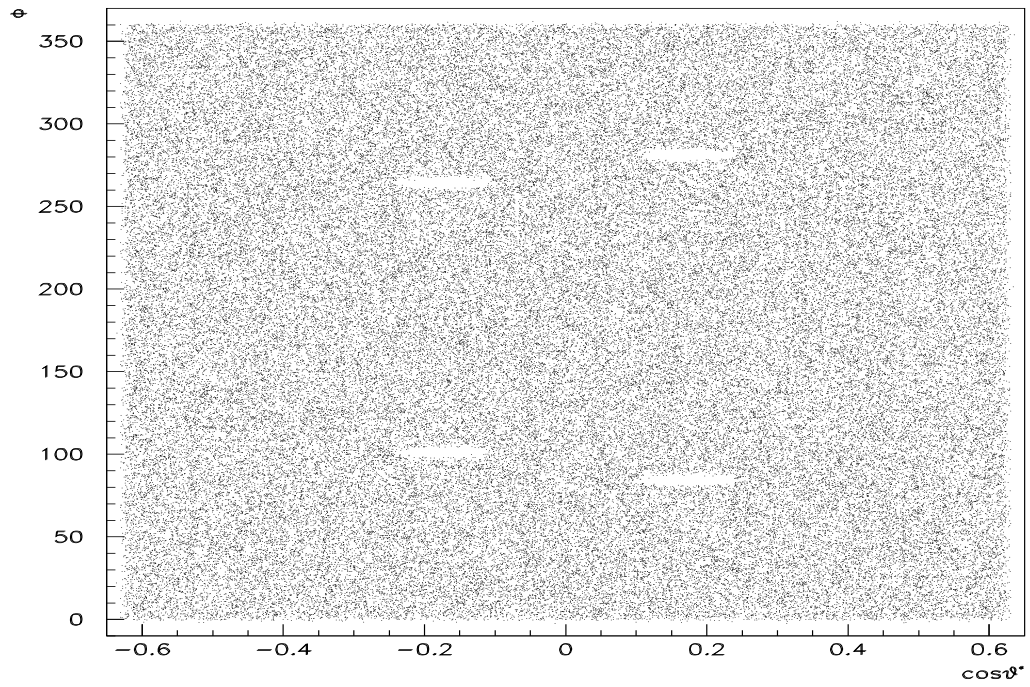


Figure 5.16:  $\phi$  vs.  $\cos\theta^*$  coverage (There are two entries per event).

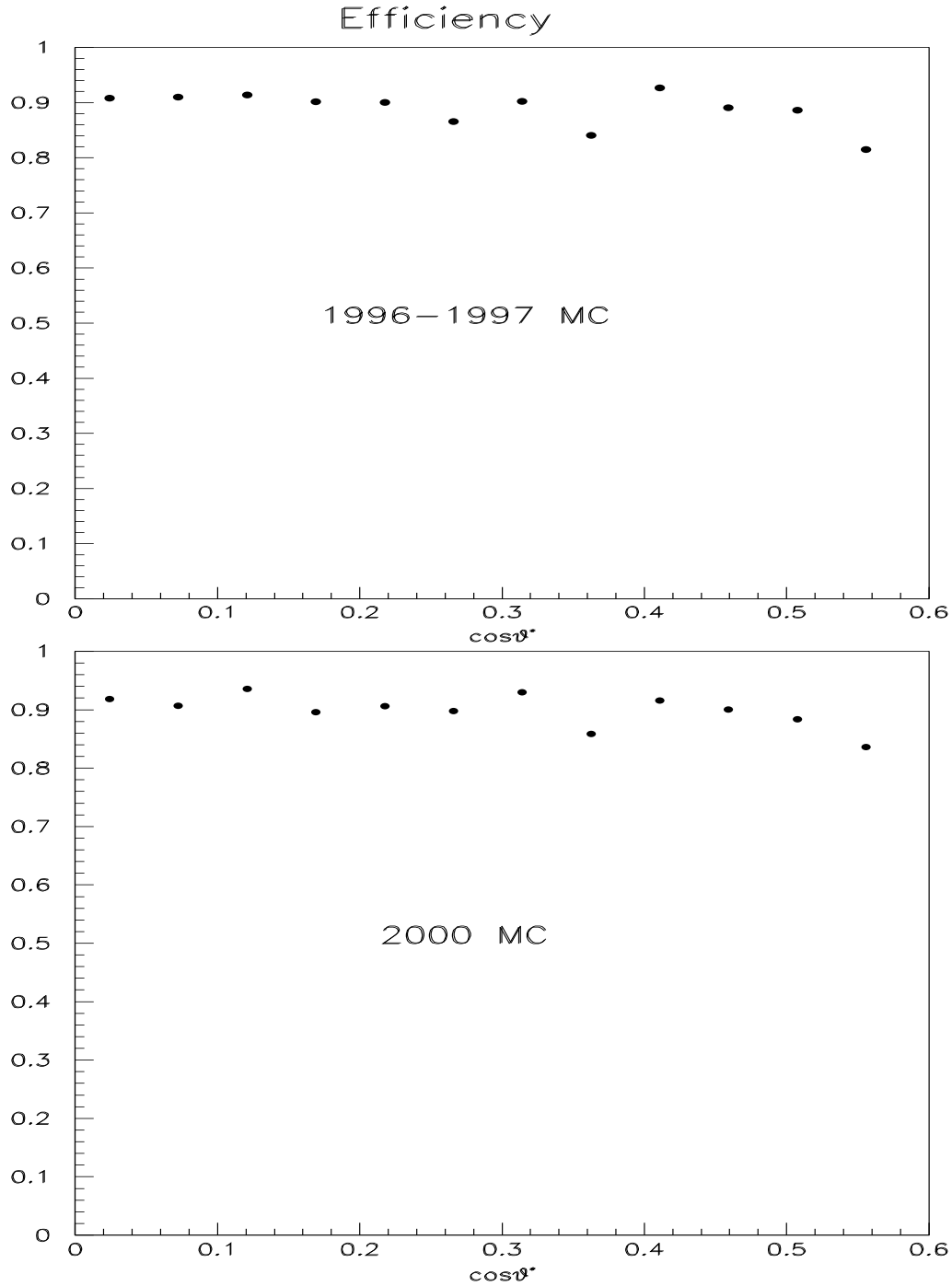


Figure 5.17: Event selection efficiency as a function of  $\cos\theta^*$ . (No dead blocks and # of bins = 12) Note the dip in  $\cos\theta^* = 0.2$  region has disappeared. A total of 100,000  $e^+e^-$  events with  $\lambda = 0$  was generated using the GEANT MC (top: from the 1996-1997 MC, bottom: from the 2000 MC).



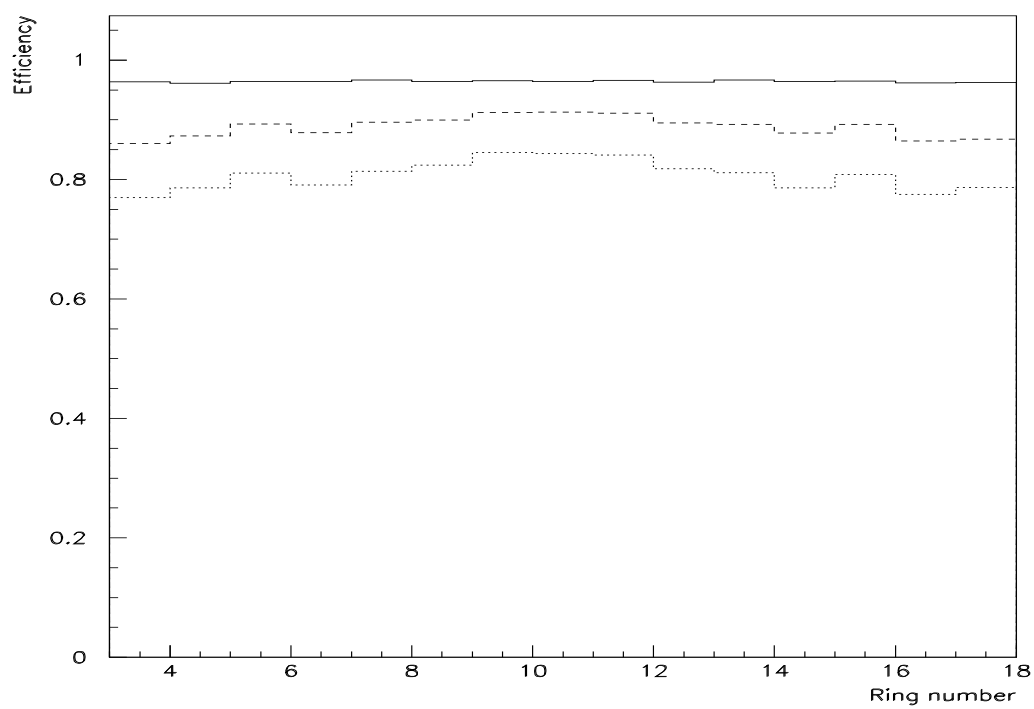


Figure 5.18: Efficiency vs. ring number (two entries per event).

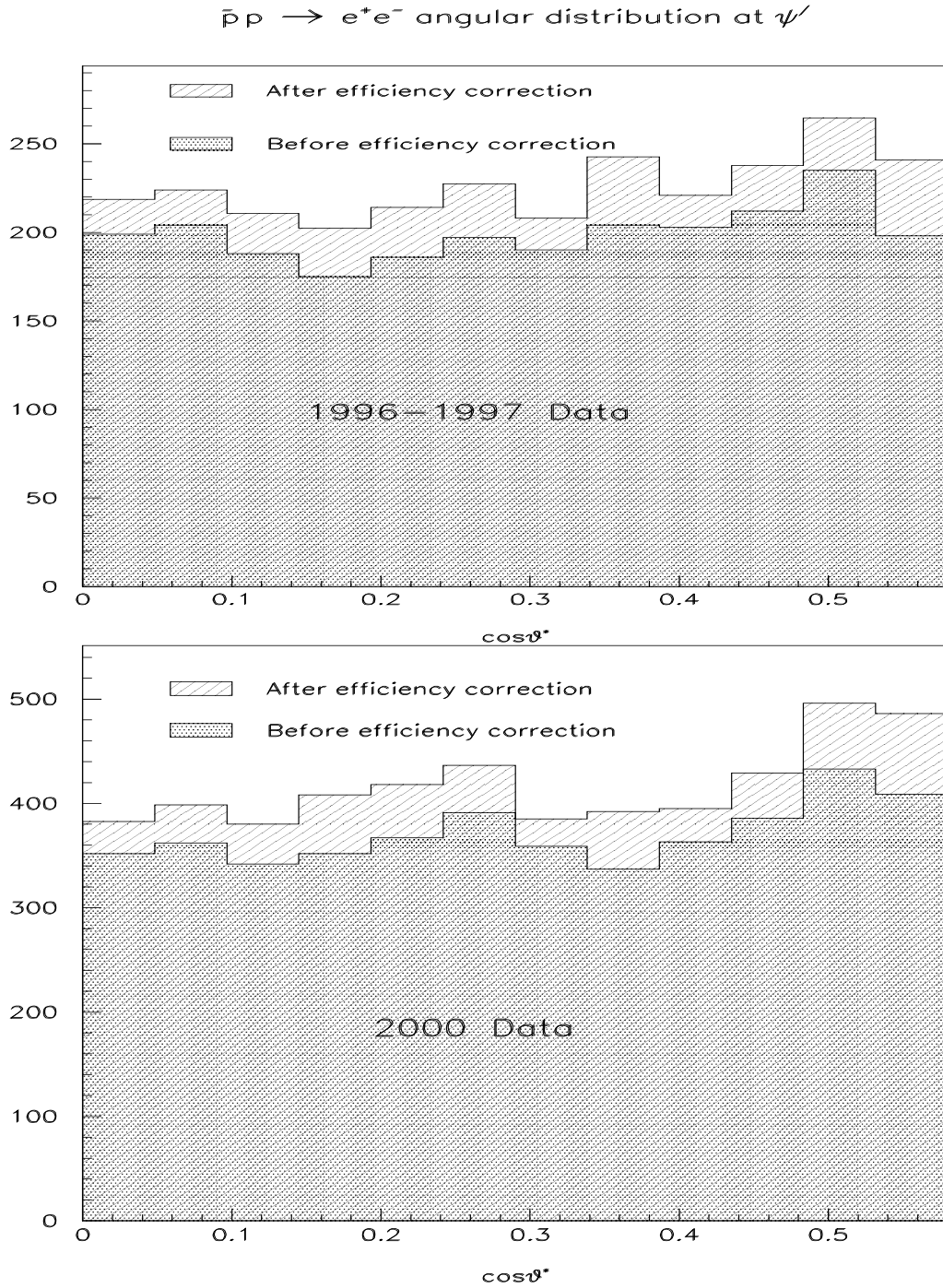


Figure 5.19: Before and after efficiency correction to the finally selected events. (top: the 1996-1997 data, bottom: the 2000 data)

# Chapter 6

## Results and Conclusion

In this Chapter, the results of the measurement of the angular distribution parameter ( $\lambda$ ) are presented. The following sections describe the fitting method, the results from individual and combined data sets, the estimation of systematic errors, and finally, the conclusions.

### 6.1 Fit Method

To extract the angular distribution parameter ( $\lambda$ ), a maximum log-likelihood fit was applied to the selected events after the efficiency correction had been applied. The definition of a log-likelihood function ( $f$ ) is:

$$f = -2\text{Log}(L) = -2\text{Log}\left(\prod_{i=1} L_i\right) = -2 \sum_{i=1} \text{Log}(L_i) \quad (6.1)$$

with

$$L_i = \frac{\varepsilon(\cos\theta_i^*) \times (1 + \lambda \cos^2\theta_i^*)}{\int \varepsilon(\cos\theta') \times (1 + \lambda \cos^2\theta') d\cos\theta'} \quad (6.2)$$

where the index  $i$  runs from 1 to the total number of bins (events) for a binned (unbinned) fit and the  $\varepsilon$  represents the efficiency described in the previous Chapter.

This fit method was applied in two ways: One was a binned fit and the other an unbinned one whose purpose here was to check the consistency in  $\lambda$  by discarding

binning data. For a binned fit, the efficiency correction was performed on a bin-by-bin basis, with a total number of twelve bins, with each bin corresponding to a  $2.08^\circ$  in  $\theta_{lab}$ . (Recall that the angular coverage of an individual CCAL block varied from  $1.52^\circ$  to  $4.80^\circ$ .) The connection between bin size and the angular distribution parameter  $\lambda$  is discussed in a later section. For an unbinned fit, the efficiency correction was applied on an event-by-event basis. The value of the  $\epsilon$  (efficiency) was calculated for 28 different angular ranges using the MC.

To perform a binned fit, the “vector/fit” command in PAW (Physics Analysis Workstation [70]) was used. For the unbinned fit, the CERN program MINUIT<sup>1</sup> [71] was used directly.

## 6.2 Stack-by-stack Results

Using the maximum log-likelihood fit in the range of  $0 < \cos\theta^* < 0.58$ , a value of  $\lambda$  was extracted for each stack of the data. The stack-by-stack measurements of  $\lambda$  from the 1996-1997 data and from the 2000 data, are listed in Table 6.1 and 6.2, respectively. The result of stack 39 (50) in the 1996-1997 (2000) run was unphysical:  $\lambda = 4.69 \pm 5.35$  and  $2.05 \pm 0.75$ , respectively due to lack of statistics for the former and relative badness of the data for the latter, which will be described more later.

The average  $\lambda$  value from each stack ( $\langle \lambda \rangle_{stk}$ ) was obtained by weighting the number of events in that stack:

$$\langle \lambda \rangle_{stk} \equiv \frac{\sum_i N_i \lambda_i}{\sum_i N_i} \quad (6.3)$$

where index  $i$  runs from 1 to the total number of stacks.

In this way, the average binned fit values were obtained as  $\langle \lambda \rangle_{stk} = 0.47^{+0.26}_{-0.22}$  and  $\langle \lambda \rangle_{stk} = 0.59^{+0.20}_{-0.18}$  from the 1996-1997 data and from the 2000 data, respectively. These two values are consistent within their errors. The average of the unbinned fit values from each stack was obtained as  $\langle \lambda \rangle_{stk} = 0.50^{+0.25}_{-0.22}$  and  $\langle \lambda \rangle_{stk}$

---

<sup>1</sup>MINUIT is a CERN program for function minimization and error analysis.

Stack #	# of events	Lum. ( $nb^{-1}$ )	$E_{cm}$ (MeV)	Binned Fit	Unbinned Fit
2	312	1086.22	3685.58 $\sim 3686.02$	$0.24^{+0.69}_{-0.60}$	$0.16^{+0.62}_{-0.54}$
6	310	1435.58	3686.15	$0.54^{+0.72}_{-0.62}$	$0.42^{+0.68}_{-0.58}$
7	290	1085.27	3685.9	$0.54^{+0.75}_{-0.65}$	$0.55^{+0.71}_{-0.61}$
8	306	1127.08	3686.2	$-0.14^{+0.61}_{-0.54}$	$-0.12^{+0.60}_{-0.52}$
17	327	1306.72	3686.16	$0.49^{+0.68}_{-0.60}$	$0.84^{+0.75}_{-0.64}$
39	60	796.10	3686.40 $\sim 3686.95$	$4.69^{+5.35}_{-3.01}$	$3.30^{+2.86}_{-1.97}$
40	483	1458.83	3686.00 $\sim 3686.02$	$0.71^{+0.57}_{-0.51}$	$0.73^{+0.59}_{-0.52}$
67	303	240.06	3685.0 $\sim 3687.0$	$1.00^{+0.82}_{-0.70}$	$1.20^{+0.83}_{-0.70}$
Total	2391	10121.01	$\langle \lambda \rangle_{stk} =$	$0.47^{+0.26}_{-0.22}$	$0.50^{+0.25}_{-0.22}$

Table 6.1: Stack-by-stack results and their average (last row) from the 1996-1997 data.

Stack #	# of events	Lum. ( $nb^{-1}$ )	$E_{cm}$ (MeV)	Binned Fit	Unbinned Fit
1	148	747.722	3685.2 $\sim 3687.6$	$0.32^{+1.02}_{-0.84}$	$0.15^{+0.96}_{-0.77}$
2	563	1008.169	3686.0	$0.27^{+0.49}_{-0.45}$	$0.38^{+0.49}_{-0.44}$
14	337	991.877	3686.0	$1.02^{+0.78}_{-0.67}$	$1.09^{+0.75}_{-0.64}$
29	263	991.911	3684.5 $\sim 3686.5$	$0.26^{+0.75}_{-0.64}$	$0.12^{+0.70}_{-0.59}$
30	136	396.250	3686.0 $\sim 3687.5$	$-0.57^{+0.92}_{-0.76}$	$0.21^{+0.95}_{-0.76}$
49	814	2566.442	3686.0	$1.35^{+0.53}_{-0.48}$	$1.25^{+0.49}_{-0.44}$
50	546	1275.000	3686.0	$2.05^{+0.75}_{-0.66}$	$2.00^{+0.69}_{-0.61}$
51	668	2103.259	3686.0	$0.55^{+0.48}_{-0.44}$	$0.55^{+0.47}_{-0.43}$
54	978	2400.949	3686.0	$0.18^{+0.37}_{-0.34}$	$0.20^{+0.35}_{-0.32}$
Total	4453	12481.58	$\langle \lambda \rangle_{stk} =$	$0.59^{+0.20}_{-0.18}$	$0.65^{+0.19}_{-0.17}$

Table 6.2: Stack-by-stack results and their average (last row) from the 2000 data.

$= 0.65^{+0.19}_{-0.17}$  from the 1996-1997 data and from the 2000 data, respectively. All these results are self-consistent within their errors.

Since data from each stack were taken at different times, it was necessary and prudent to check their consistency: A Kolmogorov-Smirnov (K-S) test which in widely is used for quality control without introducing systematic effects (see Appendix D), was performed for this purpose,. The K-S test is independent of the distribution function of data, and thus the result does not give any information as to which data set is measured better than any other. However, if the probability of consistency is high, then different data sets can be combined together with confidence to reduce statistical error.

Tables 6.3 and 6.4 list the results of this test for the 1996-1997 and for the 2000 data, respectively. The last row is the test result between a given stack and the rest of the stacks. Stack 8 in the 1996-1997 run showed the least consistency (12.9%) with the rest, with a  $\lambda$  value ( $-0.14 \pm 0.61$ ) that was within the physical range ( $-1 < \lambda < +1$ ), while stack 39 which had an unphysical  $\lambda$  value ( $4.69 \pm 5.35$ ), showed the second least consistency (37.2%). In the 2000 run, stack 50 had the least consistency (3.3%), which is very low, while also yielding an unphysical  $\lambda$  value ( $2.05 \pm 0.75$ ). While the K-S test taken by itself does not allow a judgement on the relative quality of data sets, it's interesting that those data sets which are least consistent with the others, also yield unphysical values of  $\lambda$ . In Figure 6.1 is shown the probability distribution of the K-S test between each stack from the 1996-1997 run and from the 2000 run. The probability distribution was flat, which implies that all stacks may be used for the data analysis. As is shown in Figure 6.2, the K-S probability had no relation with  $\lambda$ .

Stack #	2	6	7	8	17	39	40	67
2	1.000	0.900	0.779	0.838	0.473	0.338	0.498	0.256
6	0.900	1.000	0.908	0.653	0.721	0.477	0.601	0.797
7	0.779	0.908	1.000	0.559	0.703	0.410	0.754	0.417
8	0.838	0.653	0.559	1.000	0.061	0.186	0.307	0.239
17	0.473	0.721	0.703	0.061	1.000	0.307	0.840	0.821
39	0.338	0.477	0.410	0.186	0.307	1.000	0.412	0.494
40	0.498	0.601	0.754	0.307	0.840	0.412	1.000	0.753
67	0.256	0.797	0.417	0.239	0.821	0.494	0.753	1.000
a stack vs. the rest of stacks	0.507	0.813	0.683	0.129	0.407	0.372	0.888	0.440

Table 6.3: The K-S test results between each stack from the 1996-1997 run. The last row is the test result between a given stack and the rest of the stacks.

Stack #	1	2	14	29	30	49	50	51	54
1	1.000	0.983	0.617	0.988	0.684	0.709	0.513	0.795	0.970
2	0.983	1.000	0.592	0.963	0.626	0.485	0.112	0.811	0.940
14	0.617	0.592	1.000	0.444	0.587	0.856	0.303	0.692	0.563
29	0.988	0.963	0.444	1.000	0.649	0.431	0.100	0.615	0.945
30	0.684	0.626	0.587	0.649	1.000	0.482	0.186	0.724	0.719
49	0.709	0.485	0.856	0.431	0.482	1.000	0.434	0.506	0.188
50	0.513	0.112	0.303	0.100	0.186	0.434	1.000	0.122	0.023
51	0.795	0.811	0.692	0.615	0.724	0.506	0.122	1.000	0.539
54	0.970	0.940	0.563	0.945	0.719	0.188	0.023	0.539	1.000
a stack vs. the rest of stacks	0.889	0.874	0.753	0.753	0.741	0.380	0.033	0.816	0.252

Table 6.4: The K-S test results between each stack from the 2000 run. The last row is the test result between a given stack and the rest of the stacks.



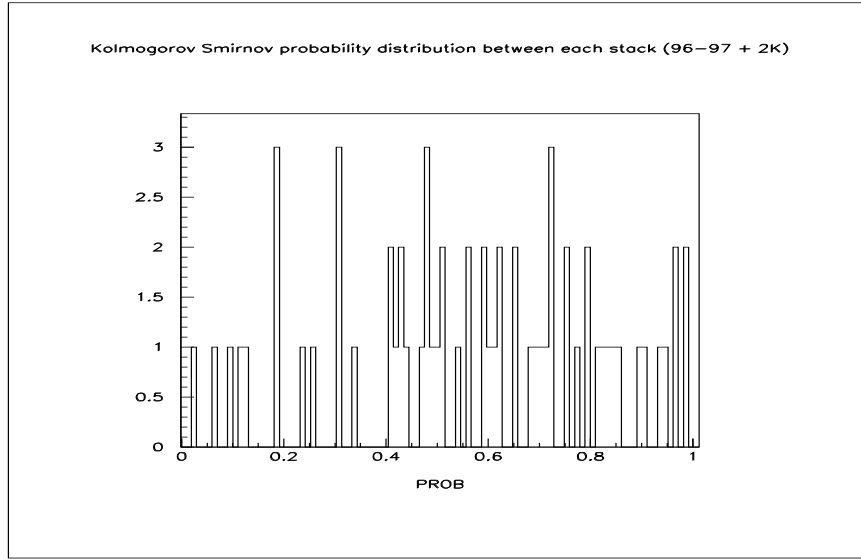


Figure 6.1: The K-S probability distribution between each stack from the 1996-1997 run and the 2000 run.

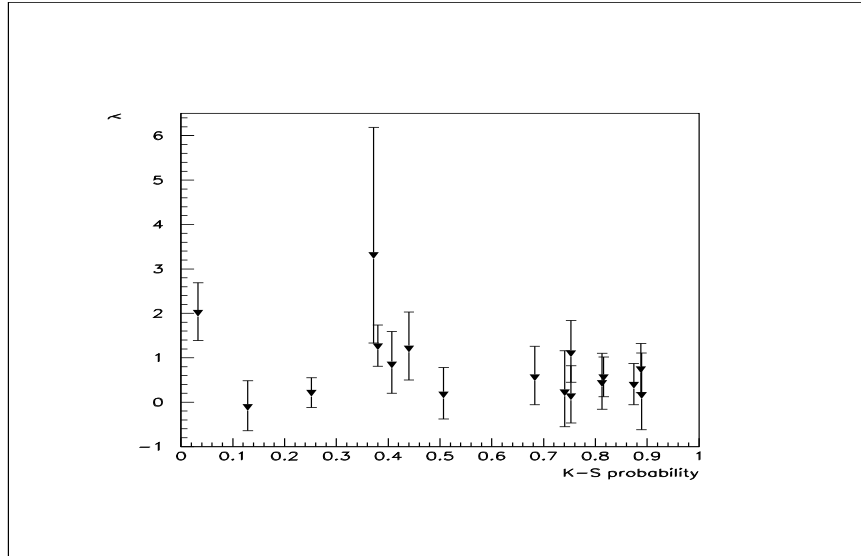


Figure 6.2:  $\lambda$  from each stack vs. the K-S probability between a stack and the rest of the stacks for both the 1996-1997 and the 2000 data sets. No particular relation exists between  $\lambda$  and the K-S probability.

### 6.3 Results from Full Data Set

Since the probability distribution of the K-S test results was flat, all stacks were included to obtain a single result from the full data set. The values of  $\lambda$  that were given by the maximum likelihood fit to the full data sets of the 1996-1997 run and the 2000 run are listed in Table 6.5. Figures 6.3 and 6.4 show the angular distributions of events in each of the full data sets (The line drawn in the figure is a fit to the data).

To study whether the choice of a particular bin size affects the value of  $\lambda$ , fit values were obtained for several different bin sizes. Figure 6.5 shows the values of  $\lambda$  as a function of the bin size (the 2000 data were used in this plot) and from this distribution it is concluded that the value of  $\lambda$  is not affected by the choice of bin size around the value used in this analysis.

### 6.4 Results from Combined Data Sets

To check consistency between the two full data sets from the 1996-1997 and 2000 runs, a second K-S test was performed, with the result that the probability of consistency was 74.4%. This high probability was expected since the  $\lambda$  values from the two different data-taking periods were consistent as described in the previous section. Therefore this result provided a sufficient reason to combine the two data sets in order to reduce statistical error.

The value of  $\lambda$  obtained with the maximum log-likelihood method was:

$$\lambda = 0.67_{-0.14}^{+0.15} \quad (stat.) \quad (6.4)$$

Figure 6.6 shows the angular distribution from the combined data (filled circles). Open circles in Figure 6.6 represent MC  $e^+e^-$  events generated with  $\lambda = 0.67$  at the  $\psi'$ . The total number of MC events used in the Figure 6.6 is approximately 6.7 times (45531) that of the total number of combined data (6844).

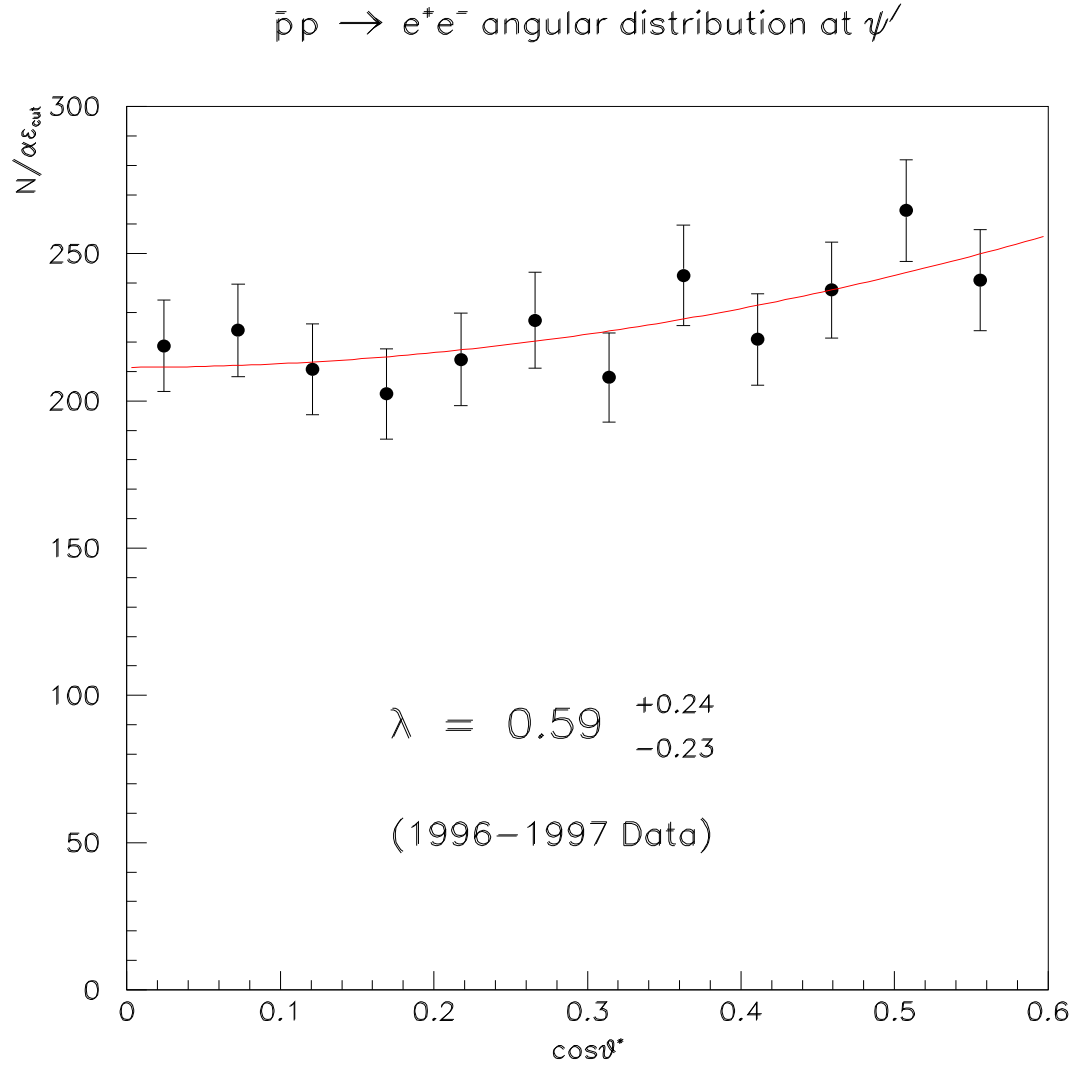


Figure 6.3: The angular distribution of  $\bar{p}p \rightarrow e^+e^-$  at the  $\psi'$  from the 1996-1997 data and its likelihood fit (line).

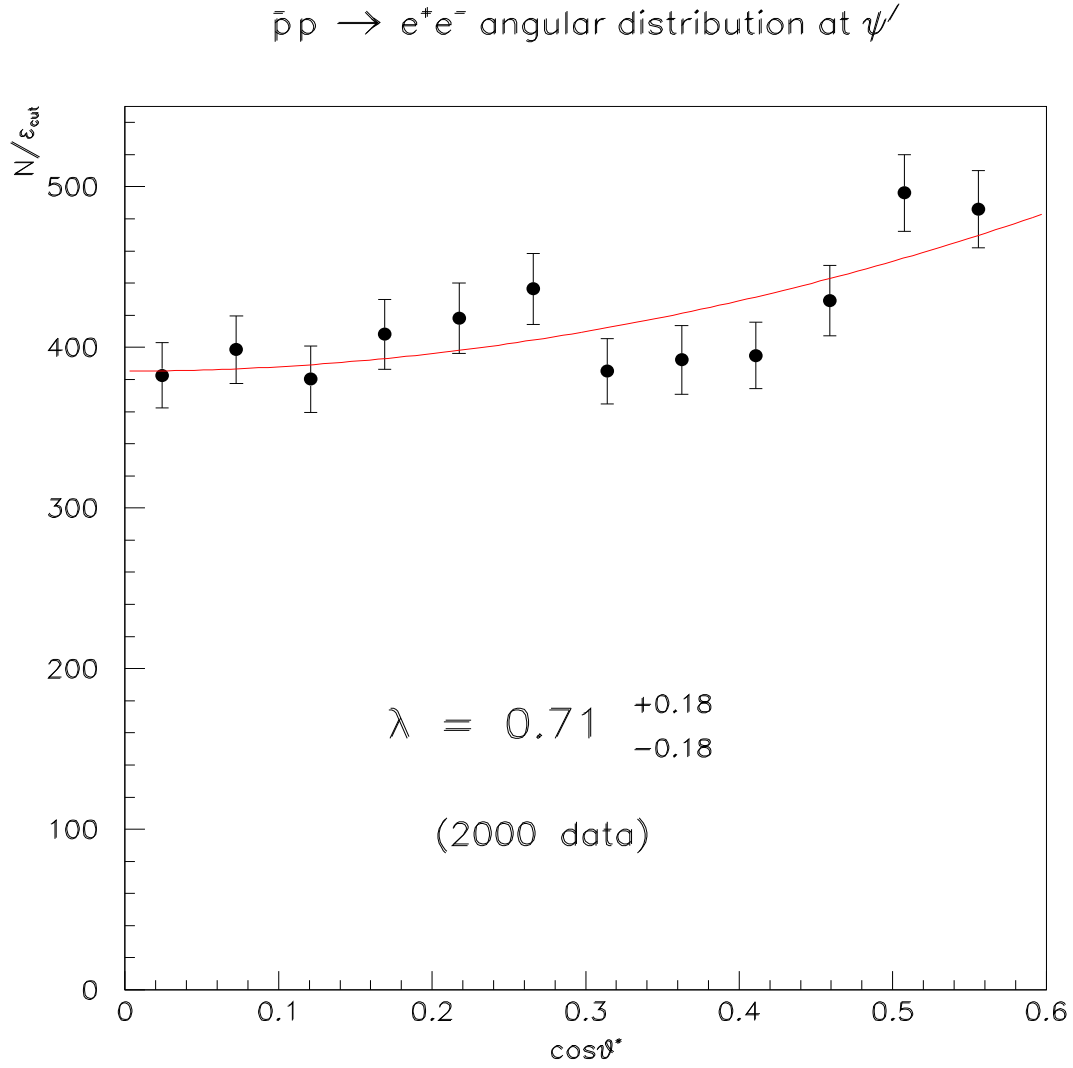


Figure 6.4: The angular distribution of  $\bar{p}p \rightarrow e^+e^-$  at the  $\psi'$  from the 2000 data and its likelihood fit (line).

Data		1996-1997	2000
	Luminosity	$10.09 \text{ pb}^{-1}$	$12.48 \text{ pb}^{-1}$
	Total # of events after cuts	2579	4822
	Total # of events used for fit ( $0 < \cos\theta^* < 0.58$ )	2391	4453
Fitted	Binned	$0.59^{+0.24}_{-0.23}$	$0.71 \pm 0.18$
$\lambda$	Unbinned	$0.59^{+0.24}_{-0.23}$	$0.72^{+0.18}_{-0.17}$

Table 6.5: The comparison of the results from the two data sets. The values of  $\lambda$  from the two data set are consistent.

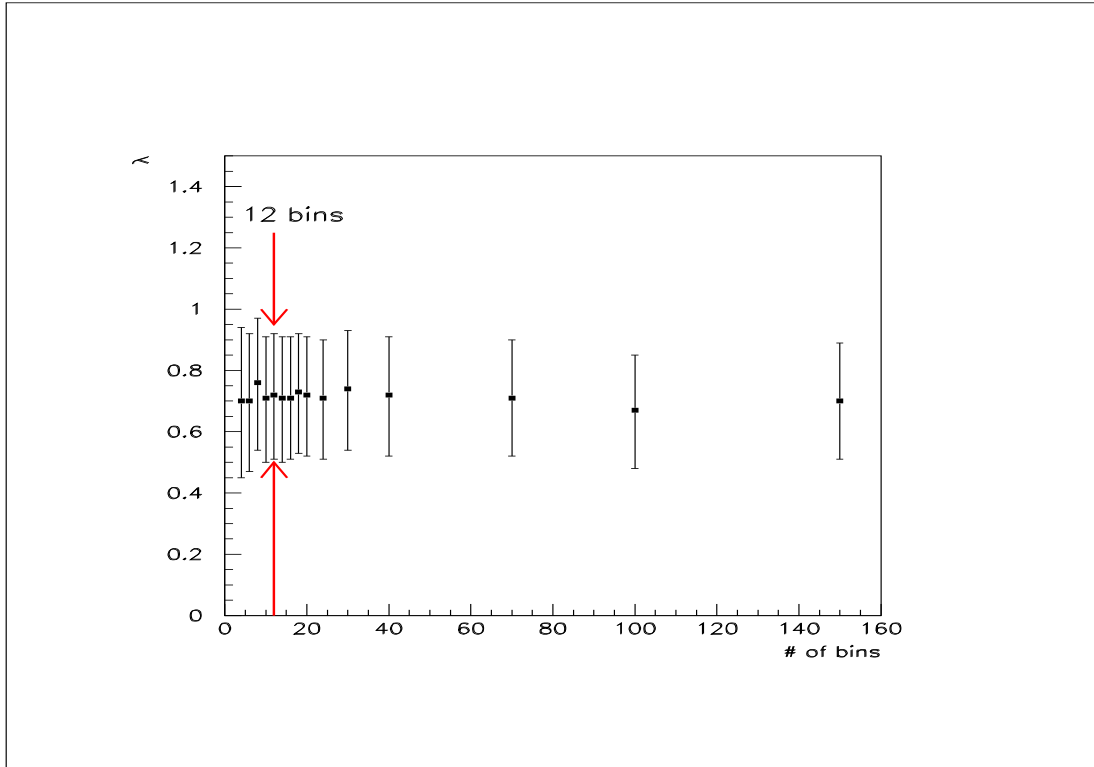


Figure 6.5: Fitted  $\lambda$  (2000 data) vs. # of bins. Note that the # of bins does not affect for measuring  $\lambda$ .

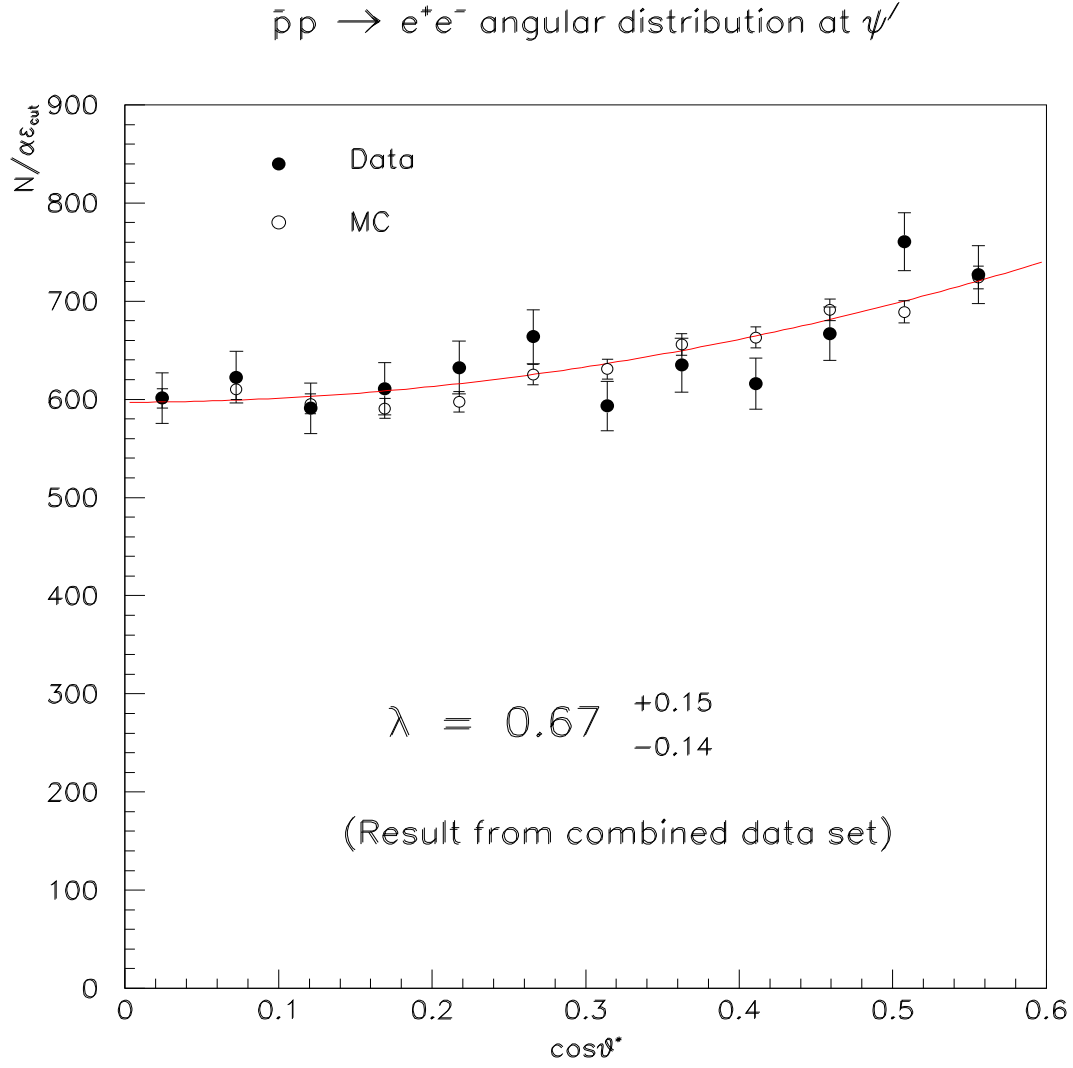


Figure 6.6: The angular distribution of  $\bar{p}p \rightarrow e^+e^-$  at the  $\psi'$  from the combined data (filled circles). The fit result (line) is  $\lambda = 0.67^{+0.15}_{-0.14}$  (stat.) Open circles represents MC events generated with  $\lambda = 0.67$ .

## 6.5 Systematic Error

To obtain the systematic error that source of error which is caused by a lack of a complete understanding of the detector, rather than statistical fluctuation, a study of the effect of modifying the analysis parameters was performed.

The systematic error in our angular distribution measurement was obtained by studying how the value of  $\lambda$  was affected by different values of the seed/cluster threshold and the analysis cuts.

To measure the variation due to the seed/cluster threshold, two new values of  $\lambda$  ( $\lambda_{\pm 10\%}$ ) were obtained by changing the value of seed/cluster threshold by  $\pm 10\%$ . A similar method was applied to measure the variation due to other analysis cuts. To extract the value of  $\lambda_{\pm 10\%}$ , the same (maximum log-likelihood) fit was applied to the data selected by changing the seed/cluster threshold or cuts by  $\pm 10\%$  after applying an efficiency correction. The applied efficiency was likewise obtained by applying the same  $\pm 10\%$  variation of the seed/cluster threshold or selection criteria. The variation due to this change was then obtained for each side of the 10% variation, which was parameterized as:

$$\left( \frac{\Delta \lambda_{\pm 10\%}}{\lambda_{fit}} \right)_i \equiv \left( \frac{\lambda_{\pm 10\%} - \lambda_{fit}}{\lambda_{fit}} \right)_i \quad (6.5)$$

where the index  $i$  runs from 1 to the total number of criteria (including the seed/cluster threshold) and the  $\lambda_{fit}$  is the fitted  $\lambda$  value obtained from the previous section.

The sensitivity to the cluster mass cut ( $< 0.12$  GeV) was examined by changing it to 0.13 GeV and 0.11 GeV. To study the sensitivity for the  $m_{ee}$  cut ( $> 3.4$  GeV), it was reduced to 3.34 GeV and increased to 3.46 GeV corresponding to approximately  $1 \sigma$  variation of the CCAL resolution which is 65 MeV assuming symmetric decay of  $\psi'$  to  $e^+e^-$ . The systematic error of each cut (including the seed/cluster threshold) was obtained by averaging arithmetically the two values from each variation in Eq. (6.5):

$$\sigma_i = \left( \frac{\left| \frac{\Delta\lambda_{+10\%}}{\lambda_{fit}} \right|_i + \left| \frac{\Delta\lambda_{-10\%}}{\lambda_{fit}} \right|_i}{2} \right) \cdot \lambda_{fit} \quad (6.6)$$

Finally, the total systematic error was obtained in the following way, which is exactly true if there is no correlation between the individual errors:

$$\sigma_{tot} = \sqrt{\sum_i \sigma_i^2} \quad (6.7)$$

In Table 6.6 is listed the estimated systematic errors from each cut (including the seed/cluster threshold) used for the event selection in the 1996-1997 data and in the 2000 data. The total systematic error was listed in the last row of the Table 6.6. They are 0.05 and 0.04 for the 1996-1997 data and the 2000 data, respectively. The cut which had the most effect on the total systematic error was that on the invariant mass of the two electrons ( $m_{ee} > 3.4$  GeV).

The total systematic error of the combined data set was obtained as 0.04 by averaging the total systematic errors from the two data sets by giving weight on their number of events in the following way:

$$\sigma_{combined} = \sigma_{'96-'97} \left( \frac{N_{'96-'97}}{N_{tot}} \right) + \sigma_{2000} \left( \frac{N_{2000}}{N_{tot}} \right). \quad (6.8)$$

## 6.6 Conclusions

The angular distribution of the process  $\bar{p}p \rightarrow e^+e^-$  has been measured using two data sets from different data-taking periods with a total of  $22.57 \text{ pb}^{-1}$  of integrated luminosity. These data resulted in 6844 events in the  $0 < \cos\theta^* < 0.58$  region after event selection. The background due to mis-identified  $e^+e^-$  events not from the  $\psi' \rightarrow e^+e^-$  decay was studied using the GEANT MC for cascade decay channels



Description of cuts	Cuts	Systematic error	
		1996-1997	2000
Seed/cluster threshold	50/50 MeV	0.01	0.01
Invariant mass (main & its additional clsters)	$< 0.2$ GeV	0.0	0.01
Probability (4C fit)	$> 10^{-4}$	0.01	0.0
EW for the highest invariant mass pair	$> 10^{-4}$	0.0	0.0
cluster mass for each of the highest invariant mass pair	$< 0.12$ GeV	0.02	0.0
$m_{ee}$	$> 3.4$ GeV	0.04	0.04
Total systematic error		0.05	0.04

Table 6.6: The systematic errors from each cut and the final systematic error (last row).

of the  $\psi'$ :  $J/\psi \eta$  and  $J/\psi \pi\pi$ . The level of this background was shown to be negligible (less than 0.2%) and thus no background subtraction was required. The magnitude of possible non-resonant contribution to the data was studied using data off-resonance and was also found to be negligible.

Finally, the detector efficiency was determined with a MC program based on GEANT and applied to the data analysis.

Both a binned and an unbinned fit using a maximum log-likelihood fit were performed on the data to extract a value for  $\lambda$ . The two fit results were consistent within errors. The bin size ( $\Delta\theta_{lab} = 2.08^\circ$ ) was selected to be within the range of a block size of CCAL even though it turned out to be that the final value of  $\lambda$  was not sensitive to the bin size. The binned fit results for the angular distribution parameter  $\lambda$  were:

$$\lambda_{\psi'} = 0.67^{+0.15}_{-0.14} \text{ (stat.)} \pm 0.04 \text{ (sys.)}.$$

The above systematic errors were obtained by varying each cut value (including seed/cluster threshold) by  $\pm 10\%$ .

Using this value of  $\lambda$ , the ratio of the helicity amplitudes can be extracted:

$$\left| \frac{C_0}{C_1} \right|_{\psi'} = \sqrt{\frac{1-\lambda}{1+\lambda}} = 0.44^{+0.12}_{-0.11}.$$

This is simply related to the ratio of the Sachs form factors of the proton at the  $\psi'$ ,

$$\left| \frac{G_E}{G_M} \right|_{\psi'} = \frac{E_{cm}}{2M_p} \sqrt{\frac{1-\lambda}{1+\lambda}} = 0.87^{+0.25}_{-0.24}.$$

So far, no measurements of  $\left| \frac{G_E}{G_M} \right|$  in the time-like region have been made off-resonance. In the space-like region,  $\left| \frac{G_E}{G_M} \right| \simeq 0.36$  at any  $Q^2$  studied so far if the Rosenbluth method is right, while  $\left| \frac{G_E}{G_M} \right| \simeq 0.11$  at  $Q^2 = 5.6 \text{ GeV}^2$  and it is expected that  $\left| \frac{G_E}{G_M} \right|$  continues to decrease if on the contrary the polarization method is correct.

The absolute value of  $|G_E|$  and  $|G_M|$  of the proton at the  $\psi'$  was estimated using the  $\left| \frac{G_E}{G_M} \right|$  measurement, Eq. (24) in Chapter 1 and the Breit-Wigner resonance cross-section formula [72]  $\sigma_{BW}(\bar{p}p \rightarrow \psi' \rightarrow e^+e^-)$ . The PDG values [73] were used for the calculation of the  $\sigma_{BW}(\bar{p}p \rightarrow \psi' \rightarrow e^+e^-)$ . This method resulted in the following estimate of the absolute value of  $|G_M|$  and  $|G_E|$  of the proton at the  $\psi'$  as:

$$|G_M|_{\psi'} = 0.520 \pm 0.013, \quad |G_E|_{\psi'} = 0.452^{+0.118}_{-0.113}.$$

The  $|G_M|$  value at the  $\psi'$  is at the same level of that at the threshold. (See Figure 8 in Chapter 1.) Our measurement could be used for fitting data in both space-like and time-like regions using Vector Dominance (VD) model where several iso-vector and iso-scalar vector mesons ( $\rho$ ,  $\rho'$ ,  $\omega$ ,  $\phi$ ,  $J/\psi$ ,  $\psi'$ , ...) are taken into account.

Using the world-average of  $\lambda$  at the  $J/\psi$  ( $\lambda_{J/\psi} = 0.63 \pm 0.08$ ) [74], the ratio of the helicity amplitudes turns out to be:

$$\left| \frac{C_0}{C_1} \right|_{J/\psi} = \sqrt{\frac{1-\lambda}{1+\lambda}} = 0.48 \pm 0.06 .$$

Using the same  $\lambda_{J/\psi}$ , the ratio of the Sachs form factors of the proton at the  $J/\psi$  is:

$$\left| \frac{G_E}{G_M} \right|_{J/\psi} = \frac{E_{cm}}{2M_p} \sqrt{\frac{1-\lambda}{1+\lambda}} = 0.86 \pm 0.10 .$$

The absolute values of  $|G_M|$  and  $|G_E|$  of the proton at the  $J/\psi$  can then be calculated using the  $\left| \frac{G_E}{G_M} \right|_{J/\psi}$  measurement, Eq (24) in Chapter 1 and  $\sigma_{BW}$  ( $\bar{p}p \rightarrow J/\psi \rightarrow e^+e^-$ ) of PDG [73] values, which are:

$$|G_M|_{J/\psi} = 4.822 \pm 0.067, \quad |G_E|_{J/\psi} = 4.147 \pm 0.427 .$$

Note that the values of  $|G_M|$  and  $|G_E|$  at the  $J/\psi$  are larger (about 10 times) than those at the  $\psi'$ . This is perhaps to be expected, on very general grounds: The  $\psi'$  is the first radial excitation with the same quantum number ( $J^{pc} = 1^{--}$ ) as the  $J/\psi$ , and both  $J/\psi$  and  $\psi'$  decay into light quark states (such as a  $\bar{p}p$  pair) via three gluon annihilation. Since more energy and more final states are available at the  $\psi'$ , it is natural to expect a suppression in the coupling strength to any particular final state relative to the  $J/\psi$ .

There are few theoretical predictions of  $\lambda$  at the  $J/\psi$  and  $\psi'$  (see Table 6.7). According to the prediction by Claudson et al. [75], the value of  $\lambda$  is 0.59 (0.46) at the  $\psi'$  ( $J/\psi$ ). In Carimalo's prediction [76], the value of  $\lambda$  is 0.80 (0.69) at the  $\psi'$  ( $J/\psi$ ). Our measurement of  $\lambda$  at the  $\psi'$  did not show any preference between the two theoretical predictions because the statistical error in the measurement was larger than that of the difference between the two predictions. However, the world average value of  $\lambda$  at the  $J/\psi$  preferred Carimalo's prediction. Table 6.8 lists the extracted values of  $\left| \frac{G_E}{G_M} \right|$  and  $\left| \frac{C_0}{C_1} \right|$  using the measured/predicted  $\lambda$  (from Table 6.7) at the  $J/\psi$  and  $\psi'$ . Note that the extracted values of  $\left| \frac{C_0}{C_1} \right|$  and  $\left| \frac{G_E}{G_M} \right|$  at the  $J/\psi$  and  $\psi'$  are the same within errors.

In Figure 6.7, all of the measurements of  $\lambda$  and the theoretical predictions at the  $J/\psi$  and  $\psi'$  are displayed. There has been, as yet, no other measurement of  $\lambda$  at the  $\psi'$  energy.

	Reference	$\lambda_{J/\psi}$	$\lambda_{\psi'}$
Experiments	Mark I	$1.45 \pm 0.56$	—
	DASP	$1.70 \pm 1.70$	—
	Mark II	$0.61 \pm 0.23$	—
	DM2	$0.62 \pm 0.11$	—
	Mark III	$0.58 \pm 0.14$	—
	E835 ( '96-'97+2000)	—	$0.67^{+0.15}_{-0.14}$
	World average	$0.63 \pm 0.08$	$0.67^{+0.15}_{-0.14}$
Theory	Claudson et al.	0.46	0.59
	Carimalo	0.69	0.80

Table 6.7: The experimental measurements and the theoretical predictions on  $\lambda$  at the  $J/\psi$  and  $\psi'$ .

	Reference	$\left  \frac{G_E}{G_M} \right _{J/\psi}$	$\left  \frac{C_0}{C_1} \right _{J/\psi}$	$\left  \frac{G_E}{G_M} \right _{\psi'}$	$\left  \frac{C_0}{C_1} \right _{\psi'}$
Experiments	Mark I	Unphysical	Unphysical	—	—
	DASP	Unphysical	Unphysical	—	—
	Mark II	$0.88 \pm 0.30$	$0.49 \pm 0.18$	—	—
	DM2	$0.80 \pm 0.15$	$0.48 \pm 0.09$	—	—
	Mark III	$0.90 \pm 0.18$	$0.52 \pm 0.11$	—	—
	E835 ( '96-'97+2000)	—	—	$0.87^{+0.25}_{-0.24}$	$0.44^{+0.12}_{-0.11}$
	World average	$0.86 \pm 0.10$	$0.48 \pm 0.06$	$0.87^{+0.25}_{-0.24}$	$0.44^{+0.12}_{-0.11}$
Theory	Claudson et al.	1.0 (input)	0.61	1.0 (input)	0.51
	Carimalo	0.69	0.42	0.65	0.33

Table 6.8: Extracted values of  $\left| \frac{G_E}{G_M} \right|$  and  $\left| \frac{C_0}{C_1} \right|$  using the measured/predicted  $\lambda$  at the  $J/\psi$  and  $\psi'$  from Table 6.7.

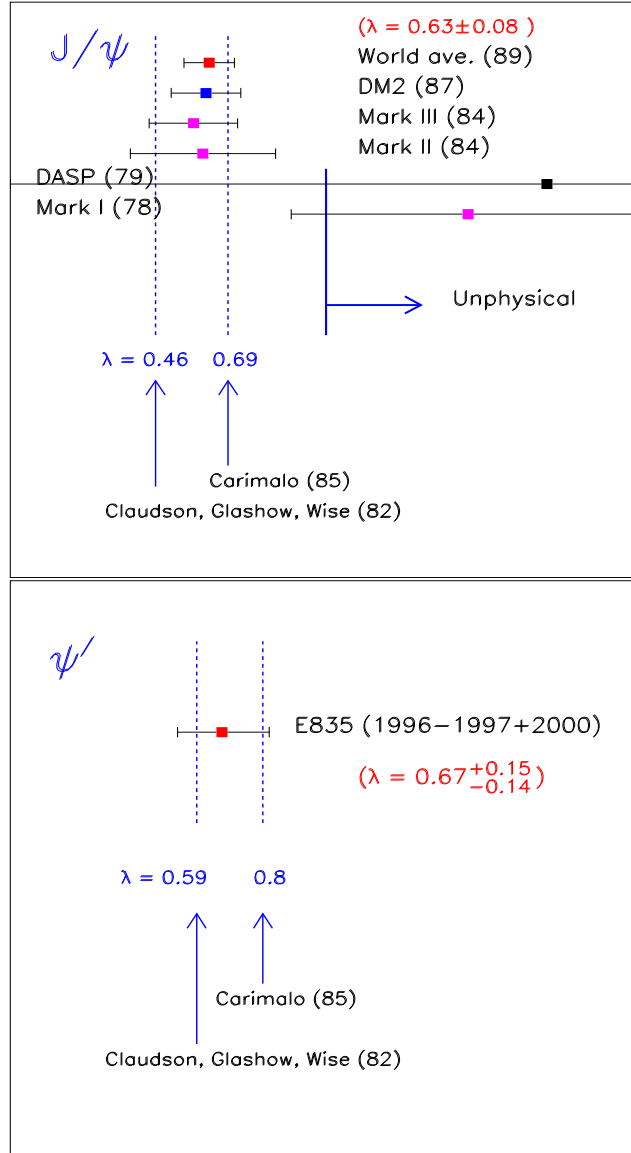


Figure 6.7: All the measurements and the theoretical predictions of  $\lambda$  at the  $J/\psi$  (top) and  $\psi'$  (bottom).

# Appendix A

## Form factors and the angular distribution for the process $\bar{p}p \rightarrow e^+e^-$

The angular distribution of the process <sup>1</sup>  $\bar{p}p \rightarrow e^+e^-$  in the CM system can be obtained by calculating

$$\frac{dN}{d\cos\theta} \propto \overline{|\mathcal{M}|^2} \quad (\text{A.1})$$

where  $\mathcal{M}$  is the invariant amplitude of the process as written in Chapter 1:

$$\begin{aligned} \mathcal{M} &\sim \langle 0 | J^\mu | \bar{p}p \rangle \cdot \frac{1}{q^2} \cdot \langle e^+e^- | j_\mu | 0 \rangle \\ &= \frac{4\pi\alpha}{q^2} \bar{v}(\vec{p}', \bar{\lambda}_p) \Gamma^\mu u(\vec{p}, \lambda_p) \cdot \bar{u}(\vec{k}, \lambda_e) \gamma_\mu v(\vec{k}', \bar{\lambda}_e). \end{aligned} \quad (\text{A.2})$$

Let's rewrite Eq. (A.2) in the CM system of  $\bar{p}p$  (see Figure A.1).

---

<sup>1</sup>This Appendix should be read in conjunction with Chapter 1.

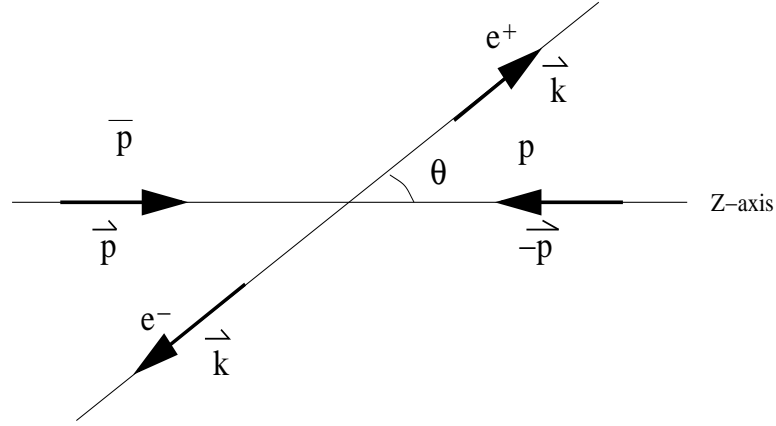


Figure A.1:  $\bar{p}p \rightarrow e^+e^-$  in the CM system.

$$\mathcal{M} = \frac{4\pi\alpha}{q^2} \bar{v}(p\hat{z}, \bar{\lambda}_p) \Gamma^\mu u(-p\hat{z}, \lambda_p) \times \bar{u}(-\vec{k}, \lambda_e) \gamma_\mu v(\vec{k}, \bar{\lambda}_e) \quad (\text{A.3})$$

where  $\Gamma^\mu$  was obtained in Chapter 1 as:

$$\Gamma^\mu = \gamma^\mu (F_1(Q^2) + F_2(Q^2)) + \frac{(p' - p)^\mu}{2M} F_2(Q^2) \quad (\text{A.4})$$

with

$$\frac{(p' - p)^\mu}{2M_p} = \left( 0, 0, 0, \frac{|\vec{p}|}{M_p} \right) \quad (\text{A.5})$$

in the CM frame.

Now let's turn to the spinors in Eq. (A.3). A spinor,  $u(\vec{p}, \lambda)$ , satisfying the Dirac equation is expressed in the following way:

$$u(\vec{p}, \lambda) = \begin{pmatrix} f_+ \chi_\lambda(\hat{p}) \\ f_- (2\lambda) \chi_\lambda(\hat{p}) \end{pmatrix} \quad (\text{A.6})$$

where  $\chi_\lambda(\hat{p})$  is a two-component spinor normalized to  $\chi_{\lambda'}^\dagger(\hat{p}) \chi_\lambda(\hat{p}) = \delta_{\lambda'\lambda}$  which satisfies  $\vec{\sigma} \cdot \hat{p} \chi_\lambda(\hat{p}) = 2\lambda \chi_\lambda(\hat{p})$  with  $\lambda \equiv \text{helicity} = \pm \frac{1}{2}$ , and  $f_\pm$  is defined as

$$f_{\pm} \equiv \sqrt{\frac{E_p \pm M_p}{2M_p}}. \quad (\text{A.7})$$

The spinor  $u(-\vec{p}, \lambda)$  is obtained from  $u(\vec{p}, \lambda)$  by the replacements  $\phi \rightarrow \phi + \pi$  and  $\theta \rightarrow \pi - \theta$  so that

$$\chi_{\lambda}(-\hat{p}) = -2\lambda e^{2i\lambda\phi} \chi_{-\lambda}(\hat{p}) \quad (\text{A.8})$$

and

$$u(-\vec{p}, \lambda) = -2\lambda e^{2i\lambda\phi} \begin{pmatrix} f_{+\chi_{-\lambda}(\hat{p})} \\ 2\lambda f_{-\chi_{-\lambda}(\hat{p})} \end{pmatrix}. \quad (\text{A.9})$$

Using the relationship between  $v(\vec{p}, \lambda)$  and  $u(\vec{p}, \lambda)$  and  $-i\sigma_2 \chi_{\lambda}^*(\hat{p}) = +2\lambda \chi_{-\lambda}(\hat{p})$ , the spinor  $v(\vec{p}, \lambda)$  can be written as:

$$v(\vec{p}, \lambda) \equiv -i\gamma^2 u^*(\vec{p}, \lambda) = \begin{pmatrix} f_{-\chi_{-\lambda}(\hat{p})} \\ -2\lambda f_{+\chi_{-\lambda}(\hat{p})} \end{pmatrix}. \quad (\text{A.10})$$

The Dirac adjoint spinors  $\bar{v}(\vec{p}, \lambda)$  and  $\bar{u}(-\vec{p}, \lambda)$  can now be found,

$$\bar{v}(\vec{p}, \lambda) \equiv v^{\dagger}(\vec{p}, \lambda) \gamma^0 = (f_{-\chi_{-\lambda}^{\dagger}(\hat{p})}, 2\lambda f_{+\chi_{-\lambda}^{\dagger}(\hat{p})}) \quad (\text{A.11})$$

$$\bar{u}(-\vec{p}, \lambda) \equiv u^{\dagger}(-\vec{p}, \lambda) \gamma^0 = -2\lambda e^{-2i\lambda\phi} (f_{+\chi_{-\lambda}^{\dagger}(\hat{p})}, -2\lambda f_{-\chi_{-\lambda}^{\dagger}(\hat{p})}). \quad (\text{A.12})$$

Recall that  $\langle 0 | J^0 | p \vec{p} \rangle = 0$  due to current conservation in the center-of-mass (CM) system. Thus only the vector components  $\langle 0 | \vec{J} | p \vec{p} \rangle$  in the expression for  $\mathcal{M}$  in the CM system remain to be calculated. With  $\vec{A} \cdot \vec{B} = A^z B^z + \frac{1}{2}(A^+ B^- + A^- B^+)$ ,



where  $A^\pm \equiv A^x \pm iA^y$  and  $B^\pm \equiv B^x \pm iB^y$ , the invariant amplitude  $\mathcal{M}$  can be decomposed in the same way (compare Eq. (A.3)):

$$\mathcal{M} \sim J^z j^z + \frac{1}{2}(J^+ j^- + J^- j^+) \quad (\text{A.13})$$

Using the above spinors in the CM frame, the  $\mathcal{M}^{zz}$  part of Eq. (A.3) can be written as:

$$\mathcal{M}^{zz} = \frac{4\pi\alpha}{q^2} \frac{E_e}{m} \cdot G_E \cdot 2\lambda_p \cdot \delta_{\lambda_p, \bar{\lambda}_p} \times \chi_{-\lambda_e}^\dagger(\hat{k}) \sigma^3 \chi_{-\bar{\lambda}_e}(\hat{k}) \delta_{\lambda_e, -\bar{\lambda}_e} \quad (\text{A.14})$$

where the following usual definition was used:

$$G_E(Q^2) \equiv F_1(Q^2) + \frac{s}{4M_p^2} F_2(Q^2) \quad (\text{A.15})$$

Now let's turn to  $\mathcal{M}^{+-}$  and  $\mathcal{M}^{-+}$  parts of Eq. (A.3):

$$\mathcal{M}^{\pm\mp} = -\frac{1}{2} \cdot \frac{4\pi\alpha}{q^2} \cdot \bar{v}(p\hat{z}, \bar{\lambda}_p) \gamma^\pm (F_1(Q^2) + F_2(Q^2)) u(-p\hat{z}, \lambda_p) \times \bar{u}(-\vec{k}, \lambda_e) \gamma_\mp v(\vec{k}, \bar{\lambda}_e) \quad (\text{A.16})$$

where the first term is calculated as:

$$\bar{v}(p\hat{z}, \bar{\lambda}_p) \gamma^\pm (F_1(Q^2) + F_2(Q^2)) u(-p\hat{z}, \lambda_p) = -\frac{E_p}{M_p} (1 \pm 2\lambda_p) \delta_{\lambda_p, -\bar{\lambda}_p} \quad (\text{A.17})$$

and in the limit of  $m_e \ll E_e$ , the second term of Eq. (A.16) is calculated as:

$$\bar{u}(-\vec{k}, \lambda_e) \gamma_\pm v(\vec{k}, \bar{\lambda}_e) = -\frac{E_e}{m_e} e^{-2i\lambda_e\phi} \chi_{-\lambda_e}^\dagger(\hat{k}) \sigma^\pm \chi_{-\bar{\lambda}_e} \delta_{\lambda_e, -\bar{\lambda}_e} \quad (\text{A.18})$$

With the following usual definition,

$$G_M(Q^2) \equiv F_1(Q^2) + F_2(Q^2) \quad (\text{A.19})$$

Eq. (A.16) now becomes:

$$\mathcal{M}^{\pm\mp} = -\frac{1}{2} \cdot \frac{4\pi\alpha}{q^2} \frac{E_e}{m_e} \left( \frac{E_p}{M_p} G_M \right) (1 \pm 2\lambda_p) \delta_{\lambda_p, -\bar{\lambda}_p} \times e^{-2i\lambda_e\phi} \chi_{-\lambda_e}^\dagger(\hat{k}) \sigma^\mp \chi_{-\bar{\lambda}_e} \delta_{\lambda_e, -\bar{\lambda}_e} \quad (\text{A.20})$$

From the above expressions of  $\mathcal{M}^{zz}$ ,  $\mathcal{M}^{+-}$  and  $\mathcal{M}^{-+}$ , it's obvious that  $G_E$  appears only in the z-component  $\langle 0 | J^z | p\bar{p} \rangle$  where helicities of  $\bar{p}$  and  $p$  are the same, corresponding to the helicity amplitude  $C_{|\lambda_p - \bar{\lambda}_p|} = C_0$ , and  $G_M$  appears in the  $+-$  or  $-+$  components where helicities of  $\bar{p}$  and  $p$  are opposite resulting in  $C_{|\lambda_p - \bar{\lambda}_p|} = C_1$ . Table A.1 shows the Eq. (A.14) and (A.20) in a more illustrative way.

The angular distribution is obtained from the modulus of the total amplitude squared by averaging over all the possible initial helicity states and adding up all the possible final helicity states since initial and final particles are unpolarized.

$$\begin{aligned} \overline{|\mathcal{M}|^2} &= \frac{1}{4} [ |m(R\bar{R} \rightarrow R\bar{L})|^2 + |m(R\bar{R} \rightarrow L\bar{R})|^2 + |m(L\bar{L} \rightarrow R\bar{L})|^2 + \\ &\quad + |m(L\bar{L} \rightarrow L\bar{R})|^2 + |m(R\bar{L} \rightarrow R\bar{L})|^2 + |m(R\bar{L} \rightarrow L\bar{R})|^2 + \\ &\quad + |m(L\bar{R} \rightarrow R\bar{L})|^2 + |m(L\bar{R} \rightarrow L\bar{R})|^2 ] \\ &\sim \frac{1}{4} \left[ 4 |G_E|^2 \sin^2 \theta + 8 \left| \frac{E_p}{M_p} G_M \right|^2 \cos^4 \left( \frac{\theta}{2} \right) + 8 \left| \frac{E_p}{M_p} G_M \right|^2 \sin^4 \left( \frac{\theta}{2} \right) \right] \\ &= \left( \left| \frac{E_p}{M_p} G_M \right|^2 + |G_E|^2 \right) \left[ 1 + \left( \frac{\left| \frac{E_p}{M_p} G_M \right|^2 - |G_E|^2}{\left| \frac{E_p}{M_p} G_M \right|^2 + |G_E|^2} \right) \cdot \cos^2 \theta \right]. \quad (\text{A.21}) \end{aligned}$$

$\bar{p}p$ part ( $J^\mu$ )						$e^+e^-$ part ( $j_\mu$ )		
$C_{ \lambda_p - \bar{\lambda}_p }$	$\mu \Rightarrow$	0	z	+	-	$\mu \Downarrow$	R $\bar{L}$	L $\bar{R}$
$C_0$	R $\bar{R}$	0	$G_E$	0	0	z	$-\sin\theta e^{i\phi}$	$-\sin\theta e^{-i\phi}$
	L $\bar{L}$	0	$-G_E$	0	0	z	$-\sin\theta e^{i\phi}$	$-\sin\theta e^{-i\phi}$
$C_1$	R $\bar{L}$	0	0	$\frac{E_p}{M_p} G_M$	0	-	$2\cos^2(\frac{\theta}{2})$	$2\sin^2(\frac{\theta}{2})e^{-2i\phi}$
	L $\bar{R}$	0	0	0	$\frac{E_p}{M_p} G_M$	+	$2\sin^2(\frac{\theta}{2})e^{2i\phi}$	$2\cos^2(\frac{\theta}{2})$

Table A.1: Each component of currents and helicities of  $\bar{p}p$  and  $e^+e^-$ . In  $e^+e^-$  part, the values are from the direct calculation of  $\chi_{-\lambda_e}^\dagger(\hat{k})\vec{\sigma}\chi_{-\bar{\lambda}_e}\delta_{\lambda_e, -\bar{\lambda}_e}$ .

Finally we get the following relation:

$$\frac{dN}{d\cos\theta} \propto |\overline{\mathcal{M}}|^2 \propto 1 + \lambda \cos^2\theta \quad (\text{A.22})$$

where,

$$\lambda \equiv \frac{\left|\frac{E_p}{M_p}G_M\right|^2 - |G_E|^2}{\left|\frac{E_p}{M_p}G_M\right|^2 + |G_E|^2} = \frac{|G_M|^2 - \left|\frac{M_p}{E_p}G_E\right|^2}{|G_M|^2 + \left|\frac{M_p}{E_p}G_E\right|^2}. \quad (\text{A.23})$$

Eq. (A.23) can be rewritten as:

$$\left|\frac{G_E}{G_M}\right| = \frac{E_p}{M_p} \sqrt{\frac{1-\lambda}{1+\lambda}} = \frac{\sqrt{s}}{2M_p} \sqrt{\frac{1-\lambda}{1+\lambda}} \quad (\text{A.24})$$

Since  $G_E$  and  $G_M$  correspond to  $C_0$  and  $C_1$ , respectively, we can define them up to a certain factor as  $\frac{2M_p}{\sqrt{s}}|G_E| \equiv |C_0|$  and  $|G_M| \equiv |C_1|$  so that  $|C_0| \rightarrow 0$  as  $\frac{2M_p}{\sqrt{s}} \rightarrow 0$  as in the case of electron. Then Eq. (A.23) is expressed as:

$$\lambda = \frac{|C_1|^2 - |C_0|^2}{|C_1|^2 + |C_0|^2} \quad (\text{A.25})$$

The above Eq. (A.25) can be rewritten as:

$$\left| \frac{C_0}{C_1} \right| = \sqrt{\frac{1 - \lambda}{1 + \lambda}} \quad (\text{A.26})$$

# Appendix B

## Helicity Amplitudes for the Process $\bar{p}p \rightarrow e^+e^-$

### B.1 Wigner D-function and 2-body decay amplitude

Wigner's D-function is defined as a rotational transformation of the initial state to the final state in an interaction of particles. In this process the total angular momentum is conserved while the x, y, and z components of the total angular momentum are changed as a result of the transformation. By this definition the Wigner's D-function can be written as:

$$\begin{aligned} D_{M'M}^J(\alpha, \beta, \gamma) &\equiv \langle JM' | R(\alpha, \beta, \gamma) | JM \rangle \\ &= \langle JM' | e^{-i\alpha J_z} e^{-i\beta J_y} e^{-i\gamma J_z} | JM \rangle \\ &= e^{-i\alpha M'} d_{M'M}^J(\beta) e^{-i\gamma M} \end{aligned} \tag{B.1}$$

where,

$$d_{M'M}^J(\beta) \equiv \langle JM' | e^{-i\beta J_y} | JM \rangle. \tag{B.2}$$

Now let's consider the decay of a particle into a two-particle final state. Helicity is a useful concept to describe relativistic particle decay or scattering because it is invariant under rotations by its definition,  $\lambda \equiv \frac{\vec{p} \cdot \vec{s}}{|\vec{p} \cdot \vec{s}|}$ . Let's assume the initial particles' total angular momentum is  $J$  and the two final particles' helicities are  $\lambda_1$  and  $\lambda_2$ , respectively:

$$(J) \longrightarrow 1 (\lambda_1) + 2 (\lambda_2)$$

Using S-matrix<sup>1</sup> the decay amplitude of this process can be written as:

$$\begin{aligned} \mathcal{M} &\sim \langle \vec{p}_f, \lambda_1, \lambda_2 | T | JM \rangle \\ &\sim \langle \theta, \phi, \lambda_1, \lambda_2 | T | JM \rangle \\ &= \sum_{j,m} \langle \theta, \phi, \lambda_1, \lambda_2 | j, m, \lambda_1, \lambda_2 \rangle \langle j, m, \lambda_1, \lambda_2 | T | JM \rangle \\ &= \sum_{j,m} \langle \theta, \phi, \lambda_1, \lambda_2 | j, m, \lambda_1, \lambda_2 \rangle \delta_{mM} \delta_{jJ} A_{\lambda_1 \lambda_2} \\ &= \langle \theta, \phi, \lambda_1, \lambda_2 | J, M, \lambda_1, \lambda_2 \rangle A_{\lambda_1 \lambda_2} \\ &= \langle \lambda_1, \lambda_2 | R(\phi, \theta, -\phi) | J, M, \lambda_1, \lambda_2 \rangle A_{\lambda_1 \lambda_2} \end{aligned} \tag{B.3}$$

where  $A_{\lambda_1 \lambda_2} \equiv \langle \lambda_1, \lambda_2 \rangle$ . By applying the definition of the D-function to the last line of the Eq. (B.3), the 2-body decay amplitude can be written as:

$$\mathcal{M} \sim D_{M\lambda}^{*J}(\phi, \theta, -\phi) A_{\lambda_1 \lambda_2} \tag{B.4}$$

where  $\lambda \equiv \lambda_1 - \lambda_2$ .

---

<sup>1</sup> $S_{fi} = \delta_{fi} + i(2\pi)^4 \delta^4(P_i - P_f) T_{fi}$

## B.2 Angular distribution and the helicity amplitudes for the process

$$\bar{p}p \ (\lambda_{\bar{p}}\lambda_p) \rightarrow \psi'(\lambda) \rightarrow e^+e^- \ (\lambda_{\bar{e}}\lambda_e)$$

The process,  $\bar{p}p \ (\lambda_{\bar{p}}\lambda_p) \rightarrow \psi'(\lambda) \rightarrow e^+e^- \ (\lambda_{\bar{e}}\lambda_e)$ , consists of two parts: the production of the  $\psi'$  from  $\bar{p}p$  annihilation and the decay of the  $\psi'$  to  $e^+e^-$ . By applying Eq. (B.3) to each part of the whole process, the invariant amplitude of this process becomes:

$$\mathcal{M} \sim \sum_{M_z} C_{M_z} D_{\lambda_{\bar{p}}-\lambda_p, M_z}^{J(\psi')} (0, 0, 0) \cdot A_{\lambda_{e^+}\lambda_{e^-}} D_{M_z, \lambda_{e^+}-\lambda_{e^-}}^{*J(\psi')} (\phi, \theta, -\phi) \quad (\text{B.5})$$

where,  $C_{M_z}$  is the amplitude for the production of the  $\psi'$  from  $\bar{p}p$ , and  $A_{\lambda_{e^+}\lambda_{e^-}}$  is the amplitude for the decay of the  $\psi'$  to  $e^+e^-$ .

The production angles  $(\theta, \phi)$  in the first  $D$  function in Eq. (B.5) were chosen as zero based on the fact that the relative decay angles of the final particles will not be affected by this choice of reference frame resulting in  $D_{\lambda_{\bar{p}}-\lambda_p}^{J(\psi')} = \delta_{M_z, (\lambda_{\bar{p}}-\lambda_p)}$ . The mass of electron is negligible in this process thus the chiral symmetry is effective resulting in the relative helicities between  $e^+$  and  $e^-$  as:  $\lambda_{\bar{e}e} \equiv \lambda_{e^+} - \lambda_{e^-} = \pm 1$ . The mass of the proton, however, can not be neglected. Thus the possible relative helicities for this process between  $\bar{p}$  and  $p$  are:  $\lambda_{\bar{p}p} \equiv \lambda_{\bar{p}} - \lambda_p = +1, -1, 0$  (for  $J = 1$ ).<sup>2</sup> The equation (B.5) is rewritten as:

$$\mathcal{M} \sim D_{\lambda_{\bar{p}p}, \lambda_{\bar{e}e}}^{*(1)} (\phi, \theta, -\phi) A_{\lambda_{\bar{e}e}} C_{\lambda_{\bar{p}p}}. \quad (\text{B.6})$$

The following relationships can be obtained under helicity conservation:

$$A_{\lambda_{\bar{e}e}} = \eta_{\psi'} \eta(-1)^{S_{\psi'} - S_{e^+} - S_{e^-}} A_{-\lambda_{\bar{e}e}}$$

---

<sup>2</sup>  $J = 0$  is excluded due to total angular momentum conservation.

$$C_{\lambda_{\bar{p}p}} = \eta_{\lambda_{\bar{p}p}} \eta_{\psi'} (-1)^{S_{\bar{p}} + S_p - S_{\psi'}} C_{-\lambda_{\bar{p}p}}. \quad (\text{B.7})$$

From the above Eq. (B.7), it's obvious that  $A_1 = A_{-1}$  and  $C_1 = C_{-1}$ .

The angular distribution of the process using an unpolarized beam, can be obtained by averaging all possible initial states and summing up all final states of the invariant amplitude squared in Eq. (B.6):

$$\begin{aligned} \frac{d\sigma}{d\Omega} &\sim \overline{|\mathcal{M}|^2} \\ &\sim \sum_{\lambda_{\bar{p}p}, \lambda_{\bar{e}e}} |A_{\lambda_{\bar{e}e}}|^2 |C_{\lambda_{\bar{p}p}}|^2 D_{\lambda_{\bar{p}p} \lambda_{\bar{e}e}}^1(\phi, \theta, -\phi) D_{\lambda_{\bar{p}p} \lambda_{\bar{e}e}}^{*1}(\phi, \theta, -\phi) \\ &= |A_1|^2 |C_1|^2 |D_{1,1}^1|^2 + |A_{-1}|^2 |C_1|^2 |D_{1,-1}^1|^2 + |A_1|^2 |C_{-1}|^2 |D_{-1,1}^1|^2 \\ &+ |A_{-1}|^2 |C_{-1}|^2 |D_{-1,-1}^1|^2 + |A_1|^2 |C_0|^2 |D_{0,1}^1|^2 + |A_{-1}|^2 |C_0|^2 |D_{0,-1}^1|^2 \\ &= |A_1|^2 |C_1|^2 (|D_{1,1}^1|^2 + |D_{1,-1}^1|^2 + |D_{-1,1}^1|^2 + |D_{-1,-1}^1|^2) \\ &+ |A_1|^2 |C_0|^2 (|D_{0,1}^1|^2 + |D_{0,-1}^1|^2). \end{aligned} \quad (\text{B.8})$$

By using the definition of the  $D$  function in Eq. (B.1),

$$D_{\lambda'\lambda}^J(\phi, \theta, -\phi) = e^{i(\lambda - \lambda')\phi} d_{\lambda'\lambda}^J(\theta). \quad (\text{B.9})$$

Now using the relation above, the following results are obtained:

$$\begin{aligned} |D_{1,1}^1| &= |d_{1,1}^1| = \left| \frac{1 + \cos \theta}{2} \right| = |D_{-1,-1}^1| \\ |D_{1,-1}^1| &= |d_{1,-1}^1| = \left| \frac{1 - \cos \theta}{2} \right| = |D_{-1,1}^1| \\ |D_{0,1}^1| &= |d_{0,1}^1| = \left| \frac{-\sin \theta}{\sqrt{2}} \right| = |D_{0,-1}^1|. \end{aligned} \quad (\text{B.10})$$



Using the values above, the Eq. (B.8) becomes:

$$\begin{aligned}
\overline{|\mathcal{M}|^2} &\sim |C_1|^2 \left( 2 \cdot \frac{(1 + \cos \theta)^2}{4} + 2 \cdot \frac{(1 - \cos \theta)^2}{4} \right) + |C_0|^2 \left( 2 \cdot \frac{\sin^2 \theta}{2} \right) \\
&= |C_1|^2 (1 + \cos^2 \theta) + |C_0|^2 \sin^2 \theta \\
&= (|C_1|^2 + |C_0|^2) + (|C_1|^2 - |C_0|^2) \cos^2 \theta \\
&= (|C_1|^2 + |C_0|^2) \left( 1 + \frac{|C_1|^2 - |C_0|^2}{|C_1|^2 + |C_0|^2} \cos^2 \theta \right). \tag{B.11}
\end{aligned}$$

The above Eq. (B.11) can be rewritten as:

$$\frac{d\sigma}{d\Omega} \sim \overline{|\mathcal{M}|^2} \sim 1 + \lambda \cos^2 \theta \tag{B.12}$$

where

$$\lambda \equiv \frac{|C_1|^2 - |C_0|^2}{|C_1|^2 + |C_0|^2}. \tag{B.13}$$

## Appendix C

# GEANT Monte Carlo Study of “shower splash” and bremsstrahlung

This Appendix is intended to provide details of the study of “shower splash” and Bremsstrahlung events done using the GEANT MC. It should be read in conjunction with Chapter 5.

The flexibility of the GEANT MC program allows for simulations to be run with different elements of the complete detector taken to be operative or not. That is, to be “on” or “off”. When an additional cluster is produced in a simulated event with the complete detector “on”, it is caused by either “shower splash” or bremsstrahlung. However, when a shower from an  $e^+e^-$  event produces additional clusters with only the calorimeters CCAL and FCAL “on”, it must have been caused by “shower splash” since there is no source of bremsstrahlung at the inner detectors or the beam pipe which are turned “off”. Thus subtracting the number of  $e^+e^-$  events with additional clusters with only calorimeters “on” from those with the complete detector “on”, gave the number of  $e^+e^-$  events with additional clusters caused by bremsstrahlung.

To do this study, a total of 100,000  $e^+e^-$  events was generated with a uniform angular distribution ( $\lambda = 0$ ). Events were selected only when the probability <sup>1</sup>

---

<sup>1</sup>A fit probability of  $10^{-5}$  is the minimal condition for passing 4C kinematic fit.

of the 4C kinematical fit was greater than  $10^{-5}$  as well as when all pre-selection criteria were satisfied: seed/cluster threshold, the number of clusters, cluster timing and geometrical acceptance (see Table 2 in Chapter 5). Table C.1 lists the number of  $e^+e^-$  events with and without additional clusters obtained by using the 1996-1997 MC, with all detectors “on” and with only CCAL and FCAL “on”. Table C.2 is structured as Table C.1 but using the 2000 MC. From the two tables, with all detectors “on” it is seen that there were more additional-cluster events in the 1996-1997 MC than those in the 2000 MC. However, when only CCAL and FCAL were “on”, the number of additional-cluster events in both MCs appears to be the same. This difference between the two MCs seemed to be caused by the silicon detector (located between Hodoscopes (H2') and Straw chambers (Str2)) existed only in the 1996-1997 run because its presence can lead to more bremsstrahlung events which result in more additional clusters.

Figure C.1 shows the number of events with three clusters divided by the total number of events as a function of the seed/cluster thresholds. These plots show that the fraction of 3-cluster events decreases as the seed/cluster threshold increases and starts saturating from 80/80 MeV. The saturation level was higher in the 1996-1997 MC ( $\sim 1\%$ ) than that in the 2000 MC ( $\sim 0\%$ ), and this was again due to the silicon detector which produced more bremsstrahlungs in the 1996-1997 MC.

As far as the events with additional clusters are conserved, the choice of 50/50 MeV as a seed/cluster threshold was reasonable since we did not want to remove all events with additional clusters originating from bremsstrahlung or “shower splash”. With the complete detector “on”, the fraction of 4-cluster events among all the additional-cluster events using the 1996-1997 MC, varied from  $(30.0 \pm 0.8)\%$  to  $(0.8 \pm 0.4)\%$  in order of increasing seed/cluster threshold, while with only CCAL and FCAL “on”, it varied from  $(3.1 \pm 0.3)\%$  to  $0\%$ . The same fraction varied from  $(2.5 \pm 0.3)\%$  to  $0\%$  in both cases using the 2000 MC. Table C.3 lists the fraction of the number of  $e^+e^-$  events with additional clusters with only CCAL and FCAL “on”, to that with all detectors “on”, according to the seed/cluster thresholds. The higher the fraction, the more numerous the events with additional clusters which are not associated with the inner detectors or the beam pipe, which reveals the level of “shower splash” in the CCAL and FCAL. This fraction decreased as the

seed/cluster threshold increased (see Figure C.2), which meant that “shower splash” events were more affected by the seed/cluster threshold than bremsstrahlung ones. From 25/50 MeV to 50/50 MeV, the corresponding fractions seemed to be the same in both MCs. However, beyond the 50/50 MeV threshold, the fraction of events with additional clusters decreased faster in the 1996-1997 MC and this was due to the silicon detector in the 1996-1997 MC. With the 50/50 MeV threshold,  $(52.2 \pm 2.4)\%$  and  $(58.9 \pm 3.4)\%$  of all the additional-cluster events were due to “shower splash” in the 1996-1997 MC and the 2000 MC, respectively.

Figure C.3 shows  $\theta_{lab}$  (in degree) as a function of  $\cos\theta^*$ . In the 1996-1997 MC, the 3-cluster events with the complete detector “on” showed a flat angular distribution. See Figures C.4 and C.5 (white area). In the 2000 MC, however, the 3-cluster events with the complete detector “on” were forward peaked. See Figures C.6 and C.7 (white area). This means that  $e^+e^-$  events with bremsstrahlung generated at the inner detectors or the beam pipe, have a higher energy than those generated at the silicon detector. In both cases, however, “shower splash” happened everywhere resulting in a flat angular distribution. See Figures C.4, C.5, C.6 and C.7 (hatched area). Thus as a result of this study, the number of clusters were chosen as two for  $e^+e^-$ , and up to two additional clusters were allowed to take into account bremsstrahlung in the inner detectors or the beam pipe, and “shower splash” in the calorimeters.

	# of events w/ all detectors	# of events w/ CCAL+FCAL	# of events w/ all detectors	# of events w/ CCAL+FCAL
Threshold	25/50		30/50	
2 clusters	57137	57770	57664	58316
3 clusters	2342	2627	2019	2112
4 clusters	955	84	766	56
Total	60434	60481	60449	60484
Threshold	35/50		40/50	
2 clusters	58245	58858	58674	59303
3 clusters	1663	1594	1399	1163
4 clusters	554	32	398	20
Total	60462	60484	60471	60486
Threshold	45/50		50/50	
2 clusters	58972	59619	59172	59806
3 clusters	1230	858	1101	676
4 clusters	278	13	212	9
Total	60480	60490	60485	60491
Threshold	60/60		70/70	
2 clusters	59507	60128	59644	60267
3 clusters	861	366	766	230
4 clusters	128	2	87	1
Total	60496	60496	60497	60498
Threshold	80/80		90/90	
2 clusters	59724	60354	59772	60397
3 clusters	708	147	680	104
4 clusters	66	0	45	0
Total	60498	60501	60497	60501
Threshold	100/100		110/110	
2 clusters	59798	60427	59818	60443
3 clusters	668	75	659	59
4 clusters	35	0	24	0
Total	60501	60502	60501	60502
Threshold	120/120		130/130	
2 clusters	59828	60455	59838	60469
3 clusters	654	47	651	33
4 clusters	19	0	13	0
Total	60501	60502	60502	60502
2 clusters	59847	60475	59852	60481
3 clusters	645	27	640	21
4 clusters	10	0	10	0
Total	60502	60502	60502	60502
Threshold	170/170		200/200	
2 clusters	59857	60484	59865	60491
3 clusters	635	18	630	11
4 clusters	9	0	5	0
Total	60501	60502	60500	60502

Table C.1: The number of events assorted with the number of clusters according to the seed/cluster thresholds. See text.

	# of events w/ all detectors	# of events w/ CCAL+FCAL	# of events w/ all detectors	# of events w/ CCAL+FCAL
Threshold	25/50		30/50	
2 clusters	57983	58619	58588	59171
3 clusters	2993	2413	2418	1885
4 clusters	78	62	53	46
Total	61054	61094	61059	61102
Threshold	35/50		40/50	
2 clusters	59206	59706	59665	60136
3 clusters	1825	1374	1386	961
4 clusters	35	25	18	12
Total	61066	61105	61069	61109
Threshold	45/50		50/50	
2 clusters	60012	60444	60259	60633
3 clusters	1049	659	806	477
4 clusters	10	7	9	3
Total	61070	61110	61074	61113
Threshold	60/60		70/70	
2 clusters	60615	60896	60773	60985
3 clusters	464	218	312	131
4 clusters	1	1	0	0
Total	61080	61115	61085	61116
Threshold	80/80		90/90	
2 clusters	60865	61029	60924	61058
3 clusters	222	88	164	59
4 clusters	0	0	0	0
Total	61087	61117	61088	61117
Threshold	100/100		110/110	
2 clusters	60950	61077	60979	61085
3 clusters	140	40	111	32
4 clusters	0	0	0	0
Total	61090	61117	61090	61117
Threshold	120/120		130/130	
2 clusters	60998	61094	61014	61099
3 clusters	92	23	76	18
4 clusters	0	0	0	0
Total	61090	61117	61090	61117
Threshold	140/140		150/150	
2 clusters	61027	61101	61035	61104
3 clusters	64	15	55	12
4 clusters	0	0	0	0
Total	61091	61116	61090	61116
Threshold	170/170		200/200	
2 clusters	61047	61106	61065	61110
3 clusters	42	10	24	5
4 clusters	0	0	0	0
Total	61089	61116	61089	61115

Table C.2: The number of  $e^+e^-$  events assorted with the number of clusters according to the seed/cluster thresholds. See text.

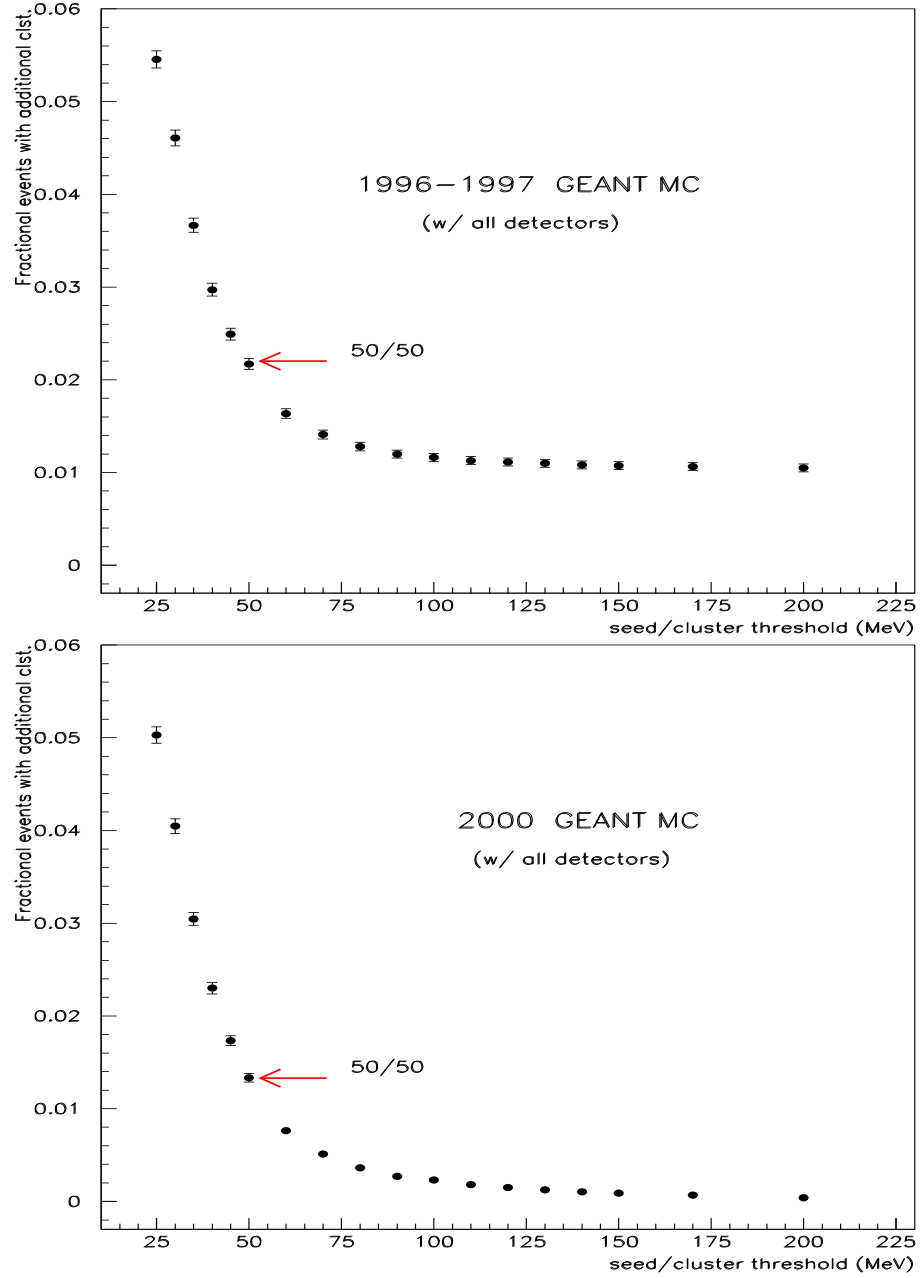


Figure C.1: 3-cluster events normalized to the total # of events vs. seed/cluster threshold using the 1996-1997 MC (Top) and the 2000 MC (Bottom).

seed/cluster threshold	1996-1997 MC		2000 MC	
(MeV)	fraction	error	fraction	error
25/50	0.822	0.021	0.805	0.021
30/50	0.778	0.022	0.781	0.023
35/50	0.733	0.024	0.752	0.026
40/50	0.658	0.024	0.693	0.029
45/50	0.577	0.024	0.629	0.031
50/50	0.522	0.024	0.589	0.034
60/60	0.372	0.023	0.471	0.038
70/70	0.271	0.020	0.420	0.044
80/80	0.190	0.017	0.396	0.050
90/90	0.143	0.015	0.360	0.055
100/100	0.107	0.013	0.286	0.051
110/110	0.086	0.012	0.288	0.058
120/120	0.070	0.011	0.250	0.058
130/130	0.050	0.009	0.237	0.062
140/140	0.041	0.008	0.234	0.067
150/150	0.032	0.007	0.218	0.069
170/170	0.028	0.007	0.238	0.084
200/200	0.017	0.005	0.208	0.102

Table C.3: The number of events with additional clusters with only CCAL and FCAL “on”, divided by that with the complete detector “on” according to the seed/cluster threshold. A total of 100,000  $e^+e^-$  MC events was generated at the  $\psi'$ .



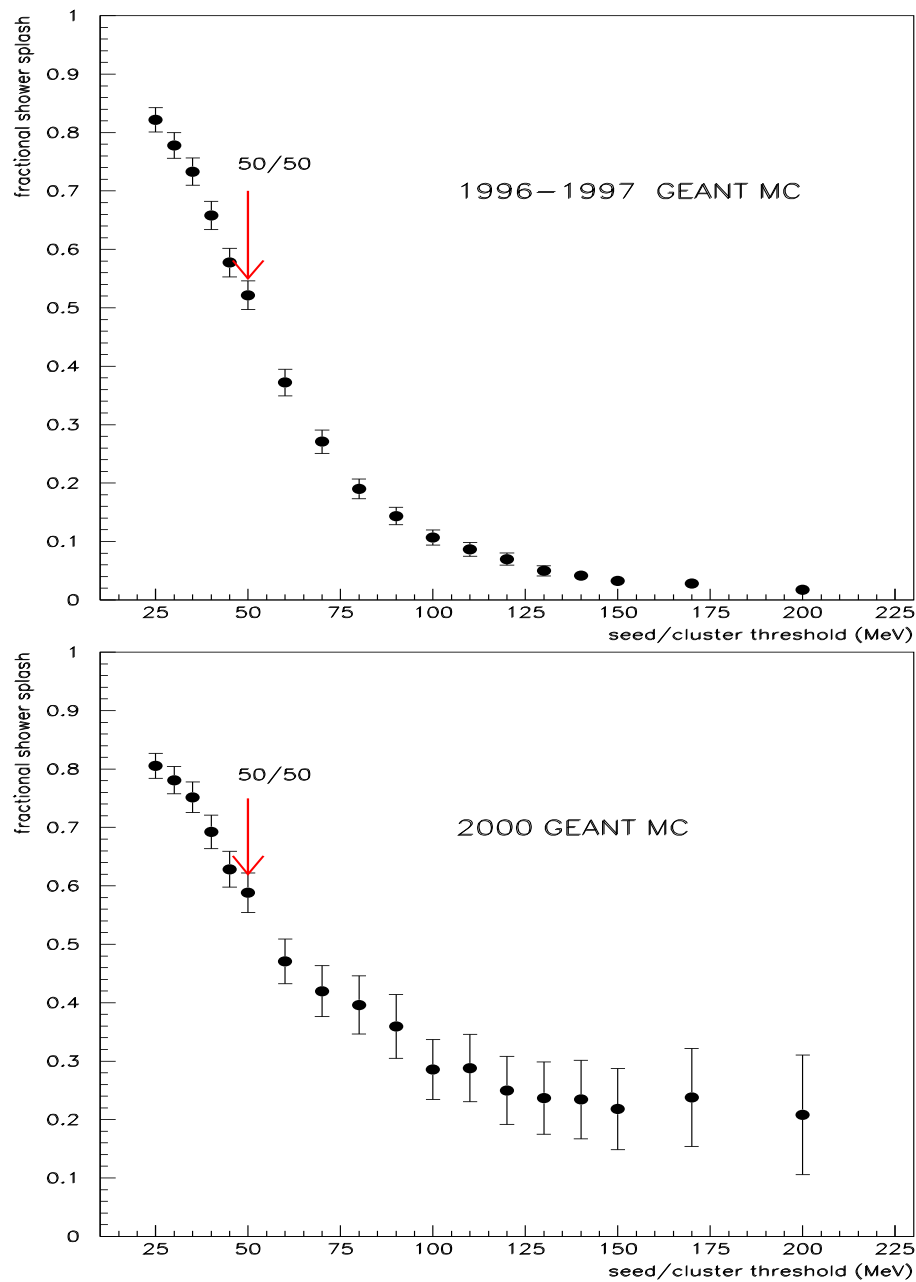


Figure C.2: Graphical representation of Table C.3.

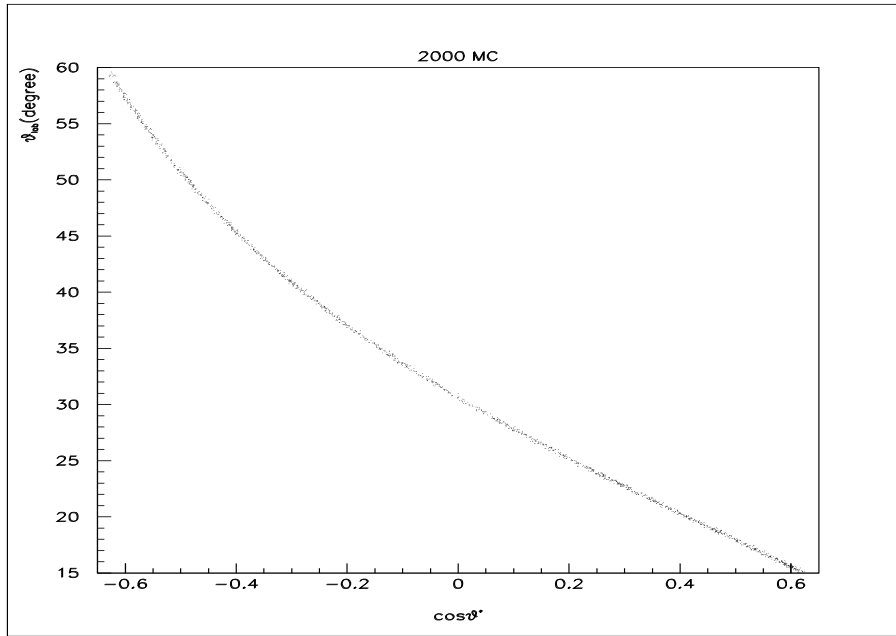


Figure C.3:  $\theta_{lab}$  vs.  $\cos\theta^*$  obtained from  $e^+e^-$  events using the 2000 GEANT MC.

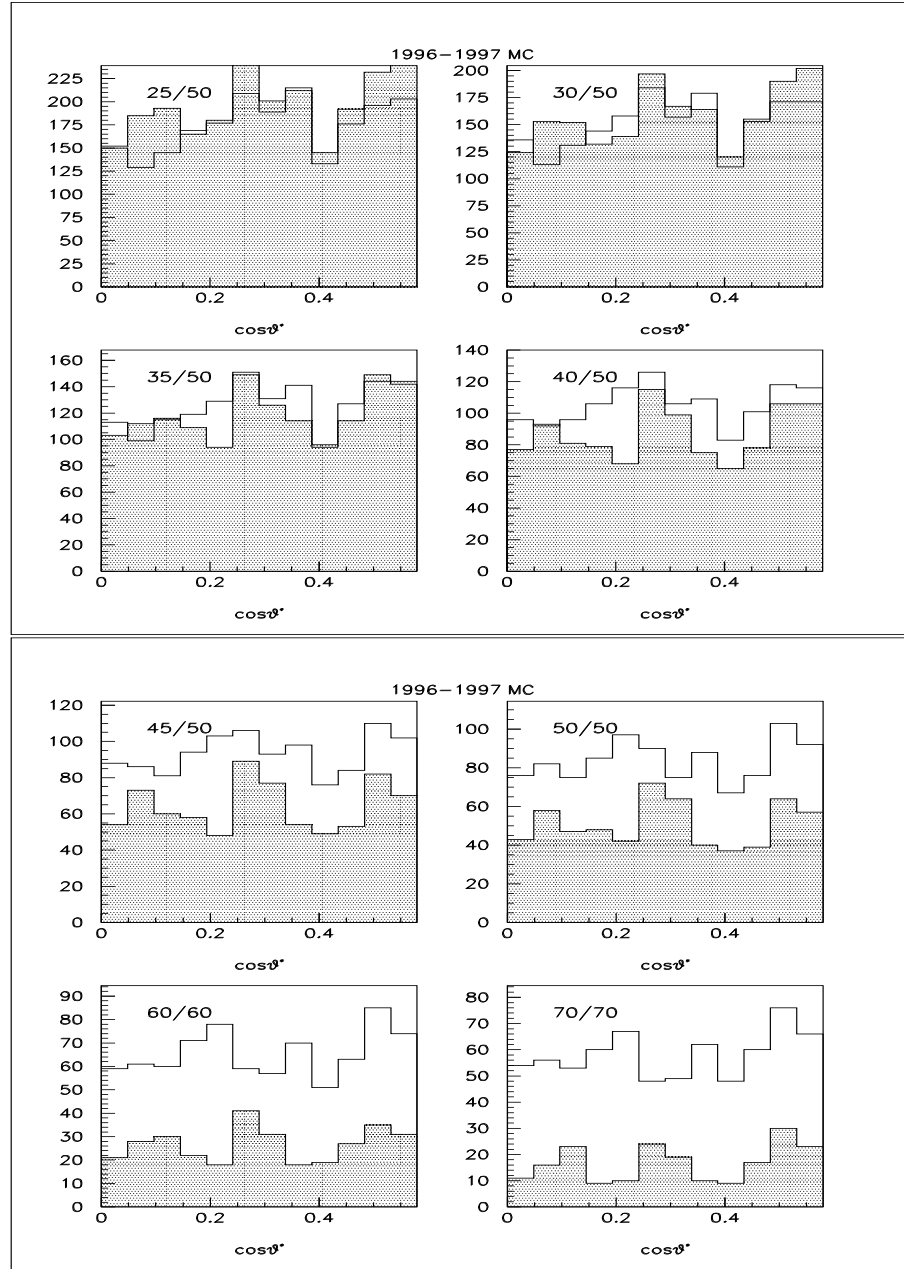


Figure C.4: Angular distribution of the 3-cluster events with the complete detector "on" (white area) and with CCAL and FCAL "on" (hatched area) according to seed/cluster thresholds (25/50 to 70/70) obtained by using the 1996-1997 GEANT MC.

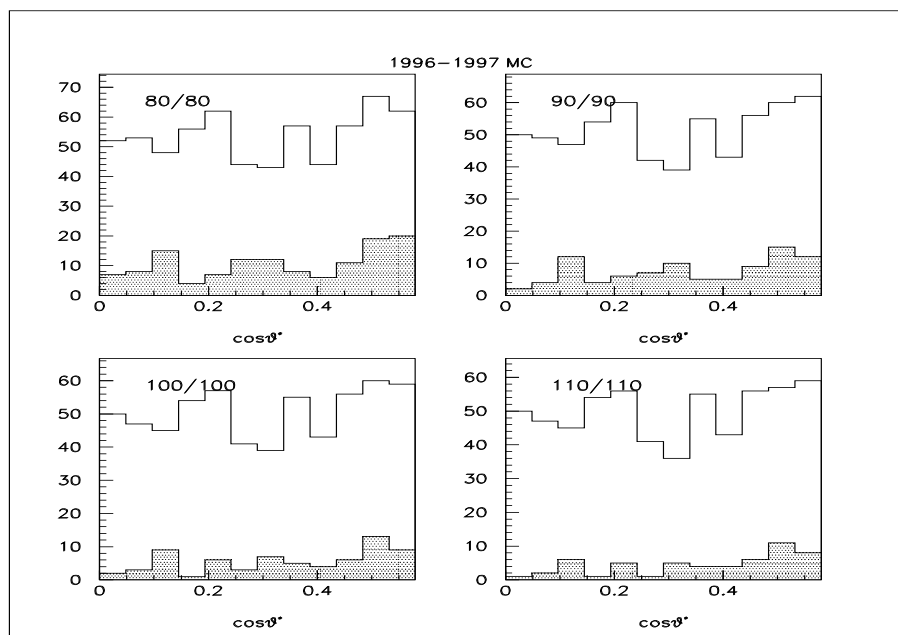


Figure C.5: Angular distribution of the 3-cluster events with the complete detector “on” (white area) and with CCAL and FCAL “on” (hatched area) according to seed/cluster thresholds (80/80 to 110/110) obtained by using the 1996-1997 GEANT MC.

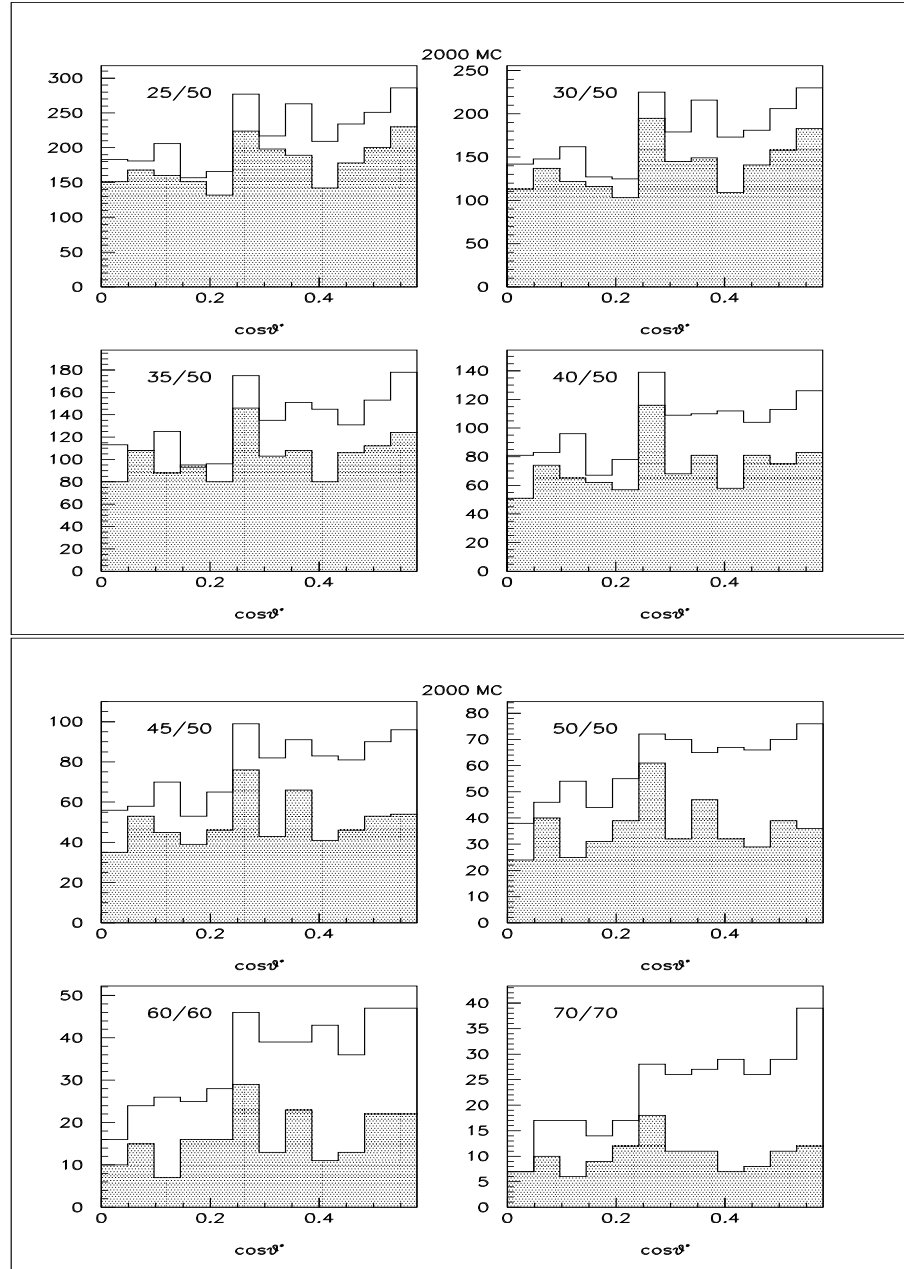


Figure C.6: Angular distribution of the 3-cluster events with the complete detector “on” (white area) and with CCAL and FCAL “on” (hatched area) according to seed/cluster thresholds (25/50 to 70/70) obtained by using the 2000 GEANT MC.

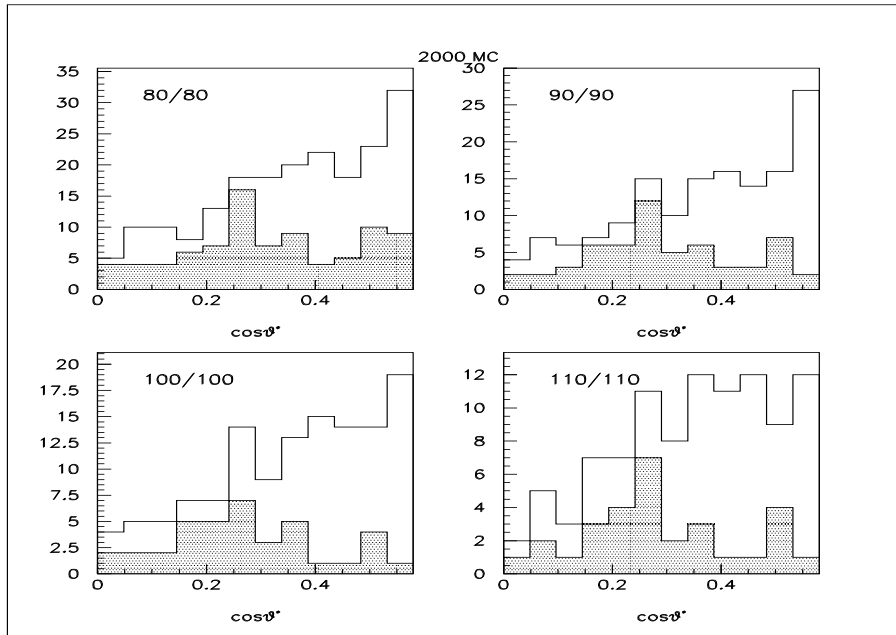


Figure C.7: Angular distribution of the 3-cluster events with the complete detector “on” (white area) and with CCAL and FCAL “on” (hatched area) according to seed/cluster thresholds (80/80 to 110/110) obtained by using the 2000 GEANT MC.

## Appendix D

### Kolmogorov-Smirnov Test

The Kolmogorov-Smirnov (K-S) test [69] is a statistical test which checks the compatibility of the two unbinned 1-dimensional data samples. The advantage of the K-S test is that its result is not affected by the distribution function of the data, but the K-S test applies only to a continuous distribution.

When the two samples, A and B, have  $N_A$  and  $N_B$  elements, respectively, these elements should be in an ascending order before starting the K-S test. The  $N_A$  and  $N_B$  do not need to be the same for this test. These ascending ordered data sets can be plotted accumulatively as shown in Figure D.1. The plot shows the number of events normalized to the total number of events as a function of 1-dimensional variable (X). The test statistic in the K-S test is defined as the maximum vertical deviation (D) between the two cumulative data sets.

For the test in this thesis, the CERN routine, `TKOLMO(A,NA,B,NB,PROB)`, was used. The test result comes out as a probability. Obviously a result close to zero means little compatibility between the data samples. For two identical data sets, the test result should be equal to one.

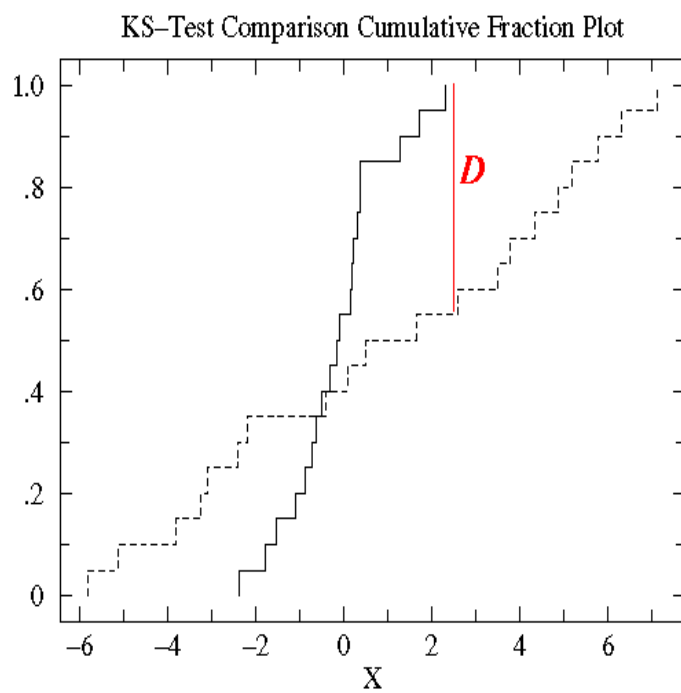


Figure D.1: The cumulative distributions of the two data sets being used for the K-S test. The  $D$  represents the maximum deviation of the two data sets.



# References

- [1] E. Tomasi-Gustafsson and M. P. Rekalo, nucl-th/001040 (2000).
- [2] S. D. Drell and F. Zachariasen, “Electromagnetic Structure of Nucleons”, Oxford Univ. Press (1961).
- [3] W. R. Frazer, “Elementary Particles”, Princeton Hall, INC. (1966).
- [4] M. Gourdin, Phys. Rep., **11C**, 30 (1974).
- [5] E. C. Titchmarsh, Theory of Functions, Oxford University Press, London, (1939).
- [6] M. N. Rosenbluth, Phys. Rev., **79**, 615 (1950).
- [7] R. Hofstadter and R. W. McAllister, Phys. Rev., **98**, 217 (1955).
- [8] A. Akhiezer and M. P. Rekalo, Dokl. Akad. Nauk USSR, **180**, 1081 (1968); Sov. J. Part. Nucl., **4**, 277 (1974).
- [9] R. Arnold *et al.*, Phys. Rev. C **23**, 363 (1981).
- [10] M. Rekalo and E. Tomasi-Gustafsson, nucl-th/0202025 (2002).
- [11] B. D. Milbrath *et al.*, Phys. Rev. Lett., **80**, 452 (1998); erratum, Phys. Rev. Lett., **82**, 2221 (1999).
- [12] M. K. Jones *et al.*, Phys. Rev. Lett., **84**, 1398 (2000).
- [13] O. Gayou *et al.*, Phys. Rev. Lett., **88**, 092301 (2002).
- [14] J. Arrington nucl-ex/0305009 (2003).
- [15] E. J. Brash *et al.*, Phys. Rev., **C 65**, 051001 (2002).
- [16] A. F. Sill *et al.*, Phys. Rev., **D 48**, 29 (1993).

- [17] J. Arrington, hep-ph/0209243 (2002), Invited talk at 7th Workshop on Electron Nucleus Scattering, Isola d'Elba, Italy, 24-28 Jun 2002.
- [18] J. Arrington, nucl-ex/0305009 (2003).
- [19] Proposal to PAC20, "Measurement of  $\frac{G_E}{G_M}$  to  $Q^2 = 9 \text{ GeV}^2$  via Recoil Polarization", C. F. Perdrisat, V. Punjabi, M. K. Jones, E. Brash *et al.*, Jefferson Lab Experiment E01-109 (2001).
- [20] A. Zichichi *et al.*, Nuovo Cimento **XXIV**, 170 (1962).
- [21] M. Jacob and G. C. Wick, Ann. Phys. (NY), **7**, 404 (1959).
- [22] M. G. Olsson and C. J. Suchyta III, Phys. Rev., D **34**, 2043 (1986).
- [23] T. A. Armstrong *et.al.*, Phys. Rev. Lett., **70**, 1212 (1993).
- [24] I. Peruzzi *et.al.*, Phys. Rev., **D 17**, 2901 (1978).
- [25] R. Brandelik *et.al.*, Z. Phys., **C 1**, 233 (1979).
- [26] M. W. Eaton *et.al.*, Phys. Rev., **D 29**, 804 (1984).
- [27] D. Pallin *et.al.*, Nucl. Phys., **B 292**, 653 (1987).
- [28] J. S. Brown, Ph.D. Thesis, Univ. of Washington UMI84-19117-mc (unpublished).
- [29] L. Kopke and N. Wermes, Phys. Rep., **174**, 67 (1989).
- [30] M. Claudson, S. Glashow, and M. Wise, Phys.Rev.,D **25**, 1345 (1982).
- [31] C. Carimalo, Int. J. Mod. Phys., **A 2**, 249 (1987).
- [32] R. G. Sachs, Proc. Int. Conf. on HEP at CERN, Geneva, 197 (1962).
- [33] V. A. Mateev et al., Lettere al Nuovo Cimento **7**, 719 (1973); S. J. Brodsky and G. R. Farrar, Phys. Rev. Lett., **31**, 1153 (1973).
- [34] S. J. Brodsky and G. R. Farrar, Phys. Rev. Lett., **43**, 545 (1979); Phys. Rev. **D 22**, 2157 (1980).
- [35] S. J. Brodsky and G. P. Lepage, Phys. Rev. Lett., **43**, 545 (1979); Phys. Rev., **D 22**, 2157 (1980).

- [36] S. M. Bilenky *et al.*, hep-ph/9304221 (1993).
- [37] R. G. Arnold *et al.*, Phys. Rev. Lett., **57**, 174 (1986); A. F. Sill *et al.*, SLAC-PUB-4395, (1992).
- [38] M. Andreotti *et al.*, Phys. Lett., **B559**, 20 (2003).
- [39] M. Ambrogiani *et al.*, Phys. Rev., **D60**, 032002, (1999).
- [40] S. van der Meer, Rev. Mod. Phys. **57**, 689 (1983).
- [41] J. Morgan, The Antiproton Source Rookie Book, V.1.1 (1999): [www-bdnew.fnal.gov/pbar/documents/PBAR\\_Rookie\\_Book.PDF](http://www-bdnew.fnal.gov/pbar/documents/PBAR_Rookie_Book.PDF).
- [42] M. Church, FERMILAB-Pub-97/049 (1997).
- [43] J. Marriner, FERMILAB-Conf-93/308 (1993).
- [44] F. Caspers, Workshop on “Beam Cooling and Related Topics”, 14-18 May 2001, Physikzentrum Bad Honnef, Germany; CERN/PS 2001-017 (RF) (2001).
- [45] S. Werkema, Fermilab Pbar Note **559** (1996): [http://www-bdnew.fnal.gov/pbar/documents/pbarnotes/pbar\\_notes\\_501-600.htm](http://www-bdnew.fnal.gov/pbar/documents/pbarnotes/pbar_notes_501-600.htm).
- [46] D. Allspach *et al.*, FERMILAB-Pub-97/274-E (1997).
- [47] S. Tokenheim *et al.*, Nucl. Inst. Meth. A **355**, 308 (1995).
- [48] S. Werkema, Fermilab Pbar Note **633** (2000): [http://www-bdnew.fnal.gov/pbar/documents/pbarnotes/pbar\\_notes\\_601-700.htm](http://www-bdnew.fnal.gov/pbar/documents/pbarnotes/pbar_notes_601-700.htm).
- [49] H. Schopper “Advances of Accelerator Physics and Technologies”, World Scientific (1993).
- [50] D. Boussard, “Schottky Noise and Beam Transfer Function Diagnostics” in “CERN Accelerator School Advanced Accelerator Physics”, The Queen’s College, Oxford, England, Sept. 1985, CERN Yellow Report 87-03 (1987), pp416-452.
- [51] G. Stancari, E835 memo **411** (2000).
- [52] S. Bagnasco *et al.*, “A Straw Chambers’ Tracker for the High Rate Experiment 835 at the Fermilab Accumulator”, Nucl. Inst. Meth. A **409**, 75 (1998).

- [53] D. Bettoni et al., “Experimental Study of a Cylindrical Scintillating Fiber Detector”, IEEE Trans. Nucl. Sci., **44**, 460 (1997).
- [54] W. Baldini et al., “The New Scintillating Fiber Detector of E835 at Fermilab”, Nucl. Inst. Meth. A **461**, 219 (2001).
- [55] S. Bagnasco et al., “The Threshold Gas Čerenkov Counter of Charmonium Experiment 835 at Fermilab”, Nucl. Inst. Meth. A **424**, 304 (1999).
- [56] G. Lasio and M. Stancari, “Calibration of the Central Calorimeter in E835” E835 internal memo (2000).
- [57] M. Graham, “The Two Photon Decay of the  $\chi_0$  State of Charmonium”, PhD Thesis, University of Minnesota, Minneapolis (2003).
- [58] G. Garzoglio et al., to be published in NIM (2003).
- [59] M. Graham et al., “FCAL 2000 Calibration”, E835 internal memo (2001).
- [60] W. Baldini et al., Nucl., Inst. and Meth. **A449**, 331 (2000).
- [61] <http://www.e835.to.infn.it/people/wander/E835/E835.html>.
- [62] G. Oleynik et al., IEEE Trans. Nucl. Sci. **41**, 45 (1994).
- [63] R. Ray et.al., Nucl. Inst. and Meth. **A307**, 254 (1991).
- [64] J. Kasper, “Search for two omega meson decays of charmonium resonances produced in proton-antiproton annihilation”, Northwestern University, PhD thesis (2002).
- [65] GEANT 3.21 “Detector Description and Simulation Tool”, <http://wwwinfo.cern.ch/asd/geant>.
- [66] G. Garzoglio et al., to be published in NIM (2003).
- [67] W. R. Leo, “Techniques for Nuclear and Particle Physics Experiments” second edition, Springer-Verlag (1994).
- [68] C. Patrignani, E835 internal memo # 395.
- [69] A. G. Frodesen, O. Skjeggstad and H. Tøfte, “Probability and Statistics in Particle Physics”, Universitetsforlaget, Bergen (1979).

- [70] PAW: Physics Analysis Workstation  
(<http://wwwasd.web.cern.ch/wwwasd/paw/>).
- [71] F. James, MINUIT: Function Minimization and Error Analysis Reference Manual, Version 94.1 (1998); CERN Program Library Long Writeup D506  
(<http://wwwasdoc.web.cern.ch/wwwasdoc/minuit/minmain.html>).
- [72] G. Garzoglio et al., to be published in NIM (2003).
- [73] K. Hagiwara et al., Phys. Rev., **D66** (2002).
- [74] L. Kopke and N. Wermes, Phys. Rep., **174**, 67 (1989).
- [75] M. Claudson, S. Glashow, and M. Wise, Phys. Rev., **D25**, 1345 (1982).
- [76] C. Carimalo, Int. J. Mod. Phys., **A2**, 249 (1987).